Lawrence Berkeley Laboratory

UNIVERSITY OF CALIFORNIA

Physics, Computer Science & Mathematics Division

CHARM PRODUCTION BY MUONS AND ITS ROLE IN
SCALE-NONINVARIANCE

G.D. Gollin, F.C. Shoemaker, P. Surko, A.R. Clark,
K.J. Johnson, L.T. Kerth, S.C. Loken,
T.W. Markiewicz, P.D. Meyers, W.H. Smith,
M. Strovink, W.A. Wenzel, R.P. Johnson, C. Moore,
M. Mugge, R.E. Shafer

March 1981

DISCLAIMER

Charm Production by Muons and Its Role

in Scale-Noninvariance*

G.D. Gollin[a], F.C. Shoemaker, and P. Surko[b]

Joseph Henry Laboratories, Princeton University,
Princeton, New Jersey 08544

and

A.R. Clark, K.J. Johnson, L.T. Kerth, S.C. Loken, T.W. Markiewicz,

P.D. Meyers, W.H. Smith, M. Strovink, and W.A. Wenzel

Physics Department and Lawrence Berkeley Laboratory,
University of California, Berkeley, California 94720

and

R.P. Johnson, C. Moore, M. Mugge, and R.E. Shafer

Fermi National Accelerator Laboratory,
Batavia, Illinois 60510

ABSTRACT

Interactions of 209 GeV muons in the Multimuon Spectrometer at Fermilab have yielded more than 8×10^4 events with two muons in the final state. After reconstruction and cuts, the data contain 20 072 events with $(81 \pm 10)\%$ attributed to the diffractive production of charmed states decaying to muons. The cross section for diffractive charm muoproduction is $6.9^{+1.9}_{-1.4}$ nb where the error includes systematic uncertainties. Extrapolated to $Q^2=0$ with $\sigma(Q^2)=\sigma(0)(1+Q^2/\Lambda^2)^{-2}$, the effective cross section for 178 (100) GeV photons is 750^{+180}_{-130} (560^{+200}_{-120}) nb and the parameter Λ is 3.3 ± 0.2 (2.9 ± 0.2) GeV/c. The ν dependence of the cross section is similar to that of the photon-gluon-fusion model. Okubo-Zweig-Iizuka selection rules and unitarity allow the muon data to set a 90% confidence lower limit on the ψN total cross section of 0.9 mb. A first determination of the structure function $F_2(c\bar{c})$ for diffractive charm production indicates that charm accounts for approximately 1/3 of the scale-noninvariance observed in inclusive muon-nucleon scattering at low Bjorken x.

I. INTRODUCTION

In 1964 Bjorken and Glashow proposed a constituent model for hadrons in which four fundamental "baryons" were linked by SU(4) symmetric forces.[1] Baryon number, electric charge, hypercharge, and a new quantum number, charm, were conserved quantities in their theory. They predicted that charmed mesons would have masses of approximately 760 MeV and noted that their model was "vulnerable to rapid destruction by the experimentalists."[1] Six years later, Glashow, Iliopoulos, and Maiani (GIM) proposed another SU(4) charm model, this time a four quark extension[2] of Gell-Mann's three quark theory.[3] The GIM model eliminated strangeness-changing neutral currents from the Weinberg-Salam model of weak interactions, which previously had predicted anomalously high rates for the decays $K_L \to \mu^+ \mu^-$ and $K^+ \to \pi^+ \nu \bar{\nu}$.

The ψ was discovered in proton-beryllium collisions and in electron-positron annihilation in 1974.[4] Its narrow width indicated that the ψ did not decay strongly and suggested that it was a bound state of a new quark and its antiquark, the charmed quark of the GIM model. The lightest charmed mesons, the $D^0(1863)$ and $D^+(1868)$ were observed at the Stanford electron-positron collider, SPEAR, in 1976.[5] The system recoiling against a D was found to be always at least as massive as the D, evidence for the associated production of the new mesons. Excited states of the ψ and heavier charmed particles such as the D^*, F, χ, and Λ_c have also been observed.[6,7]

A. Models for charm production by muons

In the simple quark model, nucleons are said to consist of three valence quarks and a surrounding veil of sea quarks and antiquarks. A beam particle can transfer energy and momentum to a virtual charmed quark (or antiquark), creating a charmed particle. Figure 1(a) illustrates this process for charm muoproduction.

Another approach is provided by the vector-meson dominance model (VMD), shown in Fig. 1(b). In VMD, charm production is a two step process. A virtual photon (γ_V) from the beam muon's electromagnetic field couples directly to a vector meson, the ψ, which then scatters off the target into a pair of charmed particles.[8] The model assumes that the γ_V-ψ coupling is nearly independent of Q^2 and that the ψ-N scattering is largely diffractive so that the charmed quarks in the exchanged ψ appear in the final state. VMD predicts the Q^2-dependence of the reaction $\gamma_V N \rightarrow c\bar{c}X$ to be $(1 + Q^2/m^2_\psi)^{-2}$, the propagator for the virtual ψ in the Feynman diagram of Fig. 1(b). Here, c is a charmed quark and $\bar{c}$ is its antiquark. The model does not predict the ν dependence of charm muoproduction. Unlike the simple quark model, VMD predicts a strong correlation between the momenta of the daughter particles. VMD describes well the production of the light particles ρ, ω, and ϕ. The larger extrapolation from $Q^2 = 0$ to $Q^2 = m^2_\psi$ required for charm production however is unsettling.[8]

A recent model for heavy-quark muoproduction is the virtual photon-gluon-fusion (γGF) model.[9] Figure 1(c) shows the Feynman diagram for γGF charm production. A virtual photon from the beam muon fuses
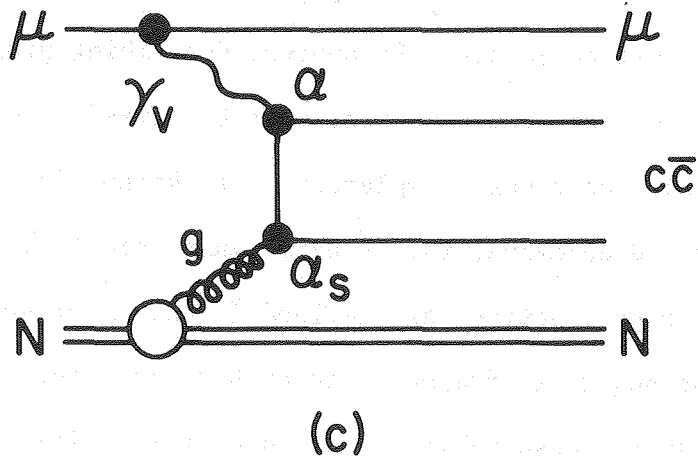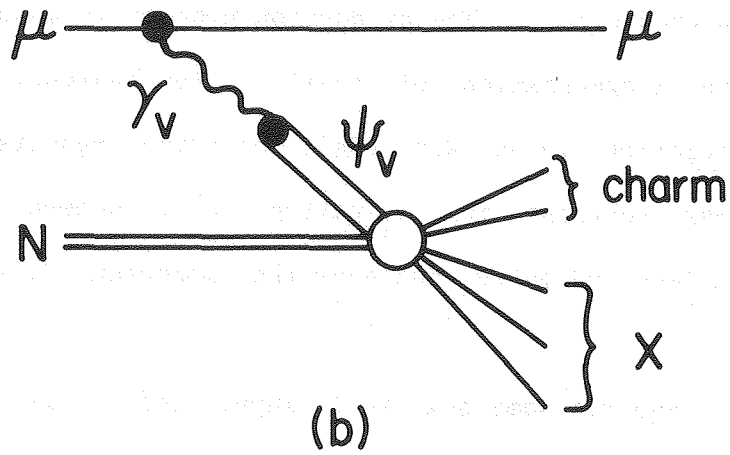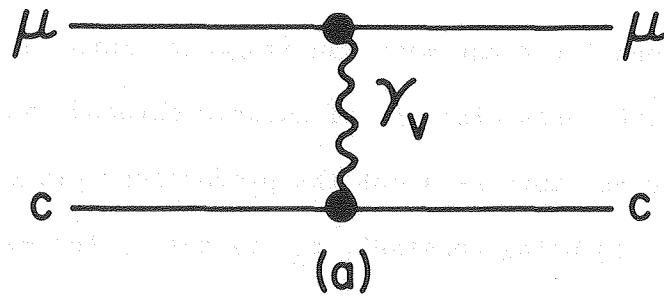
XBL 8011-7423

FIG. 1

with a gluon from the target, producing a charmed quark and antiquark. A $c\bar{c}$ pair with sufficient invariant mass can fragment into a pair of charmed particles. γGF uses elements of quantum chromodynamics (QCD) and makes the following assumptions about the production process. The scale of the strong coupling constant, α_s, is set by the mass of the charm system. The exchange of gluons between the $c\bar{c}$ pair and the target to ensure color conservation is assumed to be a soft process which does not change the γGF predictions. The production process is assumed to be unaffected by the fragmentation of quarks into hadrons. Ordinary parton-model calculation rules are used, allowing results to be expressed as cross sections for γ_V-parton $\rightarrow c\bar{c}X$, summed over the contents of the nucleon and integrated over the momentum distributions of the partons.[9]

The γGF model requires some numerical input before it can make predictions. The mass of the charmed quark must be specified. The distribution of momentum fraction x_g for gluons must be defined. The mass scale of α_s must be chosen. Parameters describing properties of the nucleon target, such as -t dependence, must be fixed. Once these are set, the model describes completely the kinematics of charm production. Q^2 and ν dependence, the $c\bar{c}$ pair mass spectrum, and the total production cross section are defined.[9] When a prescription is adopted to allow the quarks to fragment into hadrons, the γGF model describes charmed states observable in the laboratory. The predictions of γGF will be discussed in detail later.

B. The muon experiment

This paper describes interactions of the form $\mu N \rightarrow \mu \mu X$ observed in the Multimuon Spectrometer (MMS) at Fermilab. Brief descriptions of the results obtained from these observations have appeared in Refs. 10 and 11. Data from $\sim 4 \times 10^{11}$ 215 GeV beam muons were collected during the first half of 1978. Results from 1.388×10^{11} positive and 2.892×10^{10} negative beam muons are presented, covering the range $0 \ (GeV/c)^2 \leq Q^2 \leq 50 \ (GeV/c)^2$ and $50 \ GeV \leq \nu \leq 200 \ GeV$. After reconstruction and cuts, the data contain 20 072 events with two muons in the final state, most from the production and decay of charmed particles. The statistical power of such a large sample allows a measurement of differential spectra for charm muoproduction.

Section II describes the beam system and muon spectrometer. Section III describes event reconstruction, acceptance modeling, and background modeling. Extraction of the charm signal, general features of the data, and estimation of systematic errors are also discussed. Section IV presents results of measurements of the diffractive charm muoproduction total cross section, the Q^2 and ν dependence of charm virtual photoproduction, and the role of charm in the rise with energy of the photon-nucleon total cross section. A lower limit on the ψN total cross section is presented. The contribution of charm production to the scale non-invariance observed in muon-nucleon scattering at low Bjorken x is discussed.

II. THE BEAM AND THE MULTIMUON SPECTROMETER

Muons from the N1 beam line at Fermilab arrived at the south end of the muon laboratory, passed through the air gap of the Chicago Cyclotron Magnet (CCM), and entered the Multimuon Spectrometer (MMS). The trajectories of beam muons and any scattered or produced muons were registered by wire chambers placed periodically in the MMS. Data from events satisfying any of four sets of trigger requirements were recorded on magnetic tape for subsequent analysis.

The muon spectrometer was conceived as a detector for a high-luminosity muon scattering experiment studying rare processes with one or more muons in the final state. Good acceptance for both high-Q^2 scattering events and low-Q^2 multimuon events was desired. An intense muon beam incident on a long target could provide the desired luminosity while a spectrometer sensitive to muons produced at large and small angles to the beam could meet the acceptance requirements.

The detector was built in 1977 as a distributed target dipole spectrometer. Magnetized iron plates were grouped into eighteen closely spaced modules. Each module was instrumented with wire chambers and hadron calorimetry. The spectrometer was active over its entire fiducial area, including the region traversed by the beam, allowing reconstruction of low-Q^2 multimuon events.

The beam system and individual elements of the Multimuon Spectrometer will be described below.

A. The muon beam

A schematic diagram of the N1 beam line is shown in Fig. 2. A primary beam of 400 GeV protons from the main ring was focused onto a 30 cm aluminum target. A series of quadrupole magnets, the quadrupole triplet train, focused the produced particles into a 400 m long decay pipe. A west bend at enclosure 100 momentum selected particles of one sign. An east bend at enclosure 101 acted as a momentum slit and bent the beam away from its lower-energy halo. Polyethylene absorber inside the west-bending dipoles of enclosure 102 stopped hadrons in the beam. Quadrupoles in enclosure 103 refocused the beam and an east bend at enclosure 104 made the final momentum selection. The Chicago Cyclotron Magnet bent the beam east into the MMS. [12]

Figure 3 shows the locations of multi-wire proportional chambers (MWPC's) and plastic scintillation detectors used to measure the beam and reject halo muons. MWPC's and scintillator hodoscopes after the quadrupoles in enclosure 103 and at the entrance to enclosure 104 measured the horizontal positions of muons. MWPC's and scintillator hodoscopes measured horizontal and vertical coordinates at the downstream end of enclosure 104, at the entrance to the muon lab, immediately downstream of the CCM, and immediately upstream of the MMS. Halo muons were detected at three points upstream of the spectrometer. A "jaw" scintillation counter in enclosure 104 registered muons which passed through the iron of the enclosure's dipoles. Scintillation counters in a ∿10m wide by ∿5m high wall downstream of the CCM also detected halo muons. A scintillator hodoscope with a hole for the beam

FIG. 2

XBL 8010-2137

Dipole magnets

Muon Laboratory

CCM

MMS

BH(x)

IO4

BH(x,y)
MWPC

BH(x,y)
MWPC

V$_j$

V$_w$
BH
MWPC

V$_b$

V$_h$

BH(x,y)

MWPC

IO3

BH(x)

MWPC

Quadrupole magnet

BH   Beam scintillator hodoscope
V$_j$ "Jaw" veto counter
V$_w$ Large veto wall
V$_h$ Halo veto hodoscope
V$_b$ Bucket occupancy veto counter
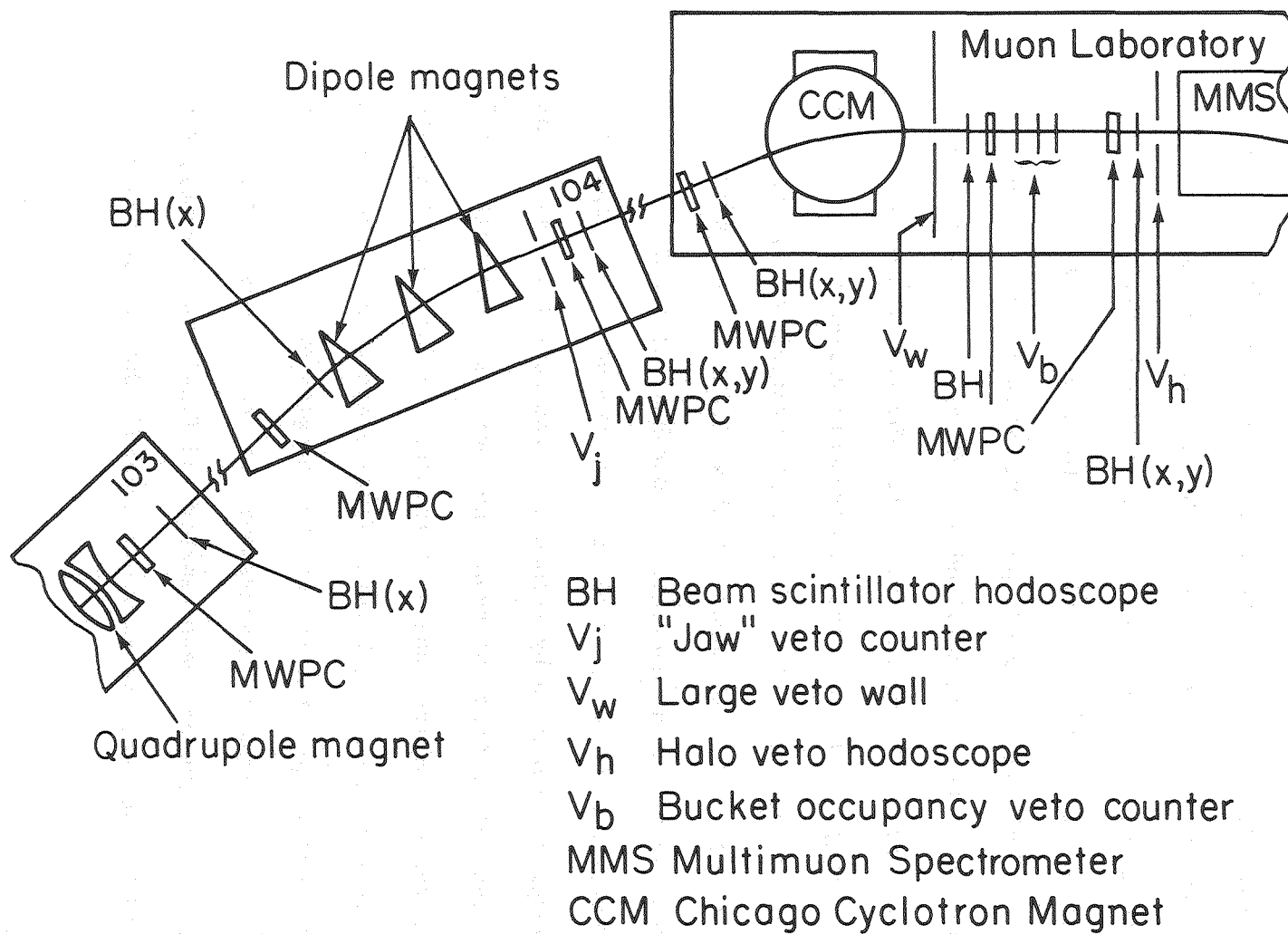MMS Multimuon Spectrometer
CCM Chicago Cyclotron Magnet
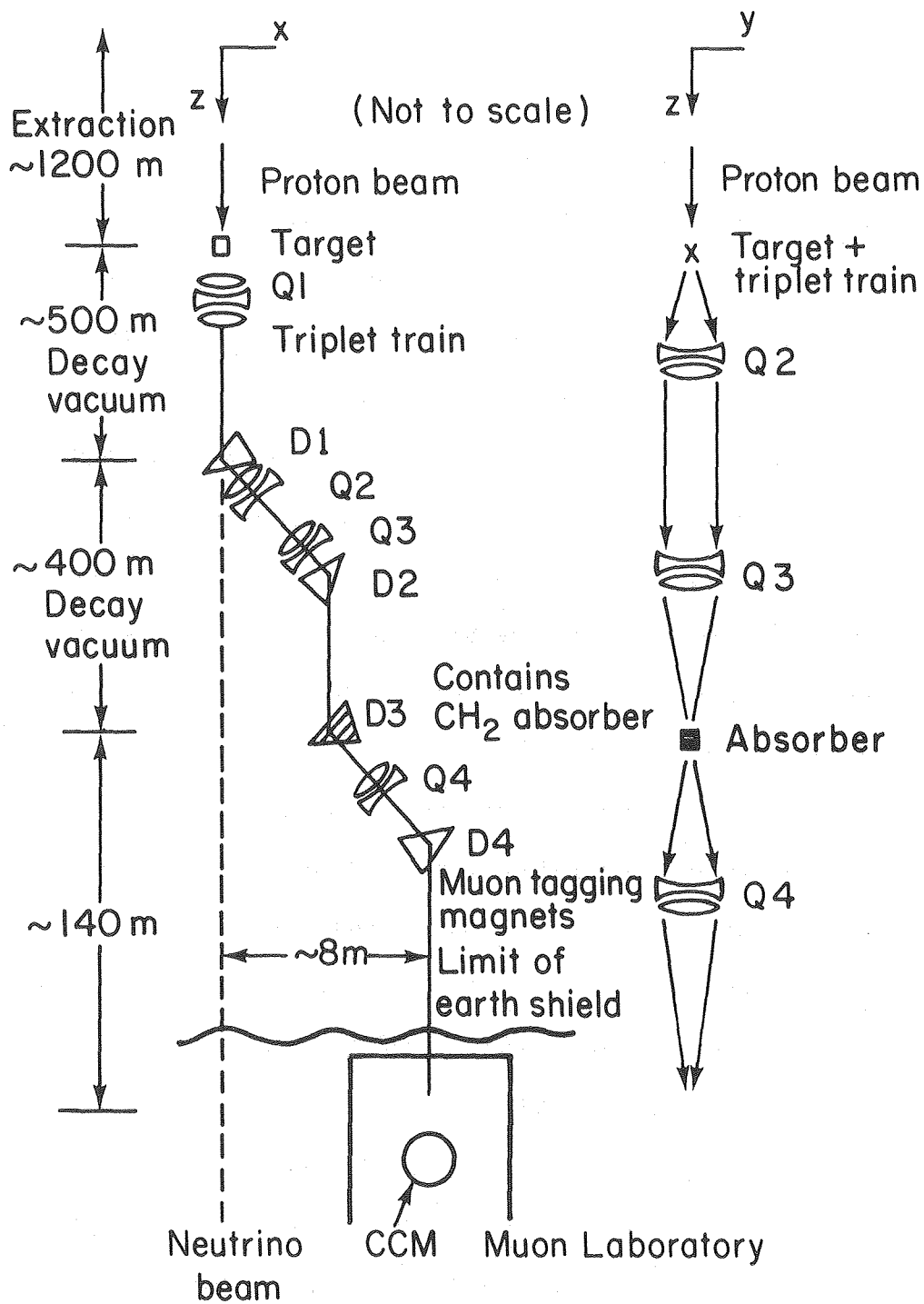
XBL 8010-2139

FIG. 3

covered the front of the muon spectrometer and counted halo particles entering the detector. A signal from any of the halo counters along the beam disabled the MMS triggers. Scintillation detectors in the beam counted incident muons and vetoed events with more than one muon in an rf bucket or with muons in the preceding or following buckets.

Data were taken with 10^{13} to 1.7×10^{13} protons/spill incident on the primary target. Typically 1.9×10^6 positive muons/spill in a beam 8 inches high and 13.5 inches wide survived all vetoes. An equal number were present in the halo outside the beam. The fraction of positive muon flux which satisfied all the veto requirements varied from 1/2 with 10^{13} protons on target to 3/8 with 1.7×10^{13} protons on target. The effective yield of positive beam muons was about 1.4×10^{-7} muons/proton. The yield of negative muons was one-third to one-half as great.

The beam energy was 215 GeV with a $\pm 2\%$ spread. A comparison between beam energies determined by elements in the beam line and by the MMS showed that the values from the beam line were systematically 1.5 GeV greater than those from the muon spectrometer. A further check came from elastic ψ production data with three final-state muons. Requiring that the beam energy equal the sum of the energies of the final-state muons showed the beam system's measurement to be 2 GeV high. To maintain consistency between beam energy and final state energy, the momentum measured by the beam system was decreased during analysis by about 1.5 GeV/c.

B. The Multimuon Spectrometer

The muon spectrometer consisted of four major systems. Steel slabs served as an analyzing magnet and rectangular scintillation counters measured hadronic shower energies. Trigger hodoscopes determined event topologies and wire chambers sampled muon trajectories. The detector is shown in Fig. 4; each of its four systems will be described below.

1. The magnet

The most massive component of the detector was the 475 ton steel target and momentum - analyzing magnet. The steel was rolled and flame cut into ninety-one plates, each 4 inches thick and 8 feet square. They were grouped into eighteen modules, with five slabs per module. An additional slab was placed upstream of the first detector module. The fiducial area was magnetized vertically to 19.7 kG by two coils running the length of the spectrometer through slots in the steel. The magnetic field was uniform to 3% over the central 1.4x1 m area of the slabs. It was mapped with 0.2% accuracy using flux loops. The location of the peak in the $\mu^+\mu^-$ pair mass spectrum at 3.1 GeV/c^2 from events

$$\mu N \rightarrow \mu \psi X, \ \psi \rightarrow \mu^+ \mu^- \tag{1}$$

provided confirmation that the field measurements were correct. The

MULTI-MUON SPECTROMETER
BERKELEY-FERMILAB-PRINCETON

FIG. 4

XBL 795-9605

MODULES 1 2 3 4 5 6 7 8 9 10 11 12 13 14 15 16 17 18

$\vec{B}$

$\mu^{\pm}$

S_{3-10}

S_1 S_2

S_{11} S_{12}

PC (X+Y+U)

DC (X)

5C

Y

X

U

S_{1-12} in modules 4,6,8,10,12,14,16,18
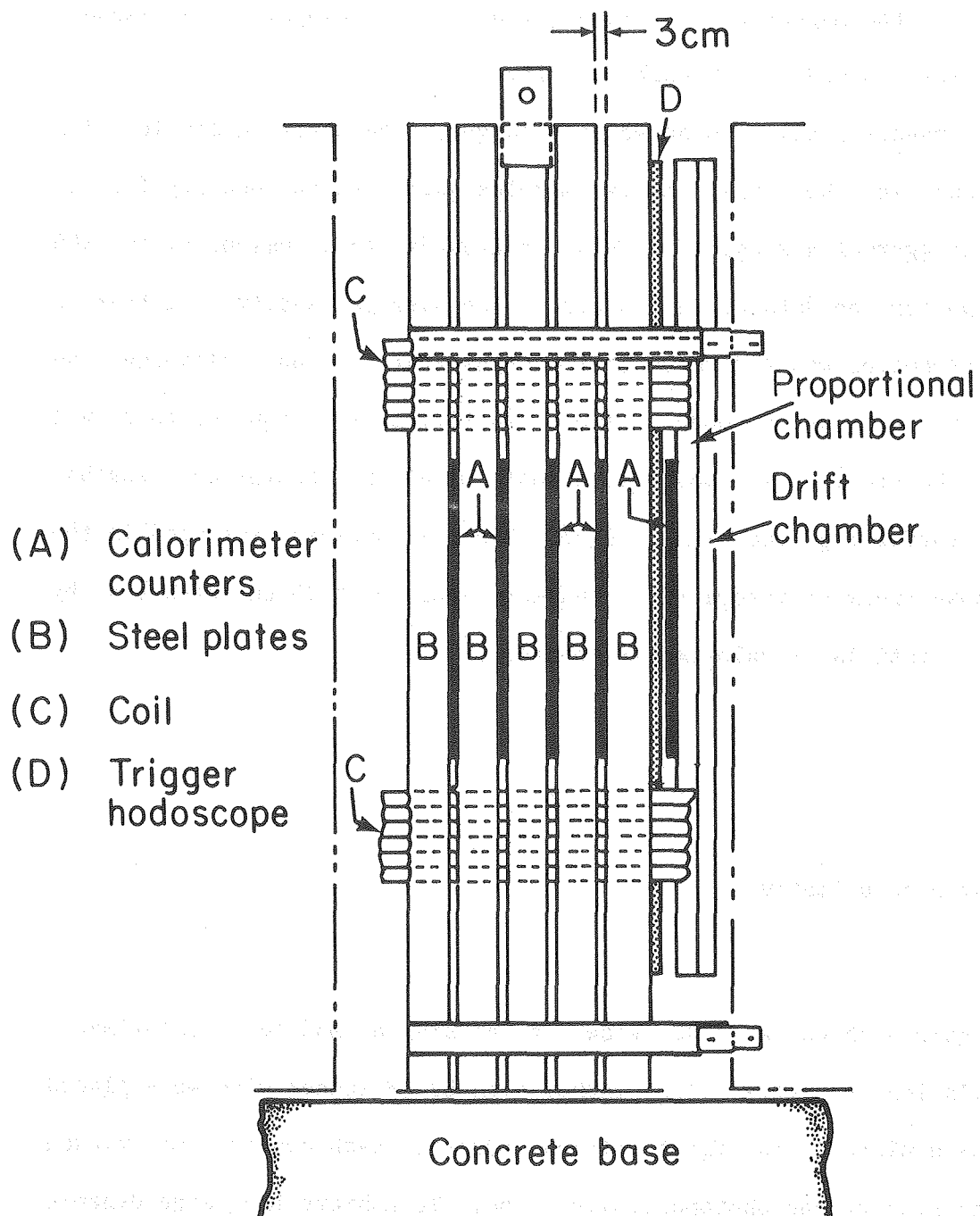
PC + DC in 1-18   5C in 1-15
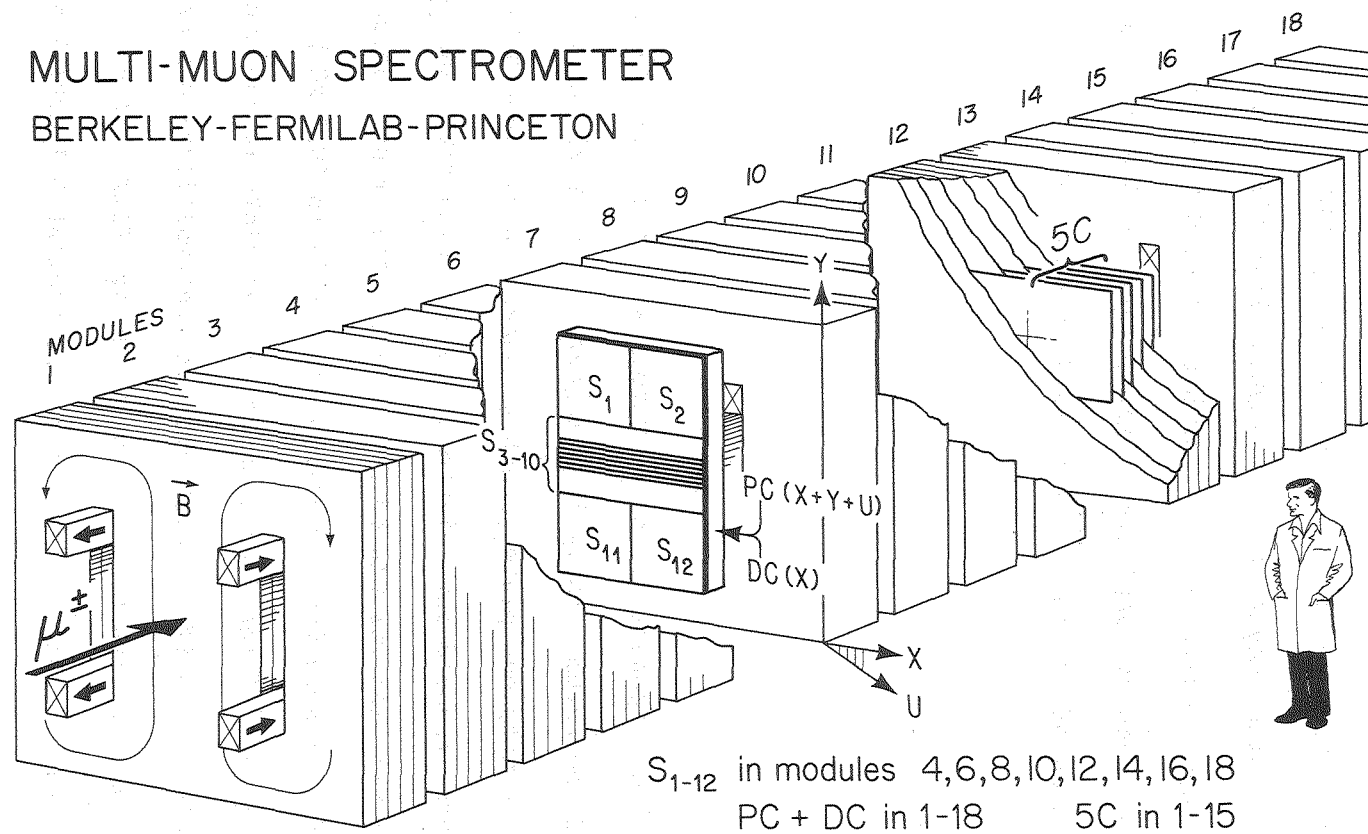
polarity of the magnet was reversed periodically. Roughly equal amounts of data were recorded with each polarity.

The magnet steel also acted as a target. The upstream single slab and slabs in the first twelve modules gave a target density for the dimuon trigger of 4.9 kg/cm^2. This corresponded to a luminosity of 500 events/pb for the data presented here. The average density of matter in the spectrometer was 4.7 gm/cm^3, six-tenths that of iron, allowing the magnet to act as a muon filter. Particles were required to travel through the steel of six modules, almost eighteen absorption lengths, before satisfying the $\mu\mu$ trigger. Hadronic showers developed in the steel downstream of interactions and were sampled at 10 cm intervals by plastic-scintillator calorimeter counters.

2. Hadron calorimetry

Figure 5 shows a side view of a single module. Calorimeter scintillation counters 31.5 inches high by 48 inches wide were placed after each plate in the first fifteen modules. Each counter was viewed from the side by one photomultiplier tube. To achieve the large dynamic range required, signals from the tubes were amplified in two stages and the output from each stage was recorded by an analogue - to - digital converter.

Deep inelastic scattering data and ψ production data provided calorimeter calibration information. Magnetic measurements of energy

3cm

D

C

Proportional chamber

Drift chamber

A   A   A

(A) Calorimeter counters

(B) Steel plates

(C) Coil

(D) Trigger hodoscope

B B B B B

C

Concrete base

XBL 8010-2254

FIG. 5

lost by muons in inelastic scattering events related calorimeter pulse heights to hadronic shower sizes. The calorimeter's zero level was set with the help of ψ events which had less than 36 GeV of shower signal. By requiring agreement between the average beam energy and the average visible energy in the final state (the sum of the three muons' energies and the calorimeter signal), a zero-shower-energy pulse height was determined. The rms accuracy of the hadron calorimetry was $\Delta E=1.5E^{\frac{1}{2}}$ for ΔE and E in GeV, with a minimum uncertainty of 2.5 GeV.
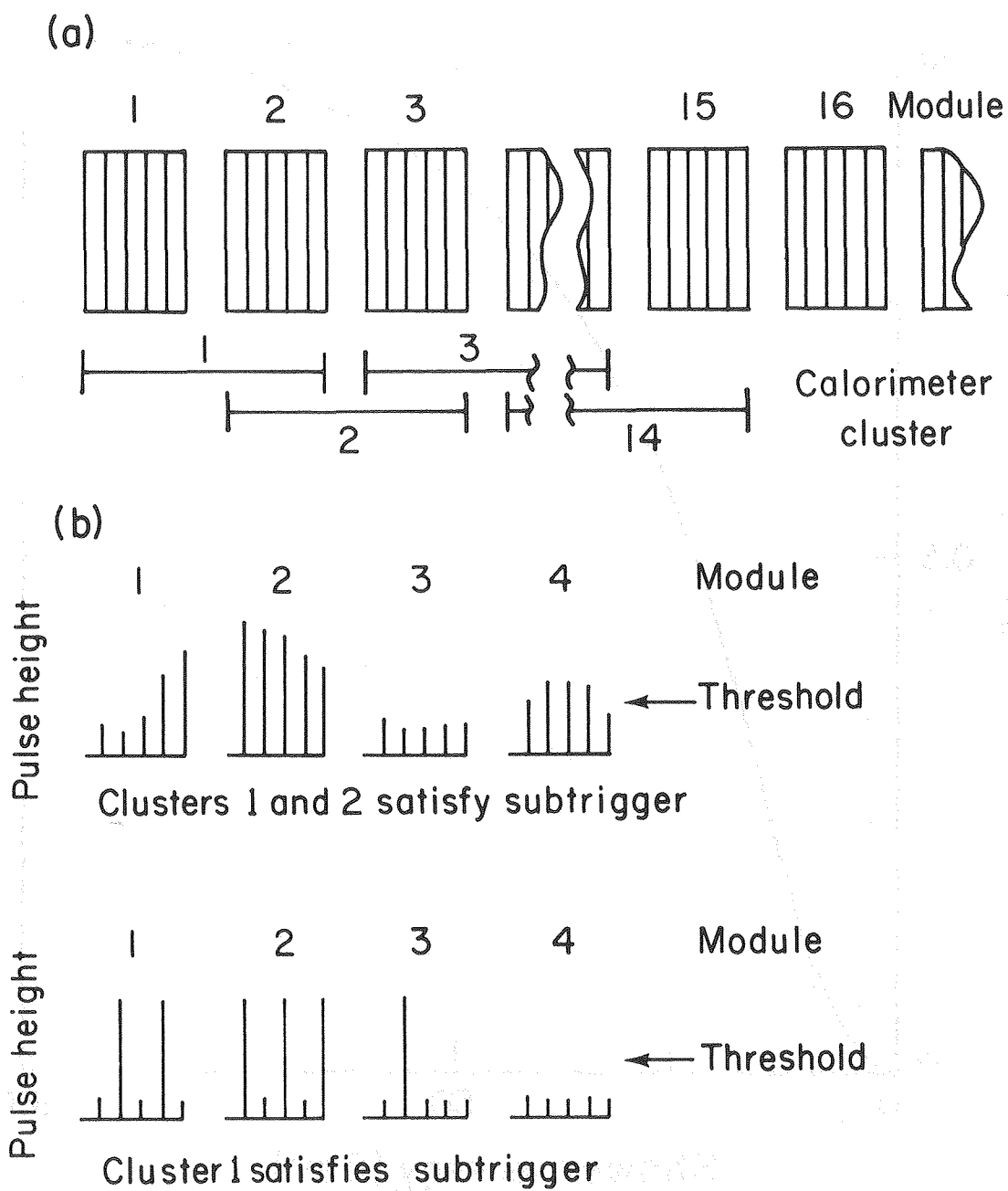
3. Trigger hodoscopes and the dimuon trigger

Each of the spectrometer's eight trigger hodoscopes was composed of four large "paddle" counters and eight narrow "stave" counters. The arrangement of scintillator elements in a trigger bank is shown in Fig. 4. Hodoscopes were placed in the gaps following every other module, starting with the fourth. The muon experiment took data using four different triggers, run in parallel. The high-Q^2 single-muon trigger required each of three consecutive trigger banks to have no hits in any stave counter and to have a hit in a paddle counter. The three-muon trigger required each of three consecutive banks to have hits corresponding to three particles with some vertical opening, perpendicular to the bend plane. The "straight-through" trigger required a beam muon to enter the spectrometer without passing through any of the upstream halo counters and was prescaled by typically 3×10^5.
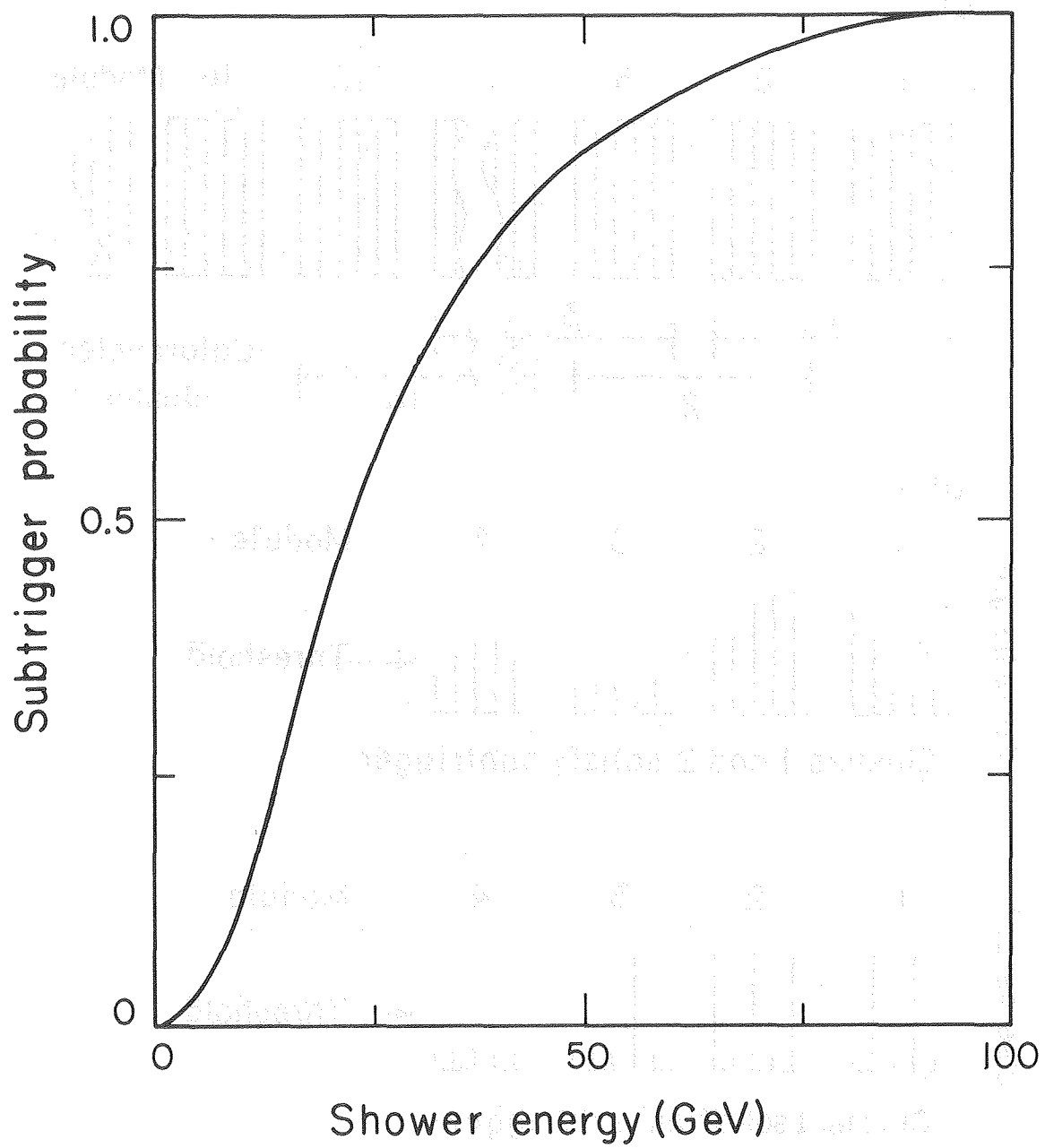
The two-muon trigger required both a shower signal from the calorimetry and a pattern of hits in three consecutive trigger hodoscopes downstream.

The dimuon calorimeter subtriggers are illustrated in Fig. 6. Calorimeter counters were ganged in half-overlapping clusters of ten. The first cluster included scintillators in modules one and two, the second in modules two and three, etc. giving a total of fourteen clusters. When signals from at least half the counters in a cluster exceeded a threshold level, that cluster's subtrigger was enabled. The greater range in steel of hadronic showers allowed the calorimetry to discriminate against electromagnetic cascades. The probability to satisfy the calorimeter subtrigger vs. shower energy is shown in Fig. 7. The subtrigger probability was measured when the calorimeter was calibrated. It was found by determining the fraction of deep inelastic showers of given energy which set calorimeter subtrigger bits. The hodoscope subtriggers required two or more counters to fire in each of the upstream pair of a group of three consecutive banks comprising the trigger. The downstream bank needed signals in two staves with at least one empty stave between them, or hits in one paddle and any other counter, or hits in any three counters to complete the subtrigger. There were six different hodoscope subtriggers, corresponding to each combination of three successive trigger banks. Possible hit patterns satisfying a hodoscope subtrigger are shown in Fig. 8. The dimuon full trigger required both a calorimeter and a hodoscope subtrigger, with a separation along the beam direction between them. The upstream end of the earliest calorimeter cluster participating in the trigger was required to be at least seven modules from the furthest downstream

(a)

1   2   3   15   16   Module

1
3
2
14

Calorimeter cluster

(b)

Pulse height

1   2   3   4   Module

← Threshold

Clusters 1 and 2 satisfy subtrigger

Pulse height

1   2   3   4   Module

← Threshold

Cluster 1 satisfies subtrigger

XBL 8010-2136

FIG. 6

XBL 8010-2141

FIG. 7

(a)

3 Two non-
adjacent staves

2 Two staves

1 Two staves

(b)

Three counters
struck

Two counters struck,
including one paddle
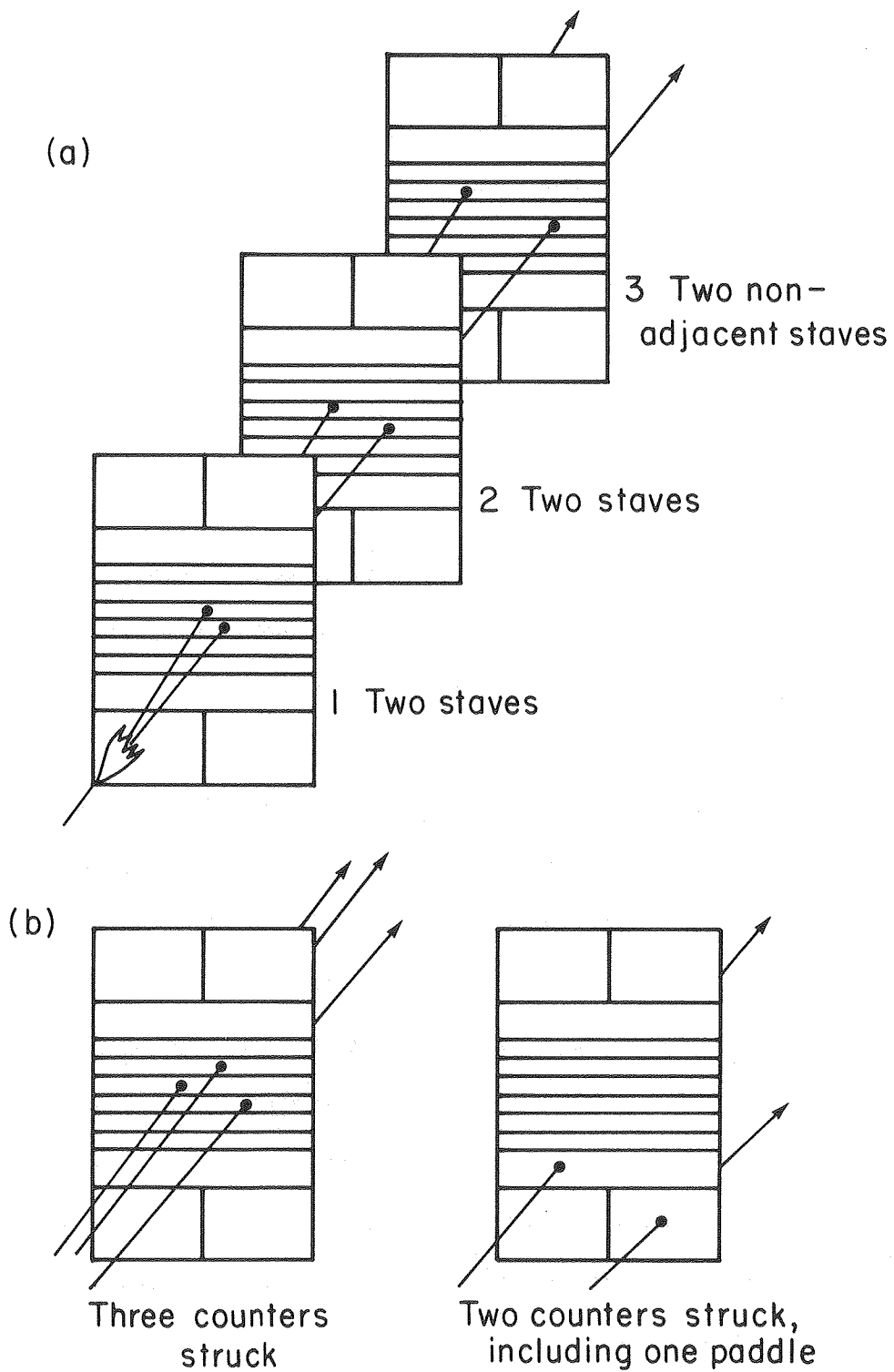
XBL 8010-2138

FIG. 8

trigger bank in the trigger. Table 1 lists possible calorimeter-hodoscope subtrigger combinations. The hodoscope subtrigger rate was typically 1.3×10^{-3} per beam muon while the full dimuon trigger rate was about 8×10^{-6} per beam muon.

4. Wire chambers

A system of nineteen multiwire proportional chambers (MWPC's) and nineteen drift chambers (DC's) measured horizontal and vertical positions of muons in the spectrometer. An MWPC and a DC were placed upstream of the first module and in the gap following each of the eighteen detector modules. The spatial resolution of the chamber system was sufficient to allow multiple Coulomb scattering of muons in the steel magnet to limit the spectrometer's momentum resolution. The chambers were active in the beam region, greatly reducing the sensitivity of the dimuon detection efficiency to Q^2 and p_T. The wire chambers were built on aluminum jig plate, permitting them to be thin but rigid. This minimized the required widths of the inter-module gaps and maximized the average spectrometer density. Jig plate covered the upstream sides of the chambers and served to stop soft electron δ-rays traveling with beam muons.

The multiwire chambers had a single plane of sense wires, measuring coordinates in the horizontal (bend) plane. Signals induced on two high-voltage planes were read by center-finding circuitry shown in Fig.

9, yielding vertical and diagonal coordinates. There were 336 sense wires spaced 1/8 inch apart in each MWPC. High-voltage wires spaced 1/20 inch apart were ganged in groups of four, giving 196 diagonal channels and 178 vertical channels of information with an effective channel spacing of 1/5 inch. The proportional chambers were built on 1/2 inch jig plate and were active over an area 41.5 inches wide by 71.2 inches high. The separation between sense and high-voltage planes was 0.4 inches. The MWPC readout electronics were gated on for 70 nsec.

The chamber resolution was approximately equal to the wire spacing divided by $12^{\frac{1}{2}}$. The efficiencies of the multiwire chambers varied with position across the faces of the chambers and with chamber location along the spectrometer. Chambers near the front of the MMS had sense and induced plane efficiencies in the beam of 83% and 59% respectively while MWPC's towards the rear had sense and induced plane efficiencies in the beam of 88% and 76% respectively. Away from the beam, all proportional chambers had sense and induced plane efficiencies of 95% and 94% respectively.

The drift chambers were built with a single sense plane of fifty-six wires measuring coordinates in the bend plane. Track finding with proportional chamber information resolved the left-right ambiguity present in single plane DC's. The drift cells were 3/4 inch wide with field shaping provided by high-voltage planes spaced 1/8 inch from the sense plane. The separation between high-voltage wires was 1/12 inch.

Figure 10 illustrates the drift cell geometry and indicates the voltages applied to the field-shaping wires. The DC's were active over a 42 inch wide by 72.5 inch high area and were built on 5/8 inch aluminum jig plate.

MWPC Cathode amplifiers

Induced
charge

1/4MCI0115P

zero

to
disc.

Output
voltage
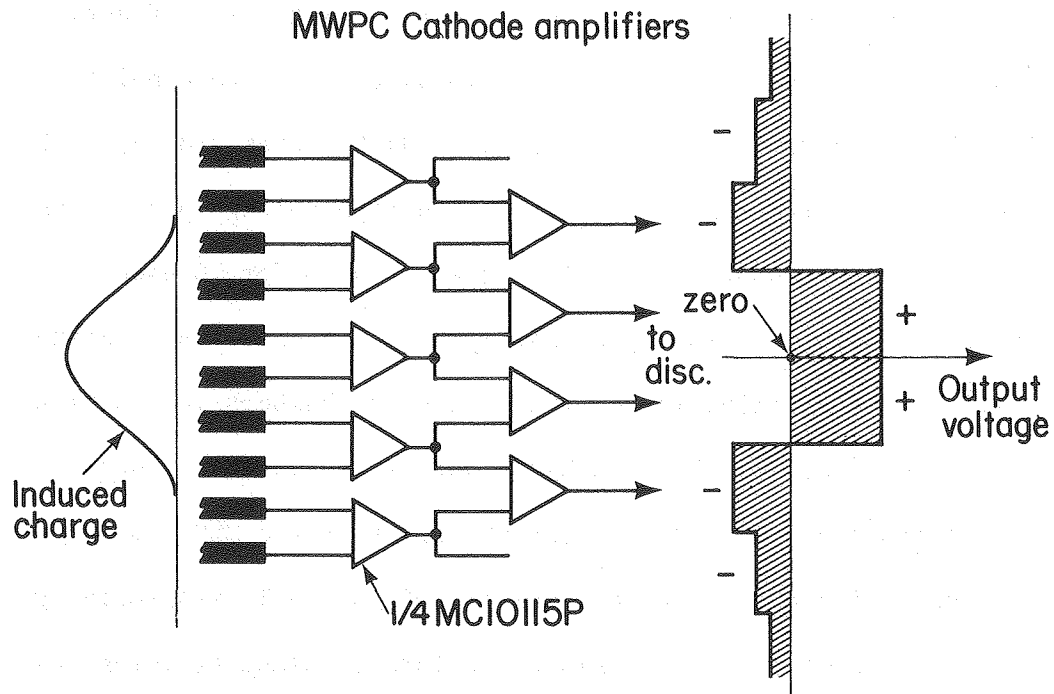
XBL 795-1599

FIG. 9
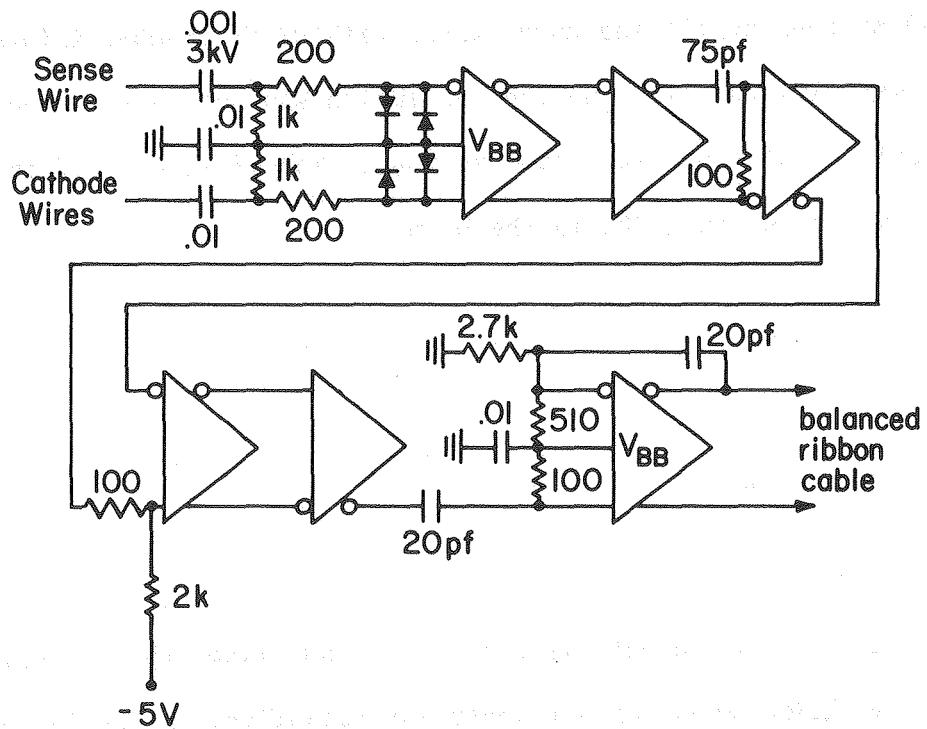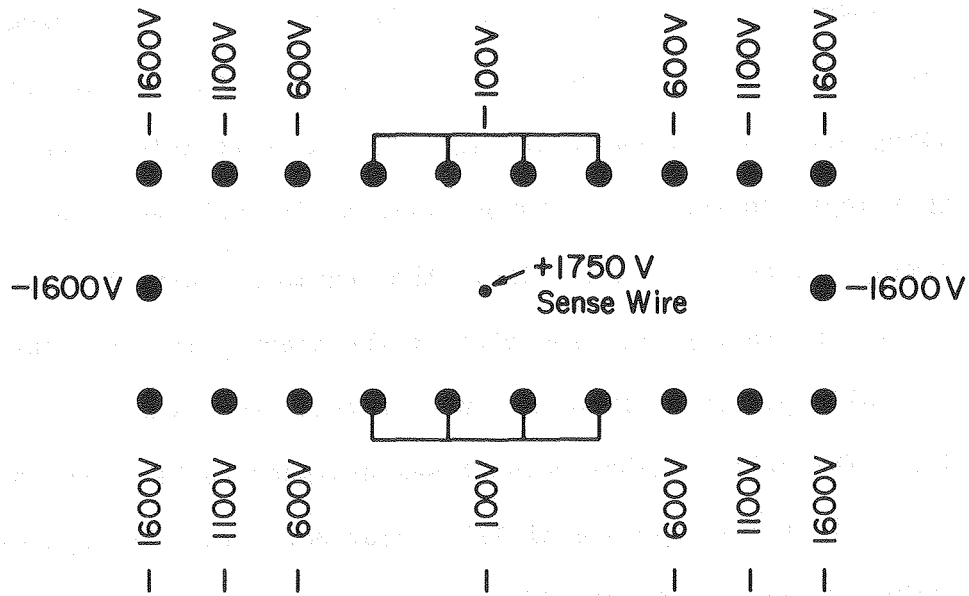
XBL 8011-7422

FIG. 10

The chamber preamplifiers read differential signals from the transmission lines formed by sense wires and the eight closest field-shaping wires as indicated in Fig. 10. A start pulse sent from the trigger logic to the drift chamber time digitizing system enabled a 120 MHz timing clock. Signals from the chambers arriving at the digitizer within thirty-one time bins of the start pulse were latched, though most valid pulses arrived in an interval approximately twenty bins wide. The drift chamber readout was designed to latch up to four hits per channel with an average of 1/2 scaler per wire. The system has been described in detail in Ref. 13.

The resolution of the drift chambers was determined to be better than 250 microns by fitting muon tracks with drift chamber information. An experimental lower limit on the resolution was not determined. The theoretical resolution was 150 microns. The efficiency of the drift chambers was better than 98% in the beam.

5. Data acquisition

Data from the different systems were read from the experimental hardware by CAMAC whenever a trigger was satisfied. A PDP-15 received the CAMAC information and stored it on magnetic tape. On-line displays, updated after each accelerator spill, permitted constant monitoring of the performance of the detector while the experiment was running. There were typically fifty triggers per spill; the maximum number that could

be processed was about twice that. The data transfer rate of the CAMAC system and the data handling speed of the computer set the limit on event rate.   Apparatus deadtime was typically less than 15%.

III. RECONSTRUCTION AND ANALYSIS

The muon experiment recorded more than 10^7 triggers on 1064 reels of computer tape. A track-finding program analyzed raw data, constructing muon trajectories from the wire chamber information. Taking into account multiple Coulomb scattering and energy loss, a track-fitting program momentum-fit all tracks that were found. A Monte Carlo program modeled the muon spectrometer, generating simulated raw data which were analyzed like real data. Different physics generators permitted the Monte Carlo to describe the detector's acceptance for both charm production and background processes.

This section discusses event reconstruction and data analysis. The first part describes the track-finding and momentum-fitting algorithms. The second describes acceptance modeling and the third describes background simulation. The fourth discusses methods used to isolate the charm signal from the backgrounds and the fifth presents general features of the reconstructed data and Monte Carlo simulations. The sixth details methods used to estimate systematic errors.

A. Reconstruction

The track-fitting and -finding programs analyze events of all four trigger topologies. The algorithms' reconstruction of dimuon triggers will be described below.

1. Track finding

Raw data from an event are unpacked and translated by the track finder into wire chamber hits, calorimeter scintillator pulse heights, and latch information. A filter routine inspects patterns of hits in the trigger hodoscopes. The filter requires the hodoscope information to be consistent with all tracks intersecting at a common vertex. About 22% of the triggers, some caused by δ-rays and by stray muons entering the top or bottom of the detector, are discarded.

Proportional chamber "blobs" are constructed of contiguous wire hits in each plane of the MWPC's. Since the deadtime of a drift chamber preamplifier corresponds typically to a drift distance of 2.5 mm, drift chamber "blobs" are constructed of all hits whose drift distances are within 2.5 mm of the drift distance of another hit on the same wire. MWPC hits in the planes measuring horizontal (x), vertical (y), and diagonal (u) coordinates are grouped into "triplets" or "matches" when any part of a u-plane blob is within 0.75 cm of the location expected from the pairing of a particular x blob and y blob. A blob may participate in at most three triplets; the matches are ordered by the difference between predicted and found u positions. Both triplets and blobs which are not part of a triplet are available to the routines which search for tracks.

Calorimetric information gives an estimate of the vertex position along z, the beam direction. The vertex algorithm finds the maximum calorimeter counter pulse height, A. For each slab in the detector it calculates a quantity N, where N is the difference between the number of

counters with pulse height less than 0.08A and the number of counters with pulse height greater than 0.08A, for all counters upstream of that slab. The middle of the slab with the largest value of N is chosen as the vertex z position. If several slabs share the largest value of N, the center of the slab closest to the front of the detector is chosen.

The track finder uses data from the wire chambers in the beam system to project a muon track into the detector. With information from the MWPC between the first plate and the first module, an incident position and angle for the beam muon are determined. The trial trajectory is then extended downstream using a fit which is linear in y and includes energy loss and bending due to the magnetic field in x. Chamber resolution and multiple scattering determine the size of a search window at each MWPC. The triplet inside the search window which is closest to the predicted location is placed on the track. If no triplets are found, unmatched blobs are used. The track finder recalculates the muon's trajectory with the new hits and projects downstream one module. The process is continued past the vertex found by the calorimeter algorithm. After filling in the entire beam track with proportional chamber information, the program adds drift chamber blobs to the muon's path. The two closest blobs in each drift chamber are assigned to the track in one pass, with no refitting after the addition of each DC's data.

The track finder next searches for muon trajectories downstream of the vertex. It begins at the back of the spectrometer and works upstream, constructing a trial track with hits from at least four MWPC's. When a track is found, drift chamber information is added simultaneously along the entire trajectory. MWPC triplets used in the

track are removed from the list of available matches. The program then begins the process again with the proportional chamber information still available.

To project a track forward from the back of the MMS, the track finder requires three triplets or two triplets and unmatched x and y hits in a third MWPC. The starting triplets may be separated by up to three proportional chambers, but there can be no more than one empty MWPC between any two chambers in the initial segment of three MWPC's. Chambers used on a track must have twelve blobs or less in the x plane. Within resolution and multiple scattering limits, the y coordinates must lie on a straight line. The curvature of the starting segment must correspond to a momentum greater than 15 GeV/c -2σ where σ is the error of the calculated momentum.

Three-chamber track segments are extended upstream past the vertex one module at a time. A multiple Coulomb scattering and resolution window is opened at each chamber and a triplet or unmatched blobs are placed on the track. The program refits the track with the new information, including energy loss and bending in the magnetic field, and continues upstream. When a track is complete, the two best drift chamber blobs in each DC are simultaneously assigned to the track and all used triplets are removed from the table of available matches.

The track-hunting process continues until all possible starting segments have been investigated. Tracks are required to contain (x,y) points from at least four proportional chambers with at least two of the points from MWPC triplets. Tracks are also required to have a fit momentum of less than 325 GeV/c. The χ^2 per degree of freedom for tracks fit only with proportional chamber information must be less than

4 or 5 for x or y views respectively. Dimuon triggers with a reconstructed beam track and two or more reconstructed final-state tracks are written to secondary data tapes for analysis by the track-fitting program.

2. Track fitting

The track fitter assumes that tracks suffer smooth, continuous energy loss. It fits tracks by simultaneously varying the Coulomb scattering impulse in each module to minimize the χ^2 associated with the momentum fit. The algorithm calculates iteratively, rejecting information which makes a substantial contribution to the total χ^2, then performing a new fit. It fits trajectories which are found by the finding program and then attempts to constrain them to a common vertex.

Figure 11 diagrams the logical flow of the fitting routine. The initial fit to all tracks uses only MWPC information. The better drift chamber blob in each pair of blobs is then attached to the track. The fitting routine attempts to minimize the χ^2 of the fit and maximize the number of chambers on the track by removing hits from the track and replacing them with unattached DC blobs. Separate tracks, corresponding to a single track broken by the track finder, are fused. Halo tracks and tracks from stray muons are identified and discarded. A vertex is then chosen for dimuon triggers which possess a reconstructed beam track and at least two accepted final state tracks.
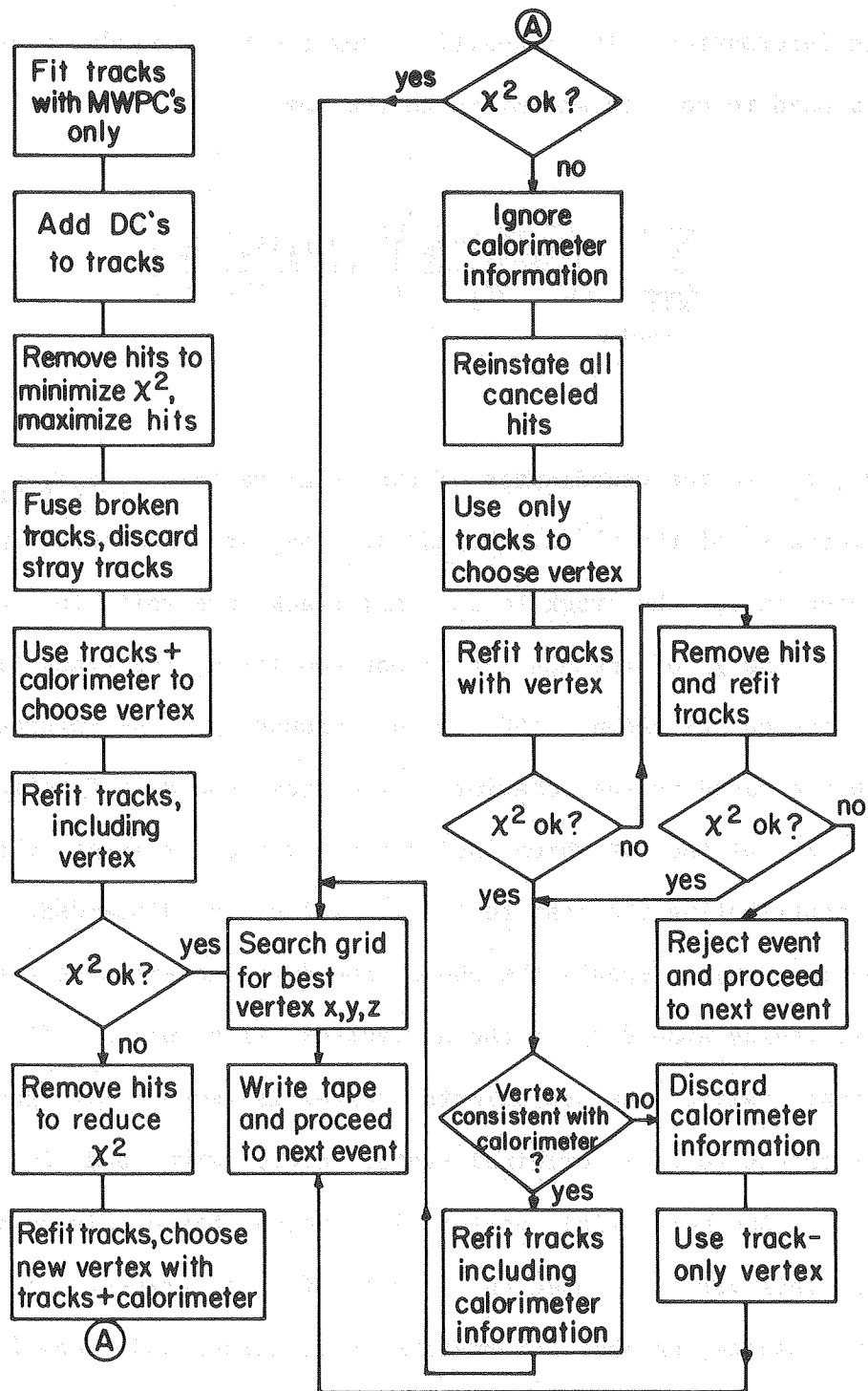
XBL 8010-2149

FIG. 11

The fitting program picks a trial vertex using track and calorimetric information. The z position from the track finder's vertex algorithm is used to compute and minimize the sum

$$\sum_{\substack{all \\ tracks}} \left(\frac{x_i(z_V)-x_V}{\Delta x_i}\right)^2 + \left(\frac{y_i(z_V)-y_V}{\Delta y_i}\right)^2 . \qquad (2)$$

Here, x_V, y_V, z_V are the coordinates of the trial vertex, $x_i(z_V)$, $y_i(z_V)$ are the coordinates of the ith track, and Δx_i, Δy_i are the uncertainties in the projection of the track to z_V. All tracks are refit to include the vertex. If the χ^2 of the new fit is not too large, the track fitter searches a region extending ± 50 cm in z around z_V. The interaction vertex is chosen based on the behavior of the above sum as a function of z. If the χ^2 of the fit which includes the vertex is large, chamber information contributing the most to the χ^2 value is discarded. The fitting routine then repeats the above procedure, determining a trial vertex and searching around z_V if the new vertex fits well. If this second attempt fails, the calorimeter vertex is temporarily ignored. Tracks are returned to their original state, before MWPC and DC hits were removed. Another trial vertex is chosen, based only on track information. This vertex is used in a refit of all tracks. If too large a χ^2 results, chamber information is discarded and a new fit is made. If the fit is still poor, the event is rejected. If the trial vertex is consistent with the track information, the z position determined by the calorimeter algorithm is included in a new fit. If the calorimeter vertex z coordinate is not consistent with the track

vertex, the calorimetric information is rejected and tracks are fit with only the track-determined vertex. If the calorimeter vertex agrees with the track vertex, a fit is done which includes the shower information. Once the track fitter selects a vertex for an event, the fitting for that event is finished.

The fitting algorithm uses an impulse approximation to describe the bending of muon paths in the spectrometer. Each module imparts a transverse momentum of 299 MeV/c. The fitting program assumes that the appropriate impulse is applied at one point between successive hits on a track. The estimate for the amount of energy lost by a particle is a function of energy and path length in matter. Multiple Coulomb scattering of particles is also described in the impulse approximation. The program simultaneously varies the transverse impulse in x and y in each module to determine a best fit to a trajectory.

The track fitting program corrects the beam energy as described in the previous section. The correction is applied to blocks of data, each containing about 5% of the full data sample. All events in a block have the same sign of beam muon and magnet polarity. The hadron calorimeter is calibrated separately for each data block as described previously. The fitting program uses the appropriate set of calibration constants for each event.

A series of cuts, to be described later, are applied to reconstructed events to discard data taken in kinematic regions where the spectrometer's acceptance changes rapidly. Before these cuts are made, 91% of the successfully analyzed events have reconstructed tracks which satisfy the dimuon trigger. After the cuts, 98% of the events meet this requirement. Because of this, no attempt is made to require

analyzed events to satisfy the μμ trigger after reconstruction.

To compute kinematic variables such as Q^2 and ν, the analysis programs must decide which final state muon is the scattered muon and which is the produced muon. The choice is obvious when the muons downstream of the interaction have opposite charges-- the scattered, or "spectator" muon is the particle with the same charge as the beam muon. If both muons have the same sign as the beam, the more energetic μ is chosen as the spectator. When applied to opposite sign pairs, this algorithm is successful 91% of the time.

The error in vertex placement varies from 15 cm to several meters. It depends in part on the opening angle of the final-state muon trajectories and the "cleanliness" of the calorimeter information. The rms momentum resolution is about 8% and varies inversely as the square root of the length of tracks in the spectrometer.

The track-finding program is able to reconstruct 39% of the exclusive dimuon triggers, where "exclusive" refers to events which satisfy only one trigger. Most rejected events emerge from the track finder with fewer than two final state tracks. The track-fitting program successfully analyzes 37% of its input from the track finder. Most failed dimuon triggers do not survive attempts to construct a vertex. These events largely are caused by noise such as shower activity in the detector and do not reconstruct to have two muons in the final state.

B. Acceptance modeling

A Monte Carlo simulation of the data is used to unfold detector acceptance from measured distributions. The Monte Carlo also allows an extrapolation of measured distributions into kinematic regions outside the acceptance of the detector. By using the calculation to estimate the ratio of observed to unseen events, total cross sections may be determined. To be successful, the simulation must accurately model the geometry and sensitivity of the spectrometer and must include effects such as energy loss and multiple scattering of muons. An acceptable model of the underlying physics governing interactions is needed to properly describe acceptance and to allow extrapolation outside the measured kinematic region.

The Monte Carlo simulation of the Multimuon Spectrometer consists of two parts, a shell and a physics generator. The shell describes the detector, propagates particles through the spectrometer, and writes simulated data tapes when an imaginary interaction satisfies an event trigger. The physics generator contains the model for the process being studied and produces daughter particles and hadronic showers with distributions intended to mimic actual interactions. Generators for charm production, deep inelastic scattering, vector-meson production, and π, K production are among the routines that have been used with the Monte Carlo shell.

The shell uses randomly sampled beam muons recorded as straight-through triggers during the course of the experiment. The program propagates beam muons from the front of the spectrometer to

interaction vertices, causing the muons to suffer both uniform and stochastic energy losses from effects such as μ-e collisions, direct electron pair production, and muon bremsstrahlung. Simulated muon trajectories are bent by the magnetic field and are deflected by single and multiple Coulomb scattering processes. A nuclear form factor is used in the description of large-angle scatters. Daughter muons bend, lose energy, and multiple scatter in the same way. One of the physics generators creates charged π and K mesons and causes them to interact or decay after traveling through typically half a module. Mesons lose energy and Coulomb scatter appropriately. All muons are traced through the spectrometer until they leave the detector or stop. Interactions which satisfy any of the experimental triggers are encoded and written to tape with the same format as was used to record real events.

The shell assumes that the efficiency of the drift chambers is 100% and the efficiency of the MWPC's is less, as described earlier. Wire chamber hits are generated to represent particles traveling through the MMS and showers developing downstream of an interaction. Halo muons, δ-rays, and out-of-time beam particles are not simulated. Only a minimal attempt is made to model the spreading of hadronic showers through the chambers.

A photon-gluon-fusion (γGF) model for charmed quark production, described earlier, serves as the heart of the physics generator used to study detector acceptance for charm. The expression for the γGF cross section is given in Appendix A.

Charmed quark pairs are produced quasi-elastically in γGF, that is, the $c\bar{c}$ pair carries off most of the energy of the virtual photon. To allow the model to make quantitative predictions, the charmed quark

mass, m_c, is set to 1.5 GeV/c^2.[14] The distribution for the gluon momentum fraction x_g is taken to be $3(1-x_g)^5/x_g$. Here, x_g is $(Q^2 + m^2_{c\bar{c}})/(2M\nu)$. The strong coupling constant α_s is $1.5/\ln(4m^2_{c\bar{c}}) \approx 3/8$. Figure 12(a) shows the $m_{c\bar{c}}$ pair mass spectrum that results; the average pair mass is 4.9 GeV/c^2. Only those events with $m_{c\bar{c}} \gtrsim 2m_D$ are allowed to generate final states containing open charm.

One-tenth of the beam muons which produce charm interact coherently with iron nuclei while the rest interact incoherently with nucleons in Fermi motion. The γGF model does not describe the dependence of the production cross section on $-t$, the square of the four-momentum transferred to the target. Coherence, screening, and $-t$ dependence are parametrized in a fashion identical to that used to describe ψ production[15] through

$$\frac{d\sigma}{dt}(\gamma Fe \rightarrow c\bar{c}X) = \left\{ A_e^2 \; e^{150t} + A_e \left[\frac{7}{8}e^{3t} + \frac{1}{8}e^t \right] \right\} \frac{d\sigma}{dt}(\gamma N \rightarrow c\bar{c}X) \Big|_{t=0}. \qquad (3)$$

The effective atomic number, A_e, is taken to be 0.9 times 55.85 based on measurements of screening from SLAC.[16] The coherent slope is unresolved in our ψ data and is based on lower energy photon-nucleon measurements.[17]

A prescription to describe the fragmentation of quarks into hadrons, and the semi-leptonic decay of those hadrons, is necessary to connect the γGF predictions with experimentally observable results. The Monte Carlo uses a two-stage fragmentation to turn the charmed quarks into hadrons. The first describes the escape of the $c\bar{c}$ pair from the vicinity of the target nucleon. In the spirit of γGF, the pair moves

away from the production vertex with minimal interference from the target. The exchange of soft gluons to "bleach" the color from the quark pair is ignored. The $c\bar{c}$ system absorbs the maximum allowable amount of energy from the virtual photon. The second stage describes the fragmentation of the $c\bar{c}$ into D mesons. A function $D(z) = (1-z)^{0.4}$ parameterizes the breakup, where, if E_D^* is the energy of a charmed particle in the $c\bar{c}$ center of mass, $z = 2E_D^* / m_{c\bar{c}}$ represents the fraction of the maximum possible energy the meson receives. $D(z)$ is based on SPEAR data[18] taken at center of mass energies comparable to typical values of $m_{c\bar{c}}$ in the γGF model. The SPEAR data measure inclusive D production and therefore include information on D^* production with the subsequent decay $D^* \rightarrow D X$.

The Monte Carlo allows the charmed quarks to fragment into neutral and charged D's in a 2:1 ratio.[18] The ratio is based on the same SPEAR measurements which yielded the function $D(z)$. Other charmed states such as $F\bar{F}$ and $\Lambda_c\bar{\Lambda}_c$ are not explicitly simulated. Any difficulties caused by limiting the variety of particles produced by the $c\bar{c}$ pair are present only to the extent that the unmodeled states decay with characteristics different from those of a $D\bar{D}$ state. The average values of Q, the available kinetic energy in typical semileptonic decays of F's and Λ_c's, differ by $\sim 10\%$ from the average Q in the simulated decay modes. This results in different $p_{||}$ and p_T spectra for the different decay modes where $p_{||}$ and p_T are muon momentum components parallel and perpendicular to the virtual photon. Monte Carlo calculations indicate that acceptance is much more sensitive to $p_{||}$ than p_T. The data and Monte Carlo agree to 15% in p_T; studies of systematic uncertainties, described below, include investigation of the sensitivity of our measurements to

$p_{||}$ spectra.

The simulation assumes the branching ratios of 4% and 20% for D^0, $\overline{D^0}$ and D^+, $D^- \to \mu \nu X$ respectively.[19,20] X is taken to be $K^*(892)$ 39% of the time and K 61% of the time.[20] The net yield of muons per $c\bar{c}$ pair is 0.187 with the above assumptions. To permit proper modeling of the shower energy and missing (neutrino) energy, D's are allowed to decay to $e\nu X$ with the same branching fractions.

The Monte Carlo was used to generate a data set of simulated events representing a beam flux equivalent to that producing the real data reported here. In all, 2.87×10^5 incoherent and 3.30×10^4 coherent Monte Carlo interactions produced 4.49×10^4 and 8.4×10^3 triggers, respectively. The trigger efficiency for γGF events with decay muons is therefore 16.7%.

Figure 12(b) shows the Q^2 distributions for events which were generated by the charm model and which satisfied the simulated trigger. The spectrometer's acceptance is remarkably flat in Q^2 due to its "no-hole" construction and forward sensitivity. This is evident in the minimal difference in the shapes of the generated and triggered spectra. Figure 12(c) shows distributions in ν, the energy lost by the beam muon. The different shapes of the generated and triggered plots are caused to great extent by the calorimeter subtrigger. For values of ν close to the beam energy, the requirement that the scattered muon travel through more than six modules has a strong effect. Spectra of daughter muon energies are shown in Fig. 12(d). Since daughter muons must travel through at least six modules to satisfy the dimuon trigger, the detector's acceptance for slow muons is small. The energy loss per module experienced by a muon is about 1 GeV and the transverse momentum
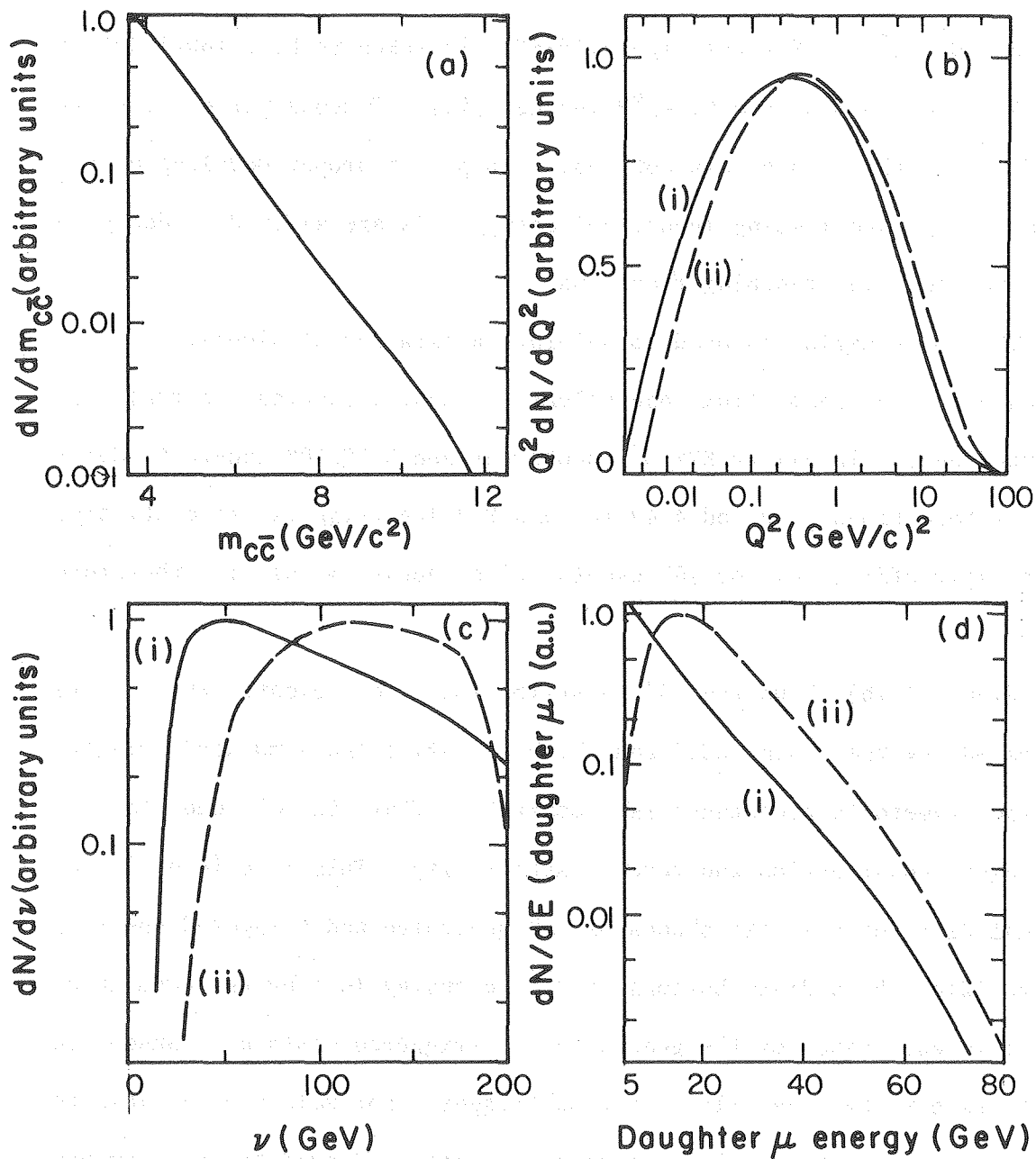
XBL 8010-2144

FIG. 12

imparted by the magnetic field is about 300 MeV/c. Soft muons are stopped or slowed and pitched out of the spectrometer before they can trigger the apparatus.

The data presented in Fig. 12 include both same-sign and opposite-sign final-state muon pairs. After reconstruction, the acceptance for opposite-sign pairs is higher by a factor of 1.45. This is because daughter muons with sign opposite to the beam's bend back into the spectrometer after the beam has partially bent out while traveling to the interaction vertex. After analysis cuts described below, the factor decreases to 1.26.

The comparison between data and Monte Carlo samples will be discussed later.

C. Background modeling

The experiment identifies charmed states by their $\geq$ three-body decays into muons. Since decays such as $D \rightarrow K\pi$ contribute only to the calorimeter signal, none of the kinematic distributions can exhibit an invariant-mass peak representing charm production. To allow extraction of the charm signal, important sources of contamination must be modeled and subtracted from the data. If the spectrometer had measured two-body decays which yield charm mass peaks, the experimental data would provide all the necessary background information. A smooth curve could be extrapolated under the mass peak, allowing accurate determination of

signal-to-background ratios. Since this is not the case, a Monte Carlo simulation of the major background is used to remove non-charm contamination from the data.

The largest source of background is the decay-in-flight of π and K mesons produced in inelastic muon-nucleon collisions. Other sources of contamination are muon trident production $\mu N \to \mu \, \mu^+ \mu^- X$, τ pair production $\mu N \to \mu \tau^+ \tau^- X$ with $\tau \to \mu X$, and bottom meson production $\mu N \to \mu B \bar{B} X$ with B or $\bar{B} \to \mu X$.
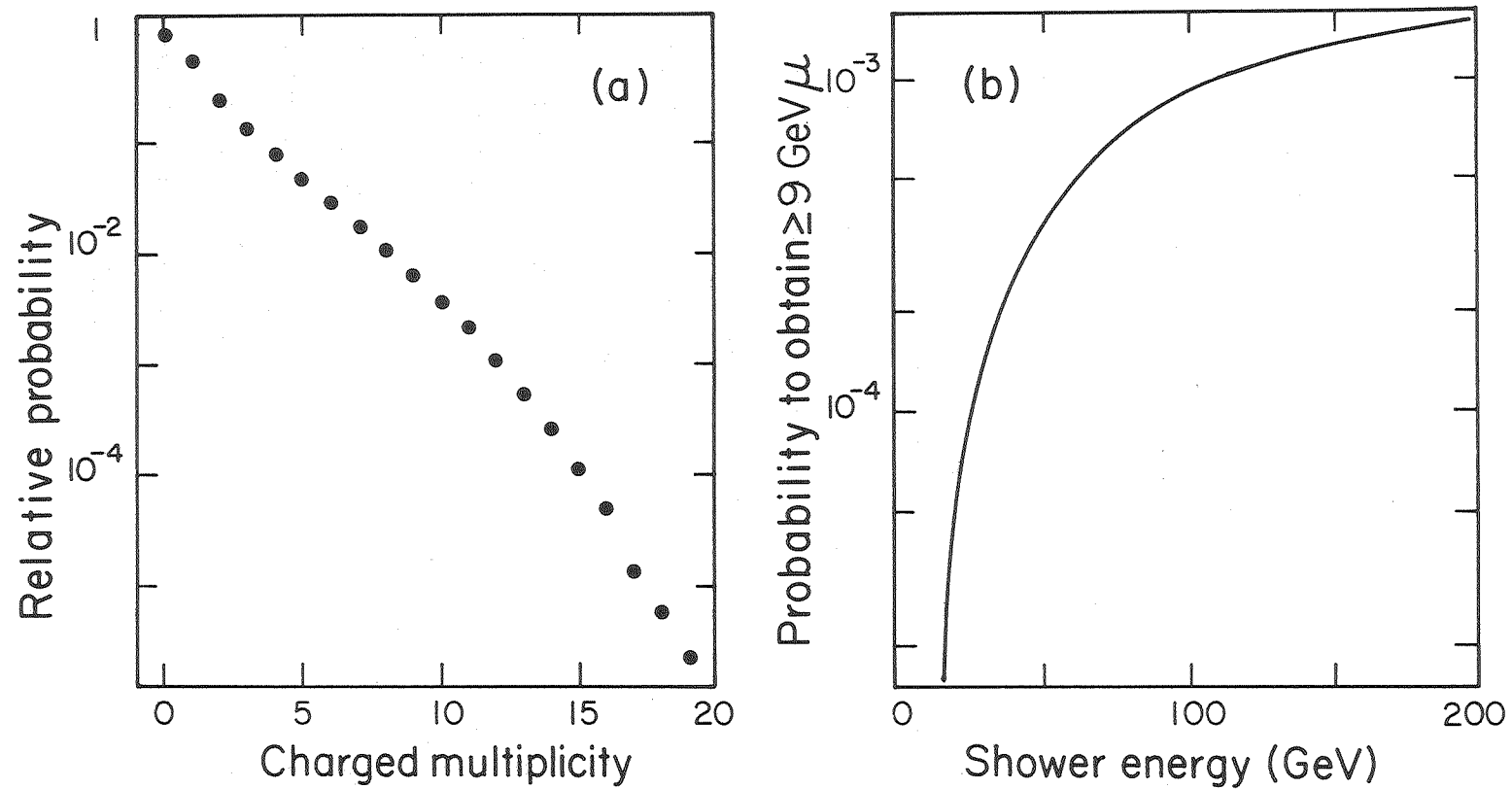
1. π, K decay

The average density of the Multimuon Spectrometer is 4.7 gm/cm^3, six-tenths that of iron. Because of this, most π and K mesons produced in a hadronic shower interact and stop in the detector before decaying. For a 20 GeV π in the MMS the total decay probability is about 4×10^{-4}, while for a 20 GeV K$^+$ it is 4×10^{-3}. This indicates that perhaps a tenth of a percent of the inelastic muon-nucleon collisions in the spectrometer will give rise to a shower-decay muon. Since theoretical estimates predict charm muoproduction cross sections that are a percent or less of the total inelastic cross section, accurate simulation of the π, K decay background is necessary.

A shower Monte Carlo based only on experimental data measuring muon-nucleon and hadron-nucleon interactions is used to study the π, K-decay background. Parametrizations of muon-nucleon scattering[12] and

hadron muoproduction [21,22] cross sections from the Chicago-Harvard-Illinois-Oxford collaboration (CHIO) fix the Monte Carlo's absolute normalization. Bubble chamber data are used to describe the interactions of pions and kaons with target nuclei[23-38] as the shower develops in the detector. The simulation creates a full shower until all charged particles have energies less than 5 GeV. Figure 13(a) shows the charged multiplicity for simulated showers. Once the hadronic cascade has been generated, the Monte Carlo chooses which, if any, of the shower mesons to let decay. The shower simulation is described in more detail in Appendix B.

The physics generator for the π, K Monte Carlo is used with the standard MMS shell described earlier. The shell manipulates beam information, generates simulated raw data, propagates muons, etc. The propagation routine allows π's and K's to travel through the spectrometer for the distance requested by the generator. Mesons lose energy, multiple Coulomb scatter, and bend in the magnetic field.

The total cross section for muon production via π, K-decay is a convolution of the inelastic scattering cross section with the probability that a decay muon comes from the hadron cascade. The average beam energy at the interaction vertex is 209 GeV. With that energy and the beam's observed momentum spread, the inelastic cross section to scatter with $\nu > 10$ GeV is 3.54 μb. The cross section to scatter and produce a decay muon with energy greater than 5 GeV is 2.28 nb. The combined trigger and reconstruction efficiency for these events is 4.6%. Figure 13(b) shows the probability vs. ν for a shower to produce a muon with energy greater than 9 GeV. The absolute normalization of the Monte Carlo predicts that after reconstruction but

XBL 8010-2140

FIG. 13

before analysis cuts, 43% of the dimuon signal is from π, K decay. After the analysis cuts described below, the decay contamination drops to 19%.

The Monte Carlo was used to generate a data sample corresponding to 1/3.915 times the beam flux represented by the data to be discussed. All π, K-decay distributions and their errors are scaled by 3.915 to compare data with Monte Carlo.

It is important to have confirmation that the predictions of the shower Monte Carlo are reasonable. Since most reconstructed π, K events have a muon from the decay of a primary shower meson, data in agreement with the CHIO results would provide this check. Unfortunately, other experiments which have studied hadron production by charged leptons have used lower energy beams.[39] The only possible tests of the simulation are indirect.

One check compares the missing (neutrino) energy predicted for π, K events with that observed in the data. The meson momentum spectrum is sharply peaked at low momentum. This is caused by the approximate $\exp(-3.5x_F)$ Feynman x spectrum exhibited by primary mesons[21] combined with the $(1-x_F)^4$ shape[26] which describes secondary production. Since the spectrometer's acceptance for slow muons is small, decay muons produced in the forward direction are strongly favored. A forward decay muon is accompanied by a neutrino with very little energy in the laboratory. The γGF charm model suggests that charmed quarks tend to receive half of the virtual photon's energy. Though fragmentation and decay kinematics exert a strong influence on muon energies, the parent distribution of quark momenta is not sharply peaked at low momentum. Charmed particles tend to have more energy in the laboratory than shower

mesons so observed muons from charm can be produced in a wider angular range. As a result, charm events should show significantly greater missing energy. This is found to be true; the comparison between data and Monte Carlo missing energies will be discussed below.

Another effect influences the missing energy distributions for π, K and charm events. The probability for a π or K to decay in flight is proportional to $1/E$ where E is the meson's energy, while the probability for a charmed particle to decay promptly is independent of energy. This $1/E$ dependence favors slow π's and K's with a forward decay muon over faster shower mesons with more decay phase space in the acceptance of the MMS.

The results of the shower Monte carlo are consistent with the rates predicted by a Monte Carlo used by the Caltech-Fermilab-Rockefeller (CFR) neutrino experiment.[40] The CFR program uses a model by Feynman and Field [41] to generate a neutrino-induced primary shower. Data taken by CFR with incident pions are used to parametrize secondary interactions of shower mesons. The CFR Monte Carlo predicts muon yields in agreement with those predicted by our shower simulation for 75 GeV showers, 10% higher for 100 GeV showers, 15% higher for 125 GeV showers, and 25% higher for 150 GeV showers. The average shower energy in this experiment is 87 GeV.

2. Muon tridents, τ pairs, bottom mesons

Other sources of background to the charm signal include muon tridents, τ pairs with muonic decay of one τ, and bottom meson pairs with muonic decay of one or both mesons. Each has been investigated and will be described.

The authors of Ref. 43 have studied the contribution of electromagnetic muon tridents to the multimuon signal which might be seen by a muon experiment. Since most tridents are not accompanied by significant shower activity, their calculation predicts that tridents which satisfy the dimuon trigger and are reconstructed as two-muon events should contaminate the data at the level of 1/2%. The trimuon final state trigger rate predicted by their calculation, when patched into a crude simulation of the MMS, provides a consistency check of the dimuon information. This check confirms that electromagnetic tridents are a small background to charm production.

Another upper limit on the trident background comes from the study of events with three muons in the final state which satisfied the dimuon trigger. This test checks the consistency of the data with the hypothesis that all the dimuon triggers with three reconstructed final-state tracks result from charm production followed by the muonic decay of both charmed particles. The production process and charm decay kinematics are assumed to be described by the γGF model discussed earlier. The charm Monte Carlo is normalized so that it predicts the same number of dimuon events after reconstruction and cuts as are present in the data after subtraction of the expected π, K-decay

background. All data events and γGF events which satisfy the dimuon trigger with three reconstructed tracks are subjected again to analysis cuts after the analysis is blinded to the softest final-state track. After cuts, 720 data events and 706 Monte Carlo events remain. Including statistical errors, the Monte Carlo accounts for (98 ± 5)% of the data. This suggests that most 2μ events which result from partial reconstruction of 3μ final states come from charm systems, not muon tridents. Less than one-fifth of the simulated dimuon triggers are caused by 3μ charm events. Consequently, other sources of 3μ events which feed down to the 2μ sample should account for a negligible fraction of the data. We conclude that the dimuon background from partially reconstructed muon tridents is small and neglect it.

τ leptons can decay into hadrons and neutrinos. A τ pair can therefore satisfy the dimuon full trigger through decay combinations like $\tau^+ \to \pi^+ \bar{\nu}_\tau$, $\tau^- \to \mu^- \bar{\nu}_\mu \nu_\tau$. The reduction in the trigger rate from muon tridents provided by the calorimeter subtrigger therefore does not apply to τ pair events. Fortunately, the kinematics of lepton production reduces the cross section for τ production by a factor of $(m_\mu/m_\tau)^2 = 3.4 \times 10^{-3}$ relative to trident production.[42] Including the 17.5% $\tau \to \mu \nu \bar{\nu}$ branching ratio reduces the ratio of τ production with a single decay muon to trident production to approximately 10^{-3}. The calorimeter subtrigger reduces the dimuon trigger rate only by a factor of 160, so the τ background should be about 0.1%, even less than the trident background. Since the masses of the τ and D are nearly equal, replacing the $c\bar{c}$ by a $\tau^+ \tau^-$ and the gluon by a photon in Fig. 1(c) allows a comparison of the charm and τ cross sections. The ratio is approximately $(\alpha/\alpha_s)^2$ or 10^{-3}, consistent with the above estimate.

Consequently, the background from τ pairs is neglected.

The γGF model predicts a bottom meson production cross section which is less than 0.03% of the charm cross section.[43] Bottom pairs should be seen as dimuon events and as events forming exotic charge combinations like $\mu^+ N \rightarrow \mu^+ \mu^- \mu^- X$ from cascade decays through charm. The small number of exotic events and events with four or five muons in the final state confirms that bottom production is not a significant background to charm production. Our 90%-confidence upper limit on the cross section for Υ production[44] confirms this conclusion. Even if the bottom production cross section times muonic branching ratio were 100 times that for Υ's, $B\bar{B}$ states would comprise less than 5% of the data.

D. Extracting charm from the data

Raw data and simulated raw data from the γGF and π, K-decay Monte Carlo simulations are analyzed in an identical fashion. Histograms for data and Monte Carlo are generated with the same reconstruction and analysis cuts. After the π, K histograms are scaled by 3.915 they are subtracted bin-by-bin from the data histograms, yielding distributions for charm. Statistical errors quoted for charm spectra include the error on the subtraction. Systematic errors associated with this procedure will be discussed below.

Cuts applied to data and Monte Carlo events serve several purposes. Events whose reconstruction is dubious can be discarded. Data in

kinematic regions where the detector's acceptance changes rapidly or is poorly understood can be rejected. Cuts which favor charm over π, K decay can improve the data's signal-to-background ratio.

A number of cuts pass events which are well reconstructed. The vertex selection is checked by requiring the difference between the z position of the track-fitting program's vertex and the calorimeter algorithm's vertex to be greater than -60 cm and less than +65 cm. The incident energy of the beam muon must lie between 206 GeV and 226 GeV. The χ^2 for the fit to the beam track must be less than 10 for four degrees of freedom in the horizontal view and less than 7.5 for three degrees of freedom in the vertical view. An aperture cut passes events whose beam muons did not enter the iron of the enclosure 104 dipoles. Events must have exactly two reconstructed final-state tracks. Each track must have horizontal and vertical χ^2 fits with less than 4.5 and 3.5 per degree of freedom, respectively. The number of degrees of freedom for tracks in the MMS depends on the length of the tracks. Data which satisfy only the dimuon, and not the trimuon, trigger are passed. Reconstructed tracks are projected upstream to the vertex and downstream until they leave the MMS. These "extended" tracks must be missing no more than four MWPC hits between the hit furthest downstream on the track and the point where the extended track leaves the detector. There must be no more than six missing chamber hits between the vertex and the hit furthest upstream on the track. To reject events associated with a shower entering the front of the spectrometer, the MWPC upstream of the first module must contain fewer than ten hits. Reconstructed tracks must differ sufficiently in curvature and direction to represent distinct muon trajectories. Two requirements discard events in which a

stale track has been interpreted as the trajectory of a produced muon. The difference between the z momentum of the beam and the sum of the z momenta of final-state tracks must be greater than -18 GeV/c. The ratio of the energy lost by the beam muon to the energy observed in the final state (the sum of the muon energies and the shower energy) must be greater than 0.6.

Several analysis cuts exclude data from kinematic regions where the spectrometer's acceptance changes rapidly or changes in a way which is poorly modeled. Reconstructed tracks are required to have at least 15 GeV/c of momentum. Events are required to have more than 36.5 GeV of shower energy. Reconstructed vertices must lie between the centers of the first and eighth modules. To increase the signal-to-background ratio, daughter muons are required to have at least 0.45 GeV/c momentum perpendicular to the scattered muon. In addition, the beam muon is required to lose at least 75 GeV of energy.

The dimuon sample shrinks from 82 026 events after reconstruction cuts to 20 072 events after both reconstruction and analysis cuts are applied. The π, K-decay background drops from 43% of the data to 19% of the data. Qualitative features of the data and further justification for some of the individual analysis cuts will be discussed below.

E. General features of the data

Figure 14 shows distributions for the two Monte Carlos and data

after subtraction of the π, K-decay background. Events in the histograms survived reconstruction and cuts; acceptance has not been unfolded. Events in Fig. 14(a) pass all the analysis cuts except that no daughter energy requirement is made and all events are required to have $\nu \gtrsim 150$ GeV. The unusual ν cut increases the sensitivity of the predictions of the Monte Carlo simulation to assumptions about charmed quark fragmentation. The inverted histogram represents the π, K Monte Carlo, absolutely normalized to the beam flux and scaled as described earlier. The upright histogram represents data after subtraction of the π, K histogram. The smooth curve shows the prediction of the γGF model, normalized to the data after the standard analysis cuts are applied. The horizontal bar indicates the rms resolution at 30 GeV. Figure 14(a) makes clear the need for a daughter energy cut. Though both Monte Carlo samples, and presumably the data, heavily populate the region of low daughter energy, the detector's acceptance is too small to allow reconstruction of many of these events. All other histograms and results do not include events with daughter energy less than 15 GeV.

The probability to obtain a calorimeter subtrigger as a function of shower energy is shown in Fig. 7. Because of the curve's steep rise at low energy, a minimum shower energy requirement of 36.5 GeV is imposed.

Since the beam bends out of the detector while traveling through it, tracks of daughter muons with the same charge as the beam tend to become shorter as the vertex moves downstream. Inaccuracies in the Monte Carlo's algorithm used to inject shower-induced hits into the wire chambers have the greatest effect on short tracks and therefore on events occuring in the downstream half of the spectrometer. By cutting on the location of the vertex in the spectrometer the data whose
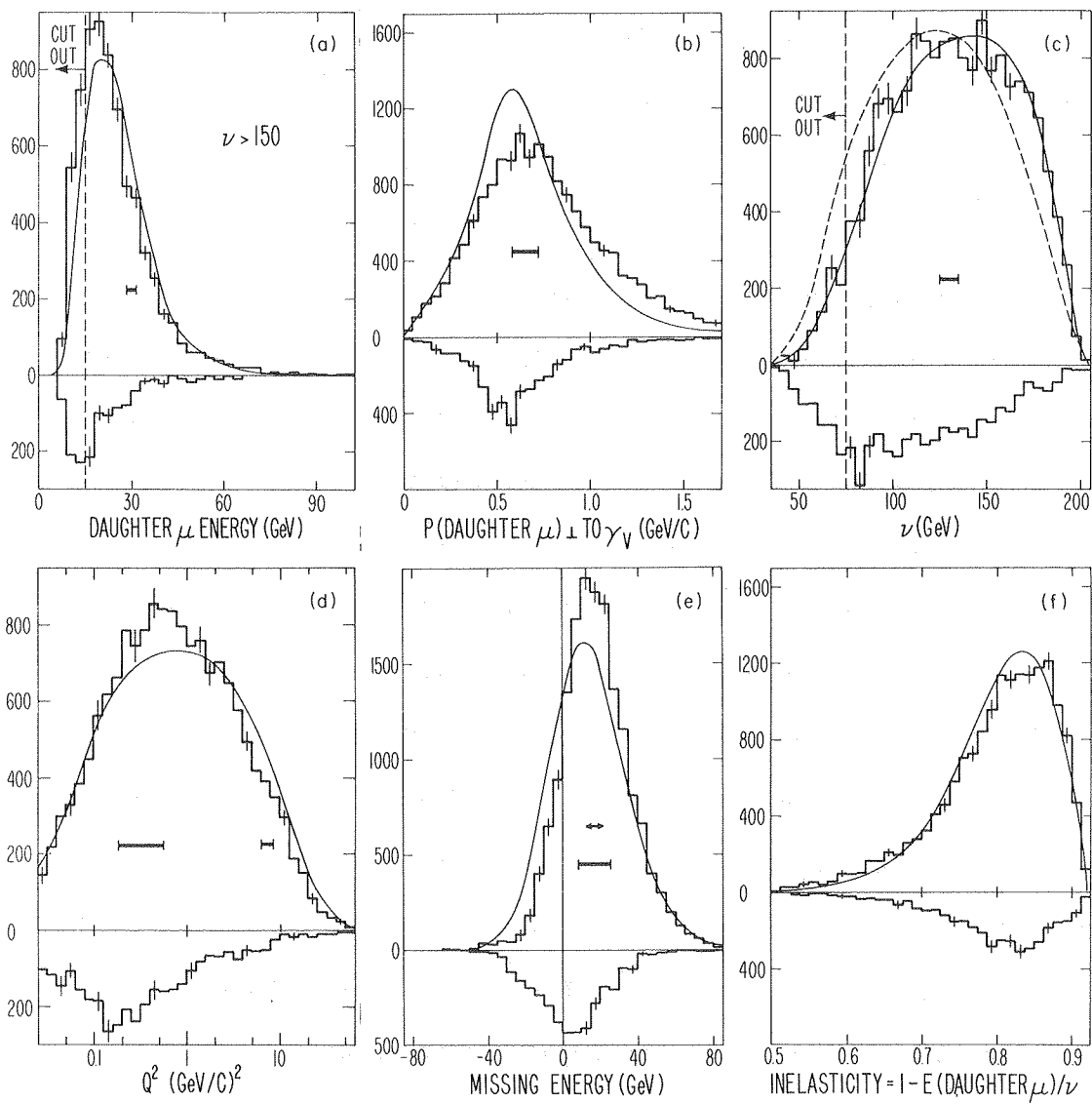
FIG. 14

XBL 8011-7421

acceptance is not well modeled can be discarded.

The momentum of the daughter muon perpendicular to the virtual photon is shown in Fig. 14(b). As in Fig. 14(a), data, γGF, and π, K Monte Carlo events are shown. The horizontal bar indicating rms resolution is 0.15 GeV/c wide. The cut requiring 0.45 GeV/c daughter momentum perpendicular to the scattered muon essentially demands that the daughter μ have a p_T which is nonzero by at least 3σ. The number of tridents contaminating the data is further reduced by this cut. Mean p_T for the background-subtracted data is 15% higher than for the charm Monte Carlo. This variable is sensitive to assumptions about $-t$ dependence, not part of the γGF model, so the disagreement does not necessarily reflect a problem with the charm production model.

Figure 14(c) shows the energy lost by the beam muon for data and both Monte Carlo data sets. All canonical cuts except the ν cut are imposed. The horizontal bar illustrates rms resolution. The agreement between subtracted data and Monte Carlo is spectacular. The π, K-decay events have lower average ν. The ratio of π, K to subtracted data is small for large ν but is of order unity for $\nu \lesssim 75$ GeV. To reduce sensitivity to the absolute normalization of the shower Monte Carlo, data with $\nu \lesssim 75$ are discarded. The dashed curve shows the predictions of the charm Monte Carlo when the γGF ν dependence is replaced by a flat ν dependence and the fragmentation is changed to $D(z) = \delta(z-1)$.

The Q^2 distributions are shown in Fig. 14(d). Horizontal bars indicate rms resolution. The π, K events tend to have lower Q^2 than the subtracted data. The γGF model predicts a Q^2 spectrum that is slightly higher than observed.

Figure 14(e) presents the missing energy for subtracted data and

the two Monte Carlos. As expected, the mean missing energy is substantially less in the π, K sample than in the charm sample. The mean missing energies are 4.45±0.53 GeV, 14.59±0.18 GeV, and 18.18±0.24 GeV for π, K Monte Carlo, γGF Monte Carlo, and subtracted data. The horizontal bar indicates rms resolution and the arrow shows the change in the centroid of the data which results if the calorimeter calibration is varied ±2.5%. The relationship between shower energy and pulse height used in both Monte Carlos is fixed by deep inelastic scattering events as described above. This is an accurate description for π, K-decay events since they essentially are inelastic scattering events. The showers in charm events, in the γGF picture, are caused by the decay products of the charmed particles since very little energy is transfered to the target nucleon. Charm decays almost always include K's in the final state. Since K's have shorter lifetimes and longer absorption lengths than π's, there is no reason to expect that the signature of a charm shower, which may be initiated by two K's and a π, will exactly match that of an inelastic μN collision, which usually does not contain fast strange particles.[22]

Figure 14(f) shows the inelasticity for data and Monte Carlos. Inelasticity is defined as 1 - E(daughter μ)/ν.

Mean values of reconstructed ν, Q^2, daughter energy, inelasticity, missing energy, and momentum perpendicular to the virtual photon are presented in Table 2. Particularly in the case of ν, daughter energy, and missing energy, the tabulation excludes the possibility that the dimuon data can be explained by π, K-decay.

F. Systematic errors

After reconstruction, cuts, and background subtraction, the data contain 16 376 events attributed to the production and muonic decay of charmed particles. To understand the limitations on the accuracy of results presented here, systematic errors must be investigated. Systematic effects can come from two sources. The backgrounds to charm production may be described incorrectly or the acceptance of the muon spectrometer for charm events may be simulated inaccurately.

The predictions of the shower Monte Carlo are sensitive to the K/π ratio in primary showers. This is the information which is least well determined by CHIO.[21,22] To gauge the Monte Carlo's sensitivity to this ratio, showers were generated with K/π ratios of 0.4 for both signs, ~three times greater than those reported in Ref. 22. Simulated trigger rates increased by 60% and the number of shower events surviving the standard cuts increased by 73%.

Since only 10% of the π, K events passing analysis cuts come from the decay of secondary hadrons, the predictions of the simulation are not sensitive to assumptions made about the interactions of primary hadrons in the detector.

A synthesis of charm and shower Monte Carlo samples provides a consistency check. The data are represented as a combination of both simulations. By seeing how the relative normalizations must be changed to fit different kinematic distributions of the data, an estimate of the accuracy of the Monte Carlos was obtained. It is not correct to fix the π, K normalization this way since it then becomes impossible to test the γGF model against the data.

We conclude that the background description provided by the shower Monte Carlo is accurate to within 50%. Therefore, after analysis cuts, our best estimate is that the decay in flight of π and K mesons contributes $(19 \pm 10)\%$ of the dimuon signal where the quoted error is systematic.

The acceptance of the muon spectrometer is by far most sensitive to the energy spectrum of produced muons. The γGF model describes quasi-elastic charm production; that is, the $c\bar{c}$ pair receives most of the energy of the virtual photon. The charm model accurately predicts the ν dependence of the subtracted data. Varying the fragmentation function $D(z)$ used to create D's from $c\bar{c}$ pairs allows investigation of this sensitivity. $D(z)$ provides the link between ν, which is correctly modeled, and daughter energy. The form for $D(z)$ used[18] in acceptance modeling is $D(z) = (1-z)^{0.4}$. Remodeling with $D(z) = (1-z)^3$ and $D(z) = (1-\min(z,0.99))^{-1.5}$ changes the detector acceptance by -19% and $+20\%$, respectively. The exponents in the "too soft" and "too hard" functions are more than 5σ from the value determined at SPEAR.[18] The mean daughter energies which result are presented in Table 3. Agreement in energy and other distributions is spoiled by using the alternative fragmentation descriptions.

When same-sign dimuon data and opposite-sign dimuon data are analyzed separately, little change is seen in data-to-Monte Carlo ratios. Cross sections based only on same-sign or opposite-sign events differ by 3.5% from those based on both signs.

Systematic uncertainties in π, K modeling and charm modeling are not expected to be significantly correlated. An estimate of the total systematic error is made by reanalyzing the data with different

assumptions. Errors are parametrized by (1) decreasing, (2) increasing by 50% the subtracted shower background and by recalculating the acceptance with the (3) softer, (4) harder fragmentation function. The effects on results are obtained by reanalyzing the data with each of the four systematic changes, adjusting the γGF normalization to yield the observed number of events past cuts, and replotting or recalculating acceptance-corrected information. All positive deviations from the canonical results are added in quadrature to yield the positive systematic error and all negative deviations are added in quadrature to yield the negative systematic error. The results define bands of systematic tolerance around observed distributions. Cross sections presented in the next section will include systematic errors of +28% and -20%.

IV. RESULTS AND DISCUSSION

This section describes the acceptance correction and presents measurements of charm production by muons and virtual photons. Results include the total diffractive cross section for muoproduction of charm and the Q^2 and ν dependence of virtual photoproduction of charm. The cross section for charm production by real photons and its contribution to the rise in the photon-nucleon total cross section are discussed. A lower limit on the ψ-nucleon total cross section is presented. The role played by charm in the scale-noninvariance of muon-nucleon scattering at low Bjorken x, $Q^2/(2M\nu)$, is described.

A. Acceptance correction

Most spectra presented in the following sections are differential in Q^2 or ν. To unfold the experimental acceptance, data, π, K-decay Monte Carlo, and γGF Monte Carlo are placed in $(\ln(Q^2), \ln(\nu))$ bins. If $\Delta\sigma(Q^2, \nu)$ is the number of events in the $(\ln(Q^2), \ln(\nu))$ bin which includes the values Q^2 and ν, the ratio of subtracted data to charm Monte Carlo in a bin is

$$\frac{\Delta\sigma(\text{data}) - \Delta\sigma(\pi, K)}{\Delta\sigma(\gamma GF)} . \tag{4}$$

For small bins, the ratio of the acceptances for subtracted data and charm Monte Carlo will be constant across the width of a bin. Because of resolution smearing, the measured average values of Q^2 and ν in a bin will generally differ from the true average values. The charm Monte Carlo is used to calculate the shift between measured and true mean Q^2 and ν. The acceptance-corrected differential cross section which results is

$$\frac{d^2\sigma(\text{charm})}{dQ^2 d\nu} = \frac{d^2\sigma(\gamma GF)}{dQ^2 d\nu} \; \frac{\Delta\sigma(\text{data}) - \Delta\sigma(\pi, K)}{\Delta\sigma(\gamma GF)} \; . \tag{5}$$

Here, $\sigma(\text{charm})$ is the cross section for charm production by muons and Q^2 and ν are the corrected average values in the bin. This procedure, which equates real cross sections with Monte Carlo cross sections weighted by the ratio of subtracted data to Monte Carlo, is used to obtain the results presented in the following sections.

3. Diffractive charm muoproduction cross section

The measured cross section for diffractive charm production by 209 GeV muons is $6.9^{+1.9}_{-1.4}$ nb. "Diffractive production" refers to the creation of $c\bar{c}$ pairs carrying most of the laboratory energy of the virtual photon, as in the γGF and VMD models. This analysis is insensitive to mechanisms which might produce charm nearly at rest in the photon- nucleon center of mass. The cross section is computed by

multiplying the γGF prediction of 5.0 nb by the ratio of subtracted data to γGF Monte Carlo. A total of 20 072 data events, 944 π, K Monte Carlo events (scaled to 3696 events), and 13 678 γGF Monte Carlo events survived reconstruction and analysis cuts to contribute to this ratio. The error on the cross section is systematic and reflects uncertainties in background subtraction and acceptance modeling, as described earlier. The statistical uncertainty is negligible compared to the systematic error. Ignoring nuclear shadowing and coherence would raise the reported cross section by 9.4%. After a (26±5)% relative acceptance correction, the opposite-sign to same-sign ratio for background-subtracted data is 1.07±.06.

A Michigan State-Fermilab (MSF) experiment has reported a cross section for charm production by 270 GeV muons of 3±1 nb.[45] Correcting the beam energy to 209 GeV with the γGF model reduces the MSF cross section to 2.1±0.7 nb. The MSF data contain 412 fully reconstructed dimuon events; the collaboration simulates detector acceptance with a

phenomenological model containing three free parameters.[46] Their choice of parameters was based on a sample of 32 dimuon events observed earlier at a beam energy of 150 GeV.[47] The 150 GeV sample contained an estimated 4.9 trident events and a small, but unspecified, number of π, K-decay events.

C. Virtual and real photoproduction of charm

In the single-photon approximation, the μ-N interaction is described as the absorption by the target of a virtual photon from the beam particle. The differential charm production cross section may be written

$$\frac{d^2\sigma}{dQ^2 d\nu} = \Gamma_T \sigma_T + \Gamma_L \sigma_L \ . \tag{6}$$

The factors Γ_T and Γ_L represent the fluxes of transversely and longitudinally polarized virtual photons with mass^2 $-Q^2$ and energy ν. The terms $\sigma_T(Q^2,\nu)$ and $\sigma_L(Q^2,\nu)$ are the cross sections for photons of the two polarizations to be absorbed by the target to yield charmed particles. More compactly, defining $\varepsilon = \Gamma_L / \Gamma_T$ and $R = \sigma_L / \sigma_T$ gives

$$\frac{d^2\sigma}{dQ^2 d\nu} = \Gamma_T \ (1+\varepsilon R) \ \sigma_T \ . \tag{7}$$

Parametrizations of Γ_T and ε from Ref. 48 are used to extract virtual photon cross sections from muon cross sections:

$$\Gamma_T = \frac{\alpha}{2\pi} \ \frac{(\nu^2+Q^2)^{\frac{1}{2}}}{Q^2 E^2 (1-\varepsilon)} \tag{8}$$

$$\varepsilon^{-1} = 1 + \frac{2(Q^2+\nu^2)\tan^2\theta/2}{Q^2} \ . \tag{9}$$

Here, E is the beam energy, M is the nucleon mass, and θ is the muon scattering angle in the laboratory. Figure 15(a) shows $Q^2\Gamma_T$ vs Q^2 for different values of ν; Fig. 15(b) illustrates the polarization ratio, ε. The flux Γ_T is normalized so that as Q^2 approaches zero, the effective cross section $\sigma_{eff}=(1+\varepsilon R)\sigma_T$ approaches the cross section for real photons of energy ν.


1. Q^2 dependence of the effective photon cross section

The effective photon cross section is obtained by factoring the equivalent flux of transversely polarized virtual photons out of the muon cross section. A measurement of R would require a substantial amount of data at a second beam energy and has not been made. There is no reason to expect σ_L/σ_T for charm production to equal σ_L/σ_T for deep inelastic scattering. In peripheral models like γGF and VMD, the photon does not couple to a valence quark in the target. Consequently, the kinematic effects which determine R for charm are different from those which influence R for inelastic scattering. Figure 15(c) shows R as predicted by γGF and Fig. 15(d) shows the product εR.

The Q^2 dependence of the effective photon cross section is shown in Fig. 16 and Table 4. The data are grouped into two ν bins, covering the regions 75 GeV < ν < 133 GeV with <ν> = 100 GeV and ν > 133 with <ν> = 178 GeV. In the figure, data points are shown with statistical errors. The solid lines are best fits to VMD propagators,
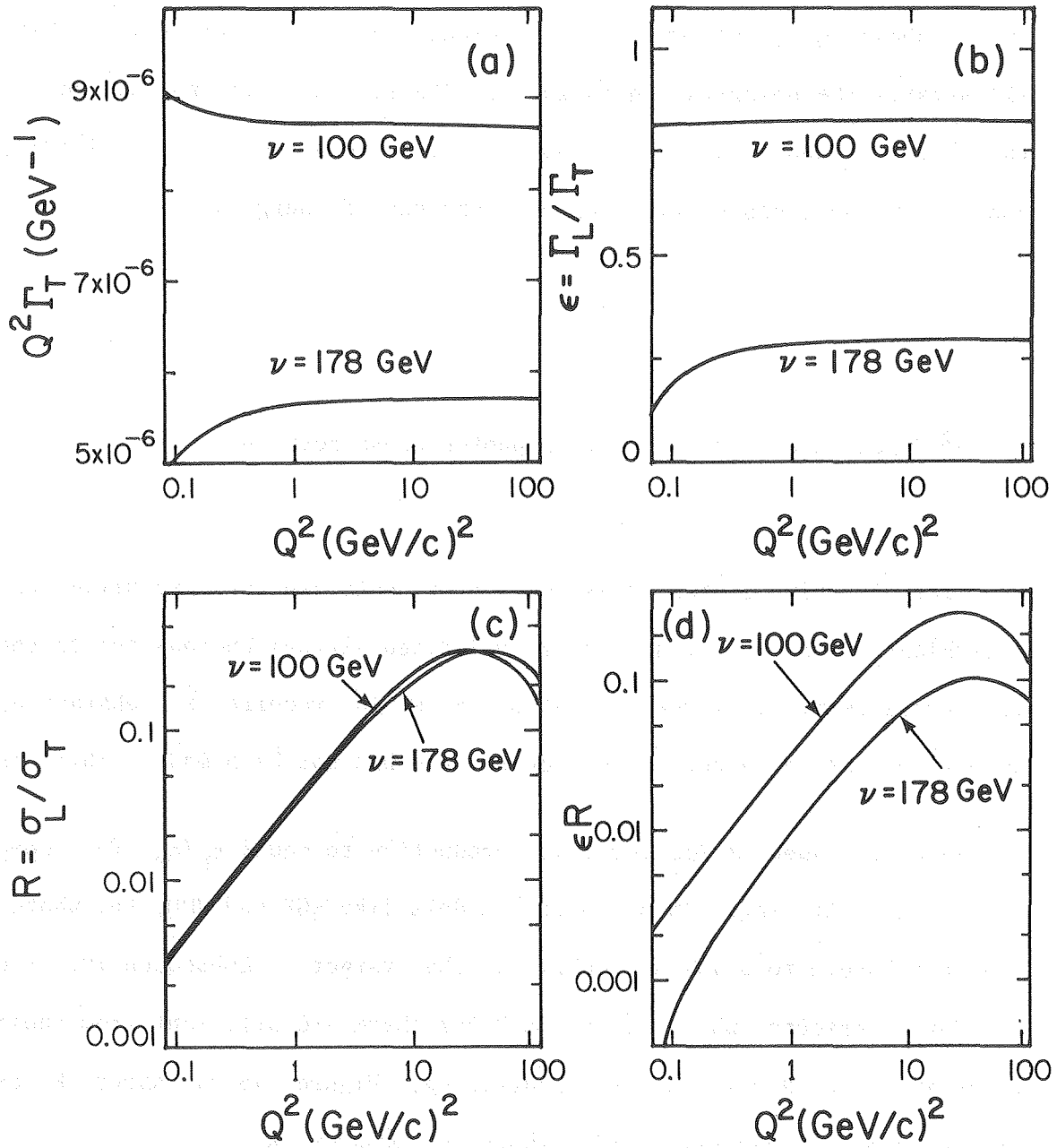
XBL 8010-2145

FIG. 15
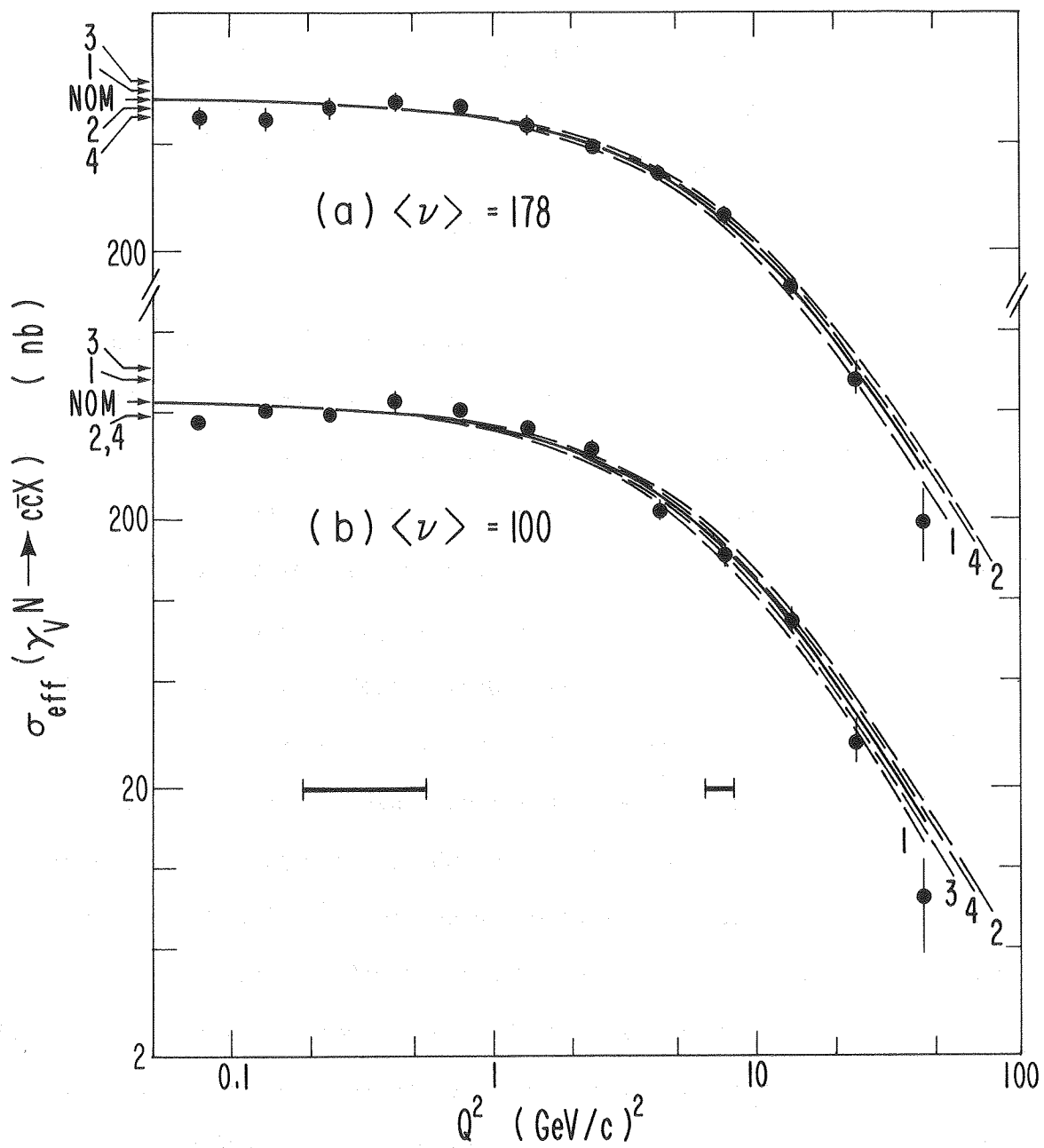
FIG. 16

XBL 803-384

$\sigma(Q^2) = \sigma(0)(1+Q^2/\Lambda^2)^{-2}$. The dashed curves, normalized to the nominal value of $\sigma(0)$, indicate the influence of the systematic effects discussed previously. Systematic errors are parametrized by (1) decreasing, (2) increasing by 50% the subtracted π, K-decay background and by recalculating the acceptance with the (3) softer, (4) harder fragmentation function described above. The mass parameter Λ is 3.3±0.2 GeV/c and 2.9±0.2 GeV/c for the 178 GeV and 100 GeV data, respectively. Extrapolated to $Q^2=0$, the data are best fit by $\sigma(0)$ of 750^{+180}_{-130} nb and 560^{+200}_{-120} nb for the 178 GeV and 100 GeV data. The rise of 190^{+34}_{-52} nb in the charm photoproduction cross section is significant; the difference of 0.39±0.18 GeV/c in Λ suggests some ν dependence in the Q^2 shape. The errors on Λ and $\sigma(0)$ are systematic, consequently the errors on the changes in Λ and $\sigma(0)$ are smaller. The effective cross section σ_{eff} decreases with decreasing Q^2 below $Q^2=.32$ (GeV/c)^2. Fits which do not include data in this region yield essentially the same results.

A wide-band photon-beam experiment has measured cross sections averaged from 50-200 GeV of 464±207 nb for $D^0\overline{D^0}$ pair production[49] and, later, 295±130 nb for inclusive D^0 production.[50] Using SPEAR data[20], one may crudely estimate the neutral D:charged D:F:Λ_c ratio to be 2:1:1:1 at $m_{c\bar{c}}$ ~4-5 GeV/c^2. The average of the two D^0 cross sections is 343±110 nb, corresponding to a total cross section for charm production of ~860 nb. This is consistent with our measurement. The authors of Refs. 49 and 50 determine experimental acceptance with a model which uses a fragmentation function $D(z)=\delta(z-1)$ and assumes no energy dependence above 50 GeV. The dashed curve in Fig. 14(c) shows that the muon data do not support these assumptions.

2. Contribution of charm to the rise in the
   photon-nucleon total cross section

Above ∿40 GeV, the photon-nucleon total cross section increases
with energy.[51,52] Most hadronic total cross sections begin to rise in
this energy region. The authors of Ref. 52 suggest that charm
production may contribute 2 to 6 μb of this increase in the energy range
from 20 GeV to 185 GeV. A fit to half the photon-deuteron cross section
from Ref. 51 is shown in Fig. 17. Since the threshold energy for charm
production is about 11 GeV, the charm cross section rises from zero at
low energy to the values reported here at ν=100 GeV and ν=178 GeV.
Diffractively produced charm is seen to make only a minor contribution
to the rise in the photon-nucleon total cross section.

3. ν dependence of the effective photon cross section

The ν dependence of the effective photon cross section in the range
0.32 $(GeV/c)^2 < Q^2 < 1.8$ $(GeV/c)^2$ is shown in Fig. 18 and Table 5. For
fixed ν, the cross section σ_{eff} varies by less than 20% in this range of
Q^2. Data in the figure are shown with statistical errors. Systematic
uncertainties, parametrized as described previously, are indicated by
the shaded band, referenced to the solid curve for visual clarity. To
gauge the systematic error associated with a given point, the shaded
region should be moved vertically until the position cut by the solid
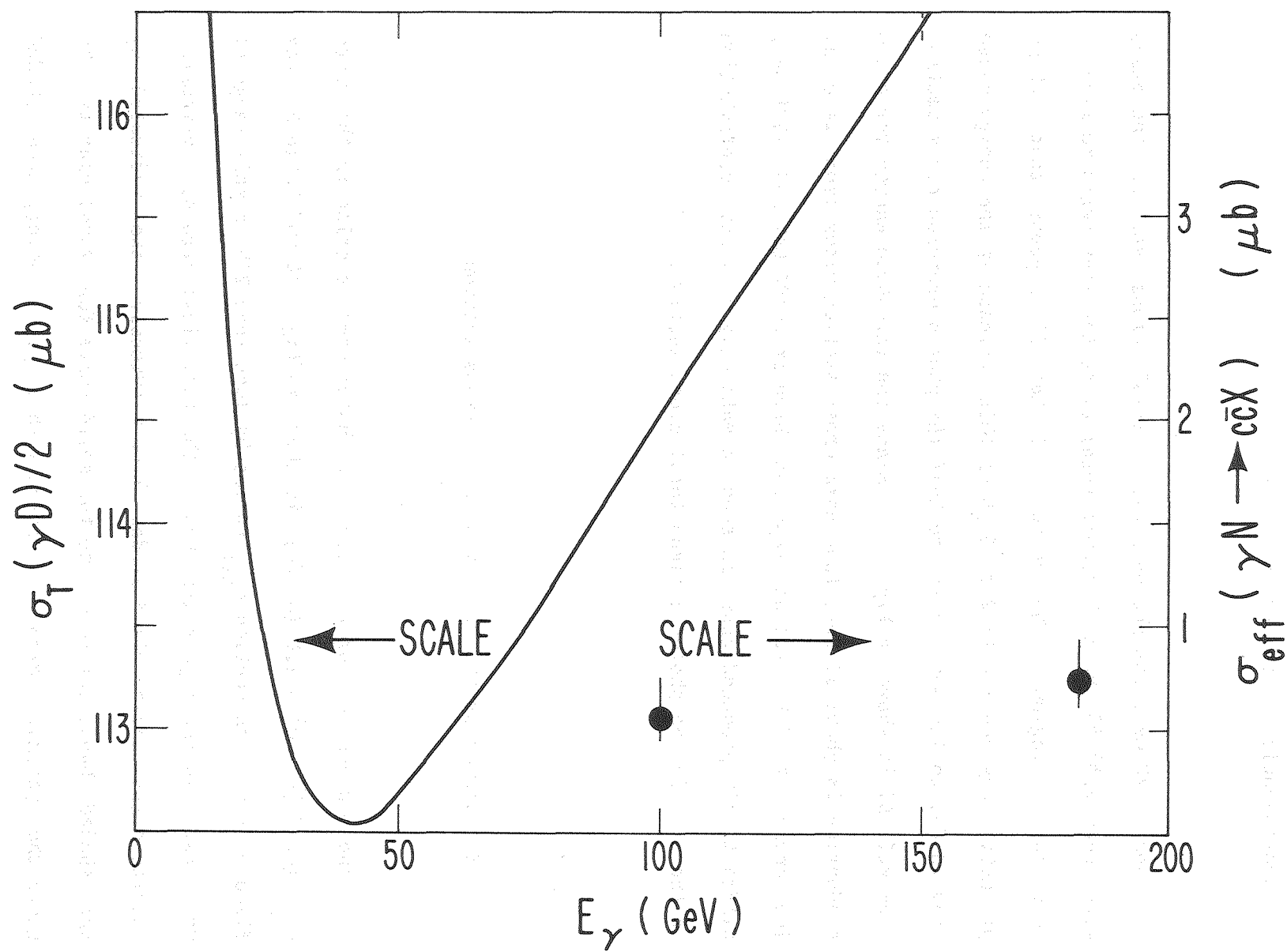
XBL 803-383

FIG. 17
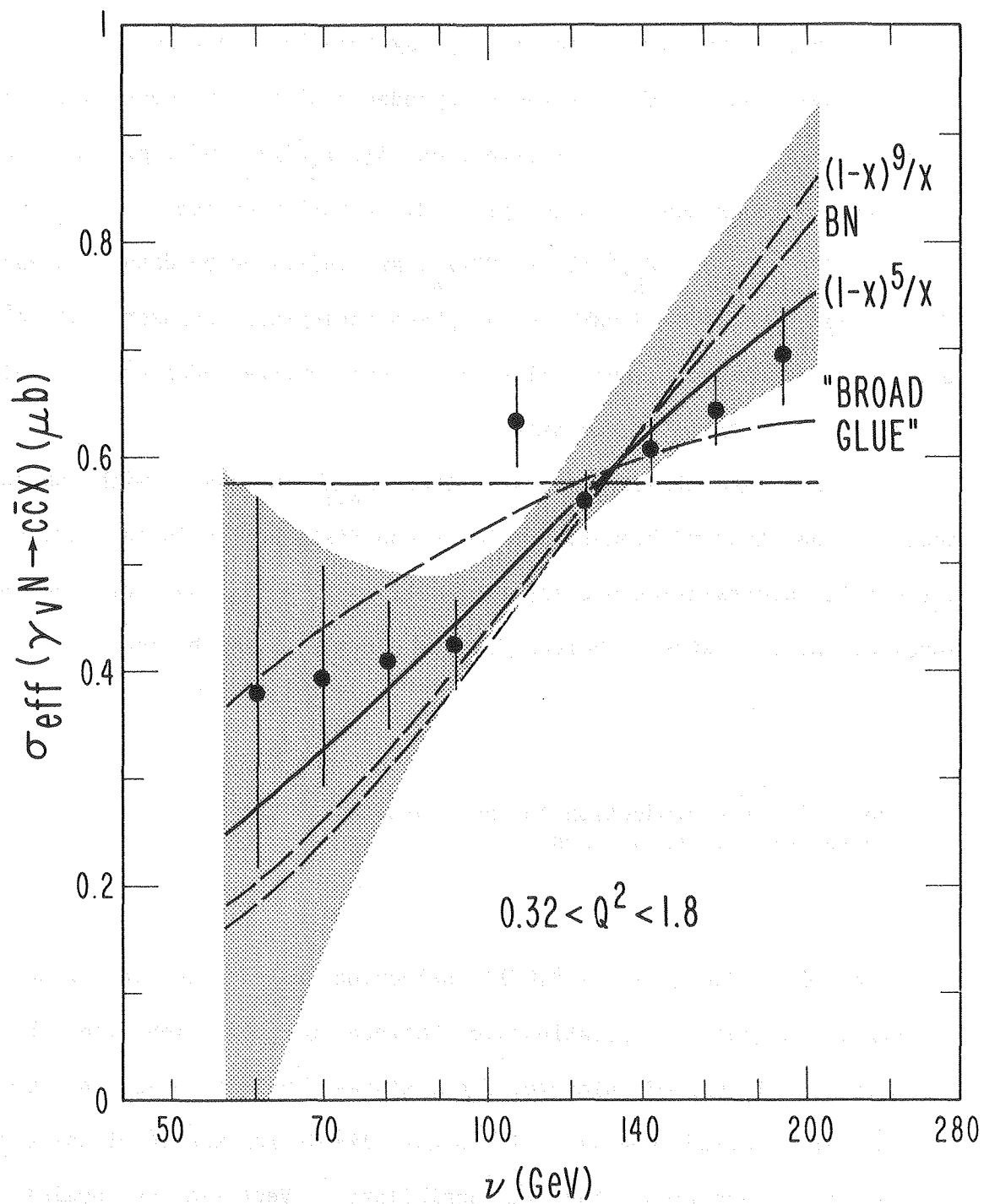
FIG. 18

line rests on the data point. Data with $\nu < 75$ GeV are excluded from further analysis because of their large systematic uncertainty.

The solid curve exhibits the ν dependence of the γGF model with the "counting-rule" gluon x_g distribution $3(1-x_g)^5/x_g$ and represents the data with 13% confidence. Other gluon distribution choices, $(1-x_g)^9/x_g$ and "broad glue"[9] $(1-x_g)^5(13.5+1.07/x_g)$ are indicated by dashed curves. The dashed curve labeled "BN" is a phenomenological parametrization[53] and the horizontal dashed line represents energy-independence. All curves are normalized to the data.

The muon data clearly indicate that σ_{eff} increases with photon energy. The standard "counting-rule" gluon distribution is favored, but systematic uncertainties prevent the analysis from ruling out the BN model or the two extreme choices for the gluon x_g distribution.

4. The ratio of ψ production to charm production and
    the ψN total cross section

The Okubo-Zweig-Iizuka[54](OZI) selection rules and vector-meson dominance suggest a relationship between ψ production and charm production.[55] In the OZI picture, final states from ψ-N collisions tend to contain charmed quarks. It is more likely for the $c\bar{c}$ of the ψ to survive the interaction than to annihilate. Vector-meson dominance describes ψ photoproduction as a two-step process. The incident photon changes into a ψ which then scatters from the target. The virtual ψ gains enough energy and momentum to materialize as a real particle. Together, OZI rules and VMD indicate that charm production should result

from inelastic ψN scattering. In this light, the ratio of charm production to ψ production should equal the ratio of the inelastic and elastic ψ-N scattering cross sections.

Sivers, Townsend, and West (STW) discuss the connection between charm production and inelastic ψN interactions.[55] They use VMD and the width for the decay $\psi \rightarrow e^+e^-$ to derive a relationship between $d\sigma/dt(\gamma N \rightarrow \psi N)$ and $d\sigma/dt(\psi N \rightarrow \psi N)$. The optical theorem and $-t$ dependence measured at SLAC then determine the ψN total cross section in terms of $d\sigma/dt(\psi N \rightarrow \psi N)$. STW equate the ψN total cross section with the $\psi N \rightarrow$ charm cross section and estimate the ratio of ψ photoproduction to charm photoproduction to be $(1.3\pm0.4)\times10^{-2}/\lambda$. The constant λ depends on the variation of the $\gamma\psi$ and the ψN couplings with Q^2; its value is about one-half. Our data on ψ production[15] and the results reported here fix the ratio of elastic ψ to diffractive charm production at 0.045 ± 0.022, somewhat larger than their prediction.

Sivers, Townsend, and West also calculate a lower limit for the ψN total cross section without assuming VMD.[55] They use unitarity and OZI rules to obtain the limit in terms of the ψ photoproduction cross section, the charm photoproduction cross section, particle masses, and the amount of OZI violation. With our data on ψ and charm production, their calculation yields the 90% confidence limit

$$\sigma_{total}(\psi N) > 0.9 \text{ mb.} \qquad (10)$$

D. The charm structure function

The muon-nucleon scattering cross section is

$$\frac{d^2\sigma}{dQ^2 d\nu} = \frac{4\pi\alpha^2}{\nu Q^4} \left[1 - y + \frac{y^2}{2(1+R(x,Q^2))} \right] F_2(x,Q^2). \qquad (11)$$

The variables x and y are $Q^2/(2M\nu)$ and ν/E where M is the nucleon mass and E is the beam energy. By measuring the structure functions F_2 and R, the small-scale structure of the nucleon can be probed. As before, R is σ_L/σ_T, the ratio of the cross sections for the target to absorb longitudinally and transversely polarized virtual photons with mass^2 $-Q^2$ and energy ν. Within the quark-parton model, the muon scatters elastically from a quark which carries momentum xP, where P is the nucleon momentum in a frame in which P is very large. The structure function $F_2(x,Q^2)$ is x times the probability to find a quark in the nucleon with this momentum. In this model, F_2 is scale-invariant and depends only on x, not on both x and Q^2. This is seen to be approximately true; $F_2(x,Q^2)$ with x held constant shows only weak Q^2 dependence.[12,56] In quantum chromodynamics (QCD), the quark-antiquark pairs in processes like $g \to q\bar{q} \to g$ should be revealed by the short-distance resolution of high-Q^2 scattering. Consequently, as Q^2 increases, the nucleon momentum should seem to be carried by more and more quarks and the average quark momentum should drop. The structure function F_2 will increase at small x and decrease at large x as Q^2 grows. This scale-noninvariance of F_2 has been experimentally observed.[12,56] F_2 increases with Q^2 for fixed x $\gtrsim$ 0.25 and decreases

with increasing Q^2 for fixed $x \leq 0.25$.

The description of scattering in terms of structure functions is equivalent to the description in terms of virtual photon fluxes and cross sections. The relationship between F_2, σ_T, and σ_L is[12]

$$F_2 = \frac{\nu(\nu - Q^2/2M)}{4\pi^2\alpha} \frac{Q^2}{Q^2 + \nu^2} (\sigma_T + \sigma_L).$$ (12)

A structure function may be defined for any process once its Q^2 and ν dependence are measured.

We define a charm structure function, $F_2(c\bar{c})$ as the analogue of the nucleon structure function F_2 through the expression

$$\frac{d^2\sigma(c\bar{c})}{dQ^2 d\nu} = \frac{4\pi\alpha^2}{\nu Q^4} \left[1 - y + \frac{y^2}{2} \right] F_2(c\bar{c}).$$ (13)

In this definition, $R(x,Q^2)$ is neglected. However, the comparison of $F_2(c\bar{c})$ with γGF model calculations takes the model's predictions for both σ_L and σ_T fully into account. Figure 19 and Table 6 show $F_2(c\bar{c})$ as a function of Q^2 for fixed ν at two values of average ν. Data are presented in the figure with statistical errors; the systematic uncertainty associated with each point is indicated by the shaded band. As in Fig. 18, the systematic error for a point may be determined by moving the shaded region to cover that point. Each curve, at each of the two average photon energies, is normalized to the data. The curves labeled $m_c = 1.5$ and $m_c = 1.2$ are γGF predictions with charmed quark masses of 1.5 GeV/c^2 and 1.2 GeV/c^2. Curves labeled ψDM are vector-meson dominance predictions using the ψ mass in the VMD propagator. The
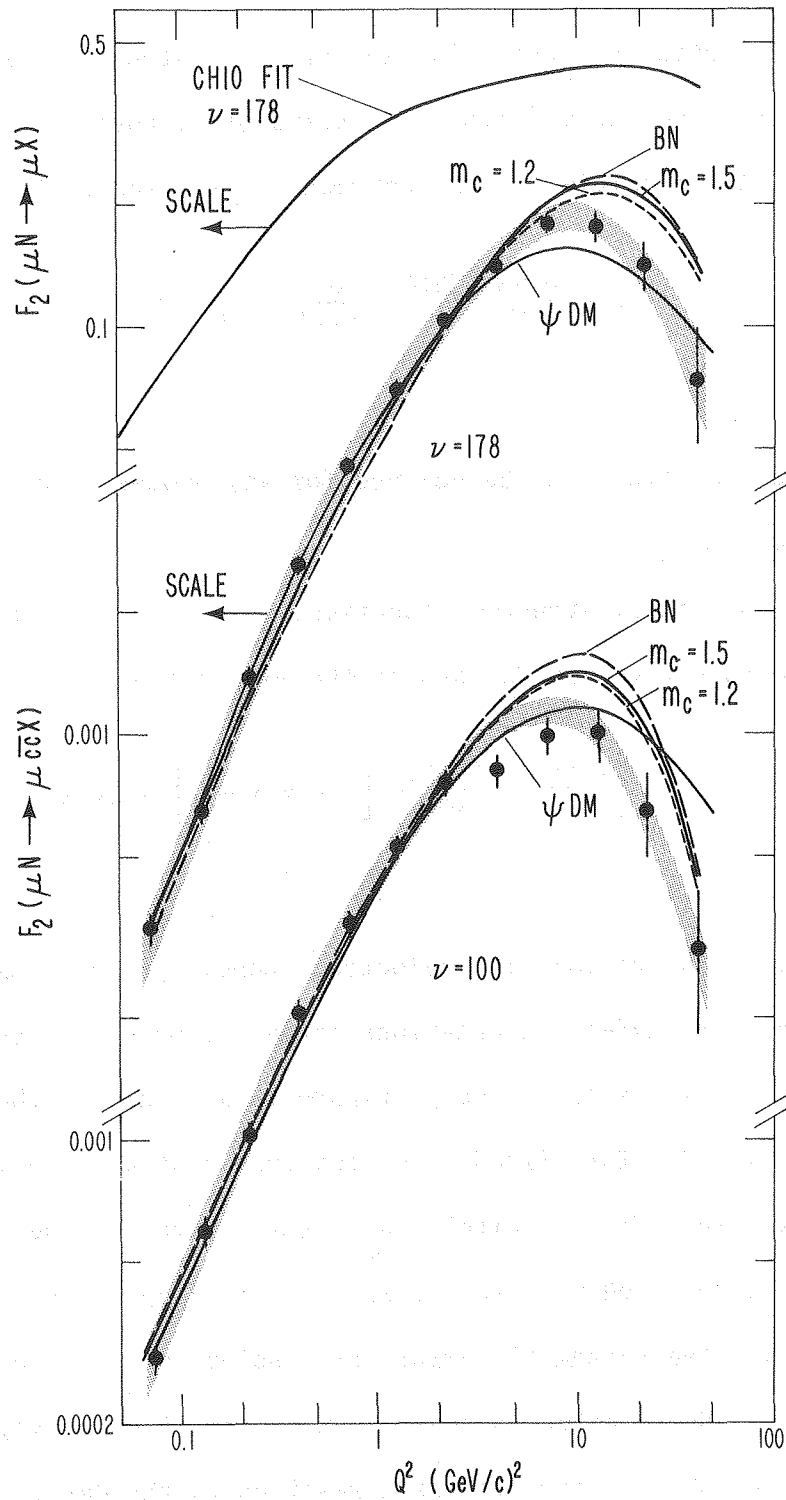
XBL 803-382

FIG. 19

curves labeled BN represent the model of Ref. 53. Shown at the top is a fit adapted from CHIO[12] to the inclusive structure function F_2 for isospin-0 muon-nucleon scattering. At its peak, $F_2(c\bar{c})$ is $\sim 4\%$ of F_2.

Since a $c\bar{c}$ state must have $m_{c\bar{c}} \gtrsim 2m_D$ to produce charmed particles, the parametrized quark mass m_c affects γGF's absolute normalization, not the shapes of its distributions. The maxima predicted by both the γGF and BN models resemble the data in shape and ν dependence, but occur at higher values of Q^2. The ψ-dominance functions drop too slowly at high Q^2. Systematic errors are only weakly correlated with Q^2 and do not obscure the disagreement. When α_s is redefined to be a function of $m_{c\bar{c}}^2 + Q^2$, instead of $m_{c\bar{c}}^2$, the agreement between data and γGF improves.[57]

$R(x,Q^2)$ is absorbed by $F_2(c\bar{c})$ in the definition of the structure function used in this analysis. Alternative assumptions about R could be made; the values of such a redefined F_2 would change typically by less than the reported systematic uncertainties.

E. The role of charm in scale-noninvariance

The relationship between $F_2(c\bar{c})$ and $\sigma_{eff}(c\bar{c})$ may be written as

$$F_2(c\bar{c}) \approx \frac{1-x}{4\pi^2\alpha} \left(\frac{Q^2}{1+Q^2/\nu^2} \right) \sigma_{eff}(c\bar{c}). \qquad (14)$$

Since most data reported here have $x \lesssim 0.1$, at fixed ν $F_2(c\bar{c})$ will grow with Q^2 until σ_{eff} begins to decrease, when $Q^2 \gtrsim m_\psi^2$. Because σ_{eff}

rises with energy, $F_2(c\bar{c})$ will also increase when Q^2 and ν are increased but x is held constant.

In the past, muon experiments measuring deep inelastic scattering have been unable to recognize charm production in their inclusive scattering data.[12,22,56] The detectors used by these experiments have been insensitive in the region traversed by the beam, which has severely limited their detection efficiency for charm states. As a result, typical measurements of inclusive F_2 and its scale-noninvariance have included all or part of the contribution from charm. Data from this experiment determine how much of the previously measured F_2 results from diffractive charm production, described by $F_2(c\bar{c})$.

Figure 20 shows the behavior of $F_2(c\bar{c})$ as a function of Q^2, with x held constant. Data points are arranged in pairs, alternately closed and open, and are connected by solid "bowtie-shaped" bands. The points in a pair represent data with the same value of x, but different Q^2. Data are shown with statistical errors. The systematic uncertainty in the slope of a line connecting the points in a pair is indicated by the solid band. Pairs are labeled by their values of Bjorken x. The dashed curves are the predictions of the γGF model, normalized to the data and damped at high Q^2 by the *ad hoc* factor $(1 + Q^2/ (100 \text{ GeV}^2/c^2))^{-2}$. The dot-dashed lines represent the slope in $F_2(c\bar{c})$ as Q^2 is increased but x is held constant which would be needed to account for all the scale-noninvariance in the CHIO fits to F_2. Their relative sizes are given by the percentages next to the lines.

The scale-noninvariance of $F_2(c\bar{c})$ is indicated by the non-zero slope in the line connecting the points in each pair. Diffractively-produced charm causes about one-third of the low-x
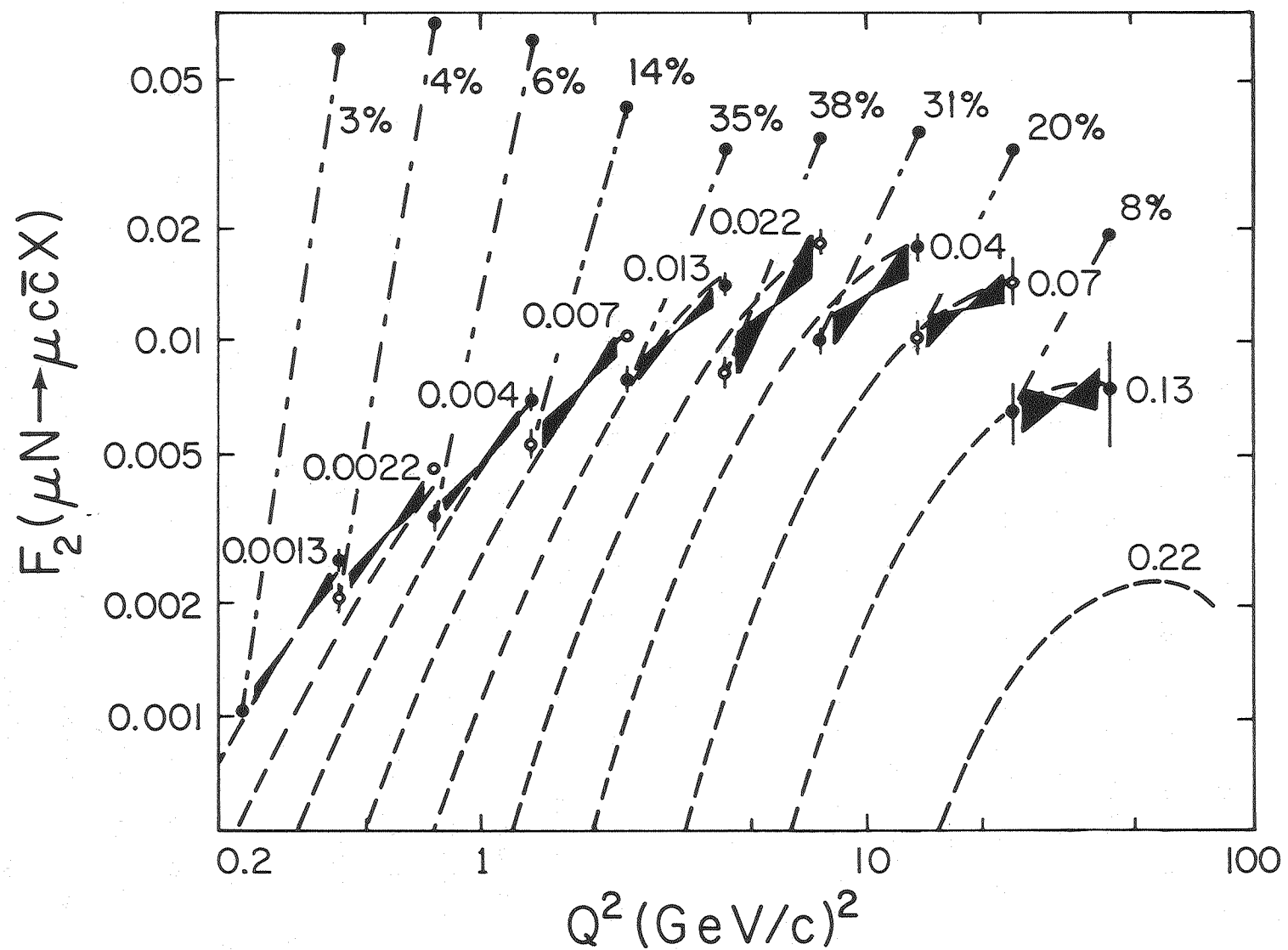
FIG. 20

XBL 8010-2147

scale-noninvariance measured by CHIO in the range $2 \ (\text{GeV/c})^2 < Q^2 < 10 \ (\text{GeV/c})^2$. This charm–induced scale breaking is a purely kinematic effect related to the heavy mass of charmed particles.

The production of bound charm states also contributes to the scale-noninvariance of F_2. The ψ muoproduction rate agrees[10,11,15] with the unmodified γGF prediction if elastic ψ production accounts for 1/6 of all charmonium production. To estimate the net effect of charm on F_2, the model's predictions for 2.8 nb of bound and 6.9 nb of open charm are combined to produce the results in Table 7. The numbers in the table are grouped in pairs. The top number in each pair is $10^4 d \ F_2(c\bar{c}) / d \ \ln(Q^2)$ at fixed x. $F_2(c\bar{c})$ is calculated as the sum of $F_2(c\bar{c})$ for $m_{c\bar{c}} < 2m_D$ as predicted by γGF and $F_2(c\bar{c})$ for open charm production as predicted by γGF but damped at high Q^2 and normalized to the data. This damped, renormalized $F_2(c\bar{c})$ matches the data in Fig. 20. The bottom number is $10^4 d \ F_2 / d \ \ln(Q^2)$ at fixed x for the fit to F_2 adapted from CHIO.[12] Charmonium production increases the scale-noninvariance of $F_2(c\bar{c})$ by $\lesssim 15\%$.

The results in Table 7 are calculated, not measured. Data from the muon experiment cover the Q^2-ν region of the two columns on the right side of the table. Where the charm scale-noninvariance is most important, the calculation is reliable to $\sim\pm40\%$. The γGF model predicts that charm accounts for about one-third of the inclusive scale-noninvariance in the region $2(\text{GeV/c})^2 < Q^2 < 13(\text{GeV/c})^2$ and $50 \ \text{GeV} < \nu < 200 \ \text{GeV}$, centered at $x \approx 0.025$. This region provided most of the original evidence[56] for scale-noninvariance in muon scattering.

The consequences of charm-induced scale breaking for QCD predictions of scale-noninvariance depend on the level of detail

sustained by the QCD calculation. Calculations which correctly describe the charmed sea in principle should be able to predict scale-breaking which properly includes the effects of charm production. Alternatively, $F_2(c\bar{c})$ may be subtracted from the experimentally measured structure function F_2 for comparison with QCD models which do not quantitatively describe the charmed sea at low Q^2.

The data indicate that the mechanism for charm production resembles γGF. The study of events with three final-state muons discussed earlier also suggests that γGF correctly describes these events. If this is true, charmed quarks tend to share equally the photon's energy. Results from another experiment confirm this tendency.[58]

F. Conclusions

Data from the Multimuon Spectrometer at Fermilab have provided a measurement of differential spectra for diffractive charm production by muons. The results are in general agreement with the virtual photon-gluon fusion model.[9] At large Q^2, the data show detailed disagreement both with that model and the predictions of Vector Meson Dominance. By redefining the strong coupling constant α_s, the agreement between data and γGF can be improved. Charm production contributes substantially to the scale-noninvariance at low Bjorken x which has been observed[12,56] in inclusive muon-nucleon scattering. The ratio of the rates for ψ and charm photoproduction is higher than predicted by a

calculation[55] which uses VMD and OZI rules. Without VMD, a calculation[55] and charm and ψ[15] production data set a lower limit on the ψN total cross section of 0.9 mb (90% confidence).

V. ACKNOWLEDGEMENTS

APPENDIX A

THE PHOTON-GLUON FUSION CROSS SECTION

In the photon-gluon fusion model, the cross section to produce a charmed quark and its antiquark with a virtual photon is

$$\sigma_T = 4\pi^2 \alpha W_1 / (\nu^2 + Q^2)^{\frac{1}{2}} \tag{A1}$$

for transversely polarized photons and

$$\sigma_L = 4\pi^2 \alpha W_2 (\nu^2 + Q^2)^{\frac{1}{2}} / Q^2 - \sigma_T. \tag{A2}$$

for longitudinally polarized photons.[14] Here,

$$W_1 = \frac{4}{9\pi M} \int_{x_o}^{1} dx\, \alpha_s \frac{G(x)}{x} \delta^2 \left\{ \left(\frac{m^4}{4} + m^2 m_c^2 - 2m^4 + \frac{Q^4}{4}\right) \ln\left(\frac{m^2 + \lambda}{m^2 - \lambda}\right) - \lambda\left(m_c^2 + \frac{1}{4}(m^2 - Q^2)^2 / m^2\right) \right\} \tag{A3}$$

and

$$W_2 = \frac{4M}{9\pi} \int_{x_o}^{1} dx\, \alpha_s G(x) x \delta \left\{ \lambda \left[9\delta - m^{-2} - 4(4m^2 + m_c^2)\delta^2 + 4m^2(2m^2 + m_c^2)\delta^3\right] \right.$$
$$\left. + \ln\left(\frac{m^2 + \lambda}{m^2 - \lambda}\right) \left[1 - (3m^2 + 8m_c^2)\delta + 4(m^4 + 5m^2 m_c^2 - 2m_c^4)\delta^2 - 2m^2(m^4 + 6m^2 m_c^2 - 4m_c^4)\delta^3\right] \right\} \tag{A4}$$

where

$$m^2 = 2M\nu x - Q^2 \tag{A5}$$

$$\lambda^2 = m^4 - 4m^2 m_c^2 \tag{A6}$$

$$\delta = (m^2 + Q^2)^{-1} \tag{A7}$$

$$x_o = (4m_D^2 + Q^2) / (2M\nu) \tag{A8}$$

$$\alpha_s = 12\pi / [(33 - 8)\ln(4m^2)] \tag{A9}$$

$$G(x) = 3(1-x)^5 / x \tag{A10}$$

APPENDIX B

SIMULATION OF HADRONIC SHOWERS

Once a vertex is selected, the simulation picks values for Q^2 and ν based on CHIO information. Values of Q^2 range from the minimum to the maximum kinematically allowed while ν runs from 10 GeV to the beam energy. The CHIO data are corrected to describe an isoscalar target[59] and renormalized by a factor of 0.9 to allow for nuclear screening.[16] The program calculates the cross section for scattering with $\nu \gtrsim 10$ Gev to fix the probability of generating showers.

CHIO data describe positive and negative hadron production by 147 GeV and 219 GeV muons. CHIO parametrize their results in terms of Feynman x (x_F) and hadron momentum perpendicular to the virtual photon (p_T). Feynman x is defined as

$$x_F = \frac{p_{\parallel}^*}{(p_{max}^{*2}-p_T^2)^{\frac{1}{2}}} \approx \frac{2p_{\parallel}^*}{s^{\frac{1}{2}}}. \tag{B1}$$

Here, $p_{\parallel}^*$ is the momentum of a hadron parallel to the virtual photon in the center-of-mass (CM) of the photon-nucleon system and p_{max}^* is the maximum momentum it can have in the CM. The total CM energy is $s^{\frac{1}{2}}$. The Monte Carlo uses CHIO distributions which are averaged over Q^2 $(Q^2 \gtrsim 0.3 \ (GeV/c)^2)$ and ν ($\nu > 53$ GeV) for muon-deuteron scattering. It is assumed that the x_F and p_T distributions provide an adequate description of the region with $Q^2 < 0.3 \ (GeV/c)^2$ and $\nu < 53$ GeV. It is also assumed that the distributions depend weakly on ν and Q^2.

Reference 22 presents K/π ratios for the CHIO 219 GeV data. Based

On these data, the simulation uses a K^+/π^+ ratio of $0.13 + 0.13p_T^2$ and a K^-/π^- ratio of $0.1 + 0.12p_T^2$. Here p_T is in GeV/c.

Neutral particles are treated in an approximate fashion by the Monte Carlo. Distributions for π^0 production are taken as an average of the π^+ and π^- distributions. A photon from π^0 decay produces muons and electrons in the ratio[42] $m_e^2/m_\mu^2 \approx 2.4 \times 10^{-5}$. Since a π^0 decays into two photons and each photon produces a pair of particles, the average yield of muons per π^0 is 9.6×10^{-5}, less than the decay probability for a charged meson. The simulation thus assumes that neutral pions just absorb energy from the shower and do not produce muons. Shower studies from another experiment indicate that this is a reasonable approximation.[60] Neutral kaons are made with the same distributions as their charged counterparts. Half the time a neutral K is used as an energy sink that does not yield muons and half the time the energy is returned to the pool available for charged meson production.

Charged and neutral mesons in the primary shower, the initial virtual photon-nucleon interaction, are generated with CHIO distributions in the range $0 < x_F < 1$. Approximate energy conservation is imposed by requiring $\sum x_F < 1$ where the sum runs over all particles generated. Primary showers violating this requirement are discarded and regenerated.

The Monte Carlo's description of primary showers neglects the dependence of kinematic distributions and charge multiplicities on atomic number, A. The muon spectrometer's acceptance is appreciable only for shower-induced muons whose parent mesons had $x_F > 0.2$. In this region, distributions and multiplicities show negligible A dependence.[61] The simulation also neglects muons arising from ρ, ω, ϕ production with

muonic decay of these particles.[60]

The program uses information stacks as bookkeeping aids while generating hadronic cascades. An "interaction" stack keeps track of all mesons with more than 5 GeV of energy which have not yet been made to interact in the detector to produce secondary showers. A "history" stack records the structure of the developing shower, storing information on parentage, p_T with respect to the parent meson, etc. for each meson generated with energy greater than 5 GeV. Pions and kaons in the primary shower are loaded into the interaction and history stacks. Secondary showers result from interactions of mesons with nucleons in the spectrometer which yield more particles. They are generated by removing a π or K from the bottom of the interaction stack, "colliding" it to produce more hadrons, and adding all new particles with sufficient energy to the bottom of the two stacks. The process is repeated until the interaction stack is empty, leaving the history stack with a complete description of the hadronic cascade.

The Monte Carlo generates an individual secondary shower in several steps. It first chooses the propagation distance that a π or K travels before interacting. Absorption lengths for mesons in iron are determined by scaling the proton absorption length at 20 GeV[62] by the ratio of the proton-deuteron and meson-deuteron total cross sections.[33-36] The $\pi^{\pm}$ absorption length is 26.8 cm or $(28.3 - 30/E)$ cm for particles with energy greater than or less than 20 GeV, respectively. The K^+ absorption length is 36.1 cm and the K^- absorption length is 30.1 cm, independent of energy. The distance a meson travels is a function of its absorption length and its initial position in a module. Particles produced near the back of a module have a greater

chance of reaching the gap between modules.

The shower generator decreases the meson's energy by the average amount it is expected to lose traveling through the spectrometer to its interaction point. The following inelastic collisions are simulated:

$$\pi^{\pm} N \rightarrow n_1 \pi^{\pm} + n_2 \pi^{\mp} + n_3 \pi^0 + X \tag{B2}$$

$$K^{\pm} N \rightarrow n_1 K^{\pm} + n_2 \pi^{\pm} + n_3 \pi^{\mp} + n_4 \pi^0 + X \quad . \tag{B3}$$

The coefficients n_1-n_4 are greater than or equal to zero. These interactions are completely described by specifying the particle multiplicity, x_F, and p_T distributions. Charged multiplicities are taken from the bubble chamber data of Refs. 25-28. Multiplicities are reduced by one unit to remove the target proton from the bubble chamber distributions. The data of Ref. 26 are then used to obtain the $x_F > 0$ multiplicities from the corrected $-1 < x_F < 1$ multiplicities of the cited references. These forward multiplicities provide an absolute normalization for the momentum distributions used to generate secondary hadrons. References 23, 24, 26, and 29 provide the Feynman x and p_T information which describes charged particle production. Neutral pions are produced with distributions corresponding to those for the pion with opposite charge from the parent particle.

Secondary mesons with $x_F \gtrsim 0$ are generated. As before, approximate energy conservation is imposed by requiring $\sum x_F < 1$. After successful creation of a secondary shower, all π's and K's with more than 5 GeV of energy are loaded into the two stacks.

The Monte Carlo neglects A dependence of secondary multiplicities and momentum distributions. The data of Ref. 37 indicate that the atomic number dependence is important in the target fragmentation

region, $x_F < 0$, and is negligible in the forward, positive x_F region.

The simulation does not model associated production in reactions such as $\pi N \rightarrow K\Lambda$.

The entire cascade is generated before the Monte Carlo chooses which particle will decay. If the probability of decay for a typical shower meson were large, this method would overpopulate the final generations of a shower. Early decays in the shower would deplete the hadron population available to produce more mesons in secondary cascades. Since the probability for a 120 GeV shower to produce a decay muon is about 10^{-3}, creating the full cascade while initially neglecting decays is a sufficiently accurate approximation. The Monte Carlo allows at most one meson to decay. A hadron with at least 5 GeV of energy is chosen based on a probability which is a function of absorption length, energy, and place of creation in the MMS. The probability that a particle will decay after traveling a given distance is proportional to the probability that it neither decayed nor interacted before getting that far. Since it is much more likely for a π or K to interact than to decay, the simulation chooses the length of the hadron's flight path according to the probability that it traveled that distance before interacting.

Pions decay to $\mu\nu$ with 100% probability and kaons to $\mu\nu$ with 63.5% probability. The 3.2% $K \rightarrow \mu\nu\pi$ decay mode is neglected. The laboratory frame energy of the neutrino is calculated to obtain the correct balance of shower energy, daughter energy, and missing energy. Once a decay meson is chosen, the shower generator returns program control to the Monte Carlo shell. The shell propagates through the detector all the

mesons in the parent-daughter chain which terminates in a decay, calculates the Lorentz transformations needed to produce the resulting muon, and propagates the muon through the rest of the detector.

Figures 13 and 21-25 show predictions of the shower Monte Carlo. The charged multiplicity for mesons with more than 5 GeV of energy is shown in Fig. 13(a). The number of meson generations linking the virtual photon-nucleon interaction and the decay muon is shown in Fig. 21(a). Though 22% of the muons come from parent particles created in meson-nucleon showers, after reconstruction and cuts this decreases to 10%. Figure 21(b) shows the decay probability for generated shower mesons. The two peaks correspond to π's and K's. The ratio of K's to π's decaying in flight is 0.69 for K^+/π^+ and 0.46 for K^-/π^-. The ratio of π^+ to π^- is 0.92. This unusual charge ratio accurately reflects the production ratio of 0.91 measured by CHIO. After reconstruction and analysis cuts, the ratios are 0.81 for K^+/π^+, 0.59 for K^-/π^-, and 0.81 for π^+/π^-. The increase in K/π fractions presumably results from the difference in acceptance caused by the greater available p_T in K decay. The change in the π^+/π^- ratio is caused by the larger acceptance for daughter muons charged opposite to the beam since most data were taken with positive beam muons. Figure 22 shows ν and Q^2 for simulated inelastic muon-scattering events. Figure 23 shows the x_F and p_T^2 distributions for shower mesons. The aproximate energy conservation requirement imposed on secondary interactions rejects 14% of the generated secondary showers. Figure 24(a) shows the energy of hadrons allowed to decay and Fig. 24(b) shows the decay muon momenta along the z axis. The muon and neutrino energies for events satisfying the simulated dimuon trigger are shown in Fig. 25(a). Figure 25(b)
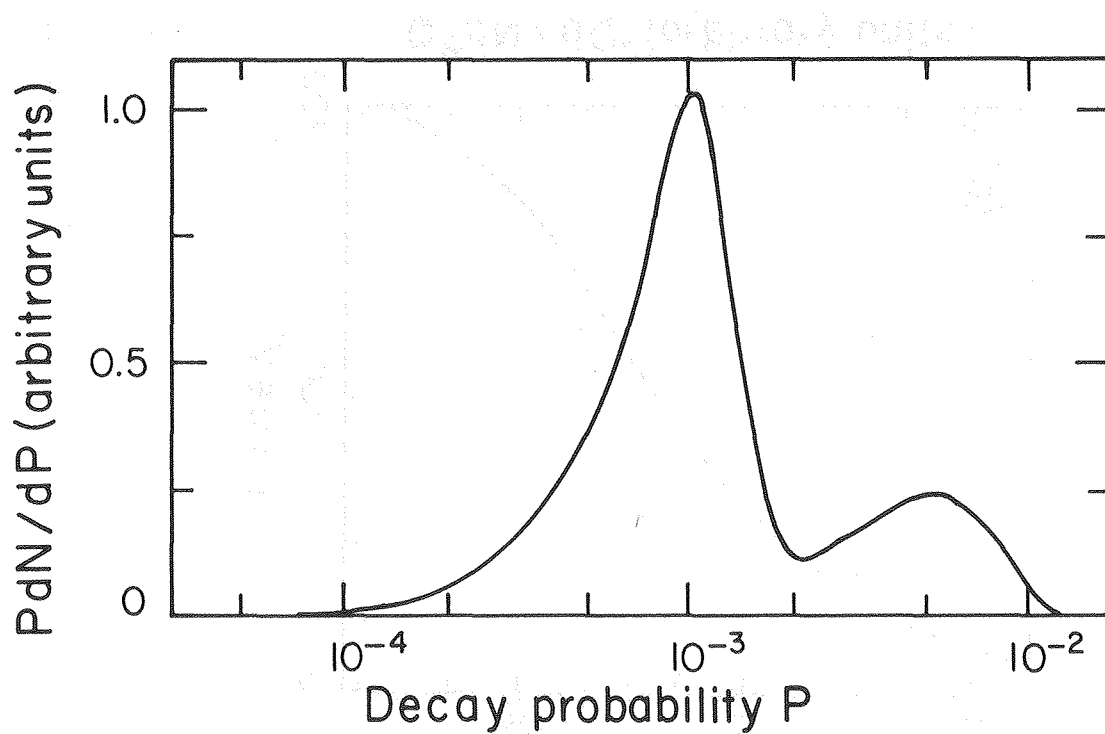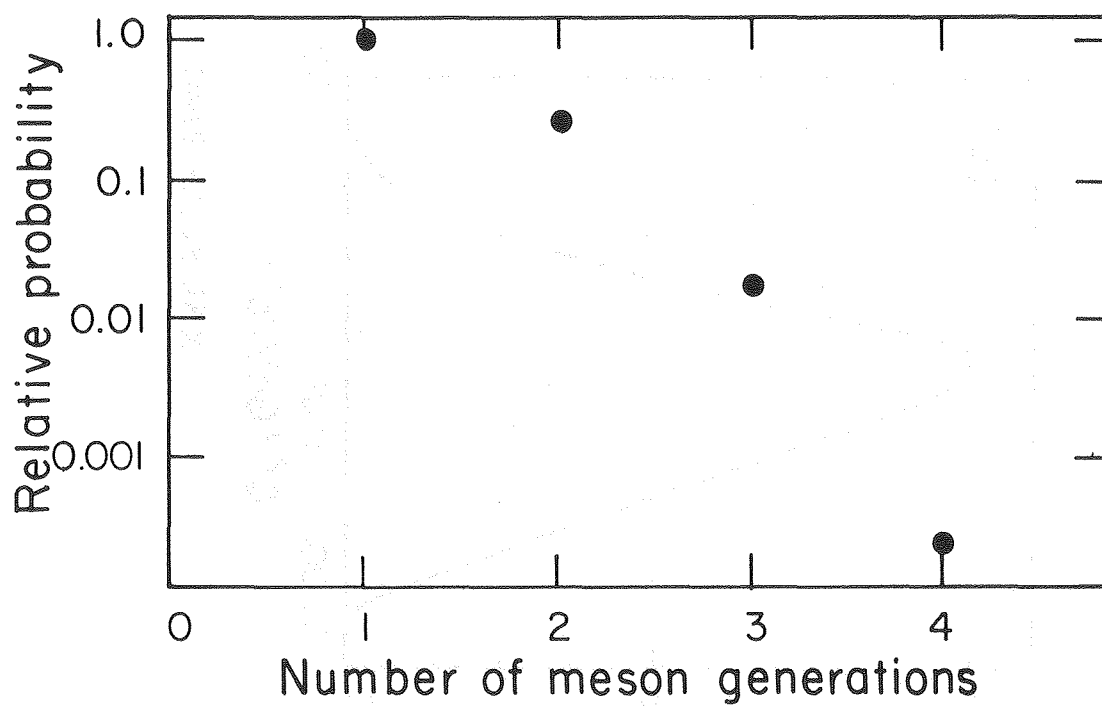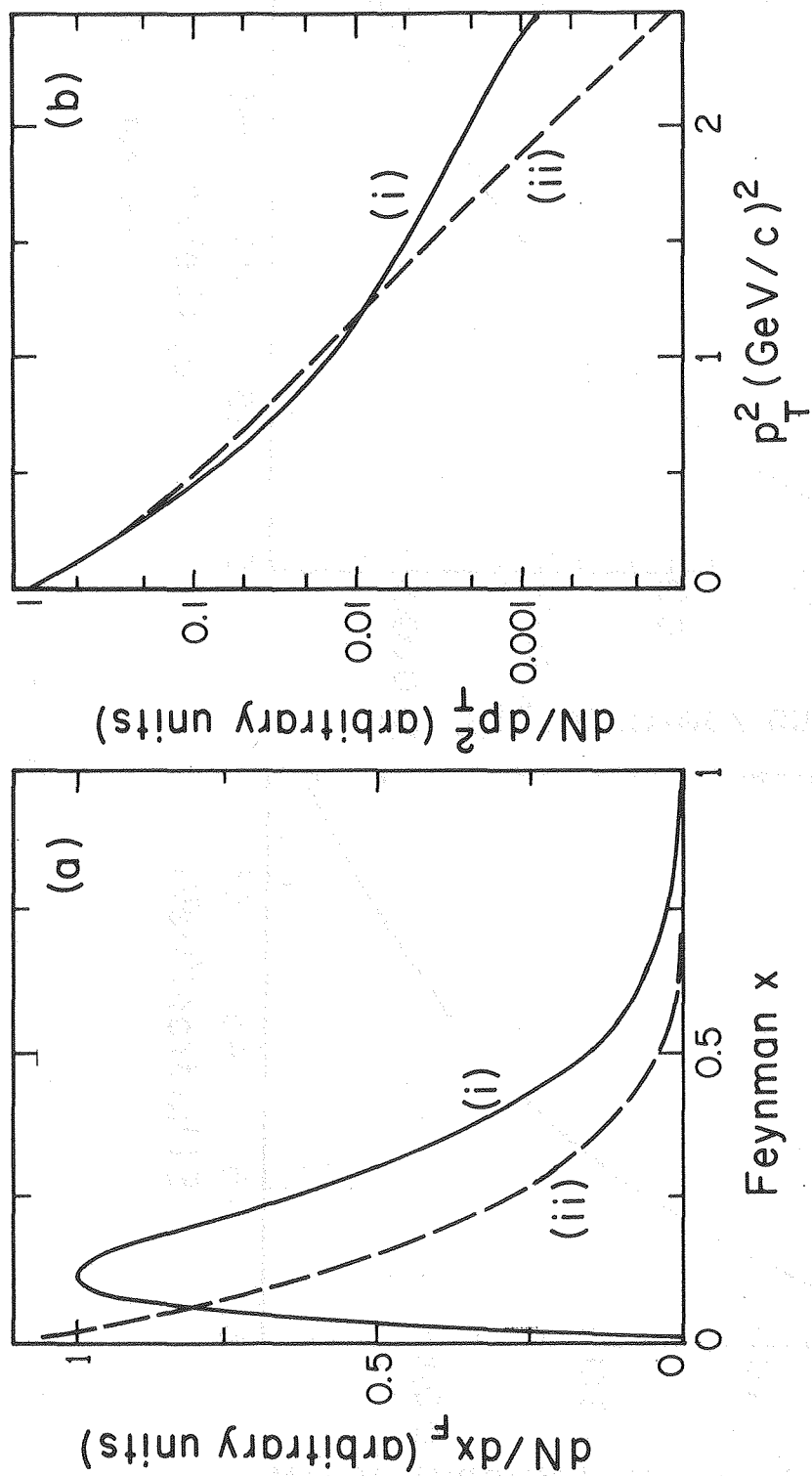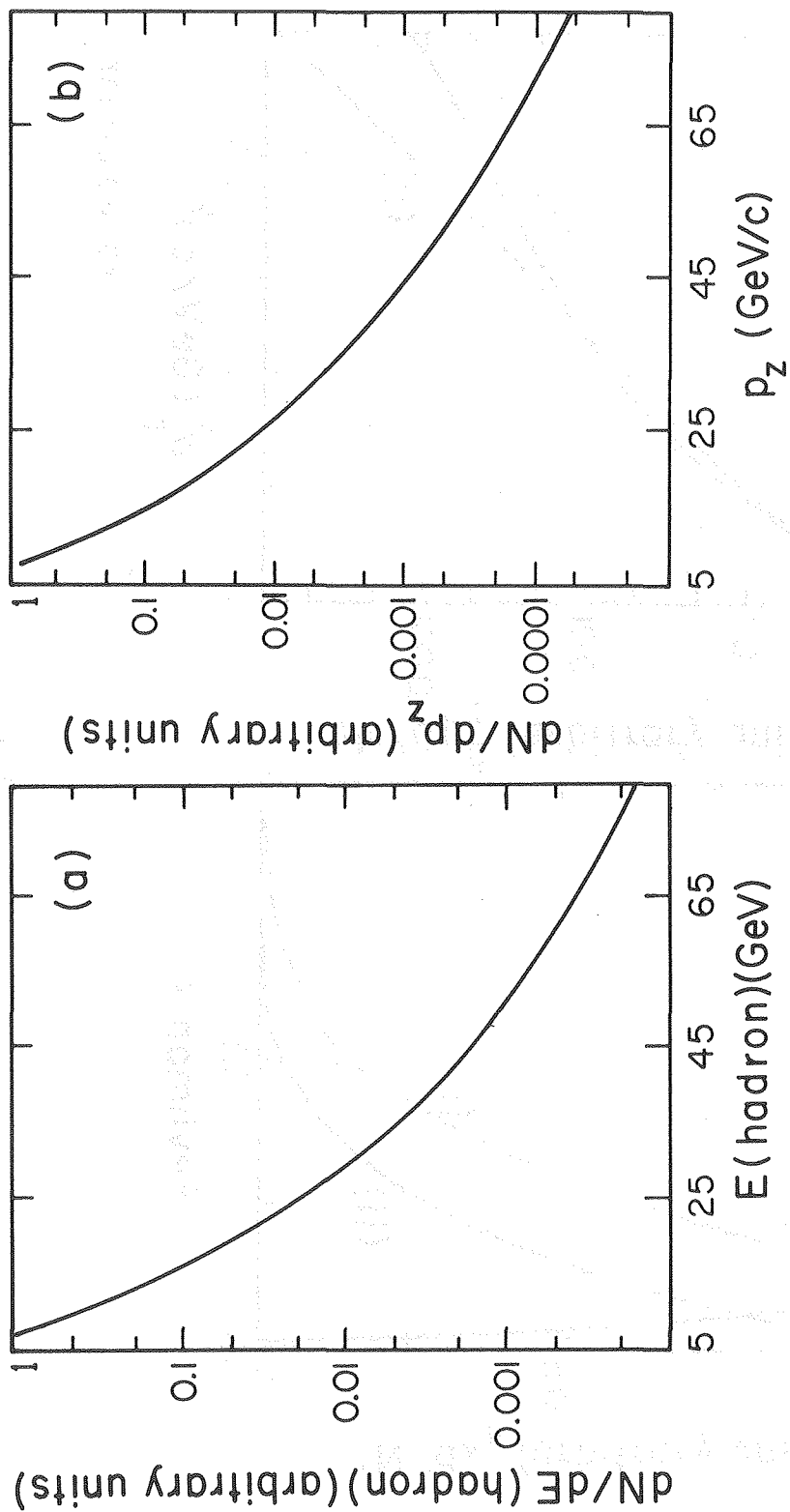
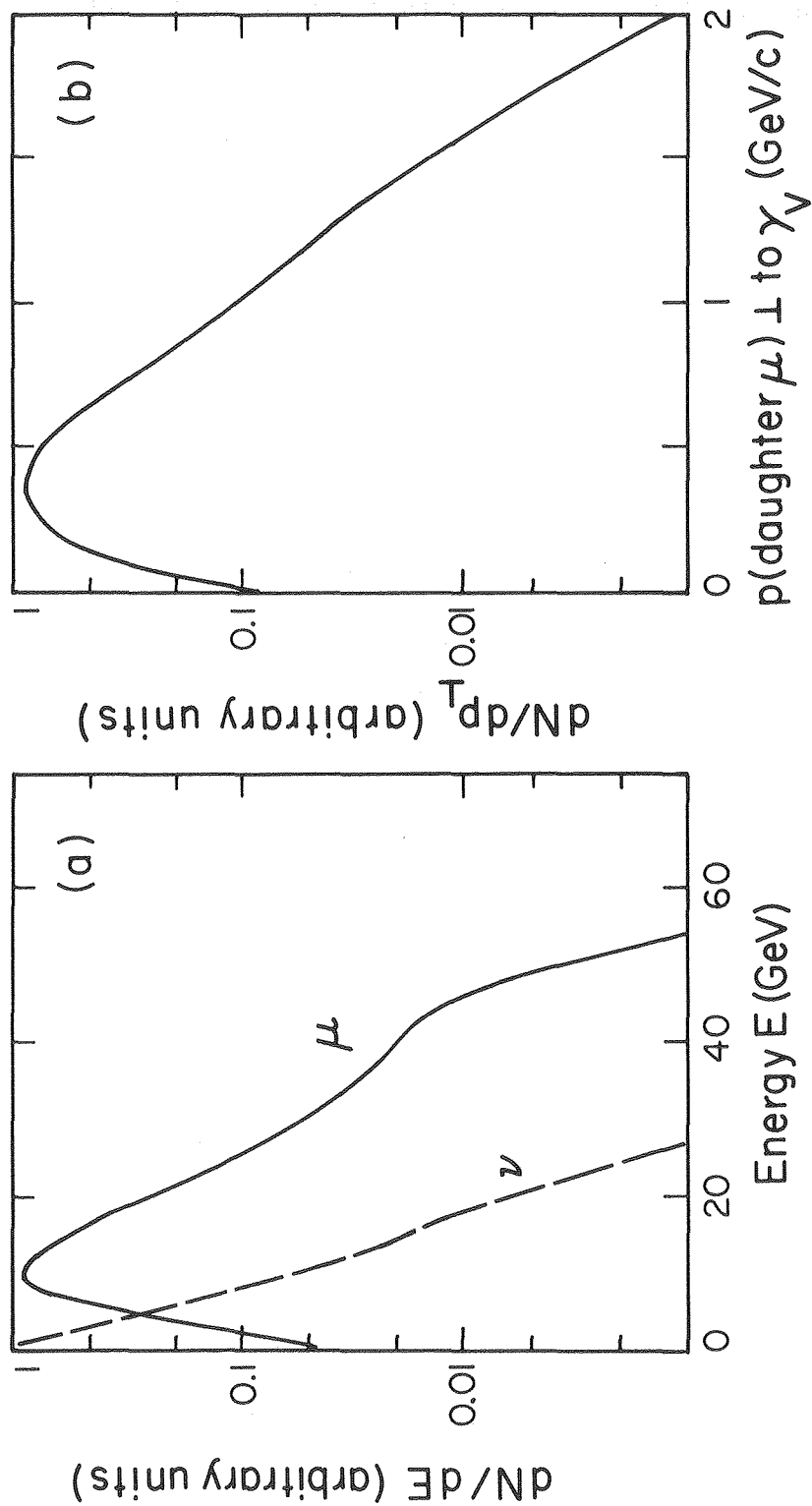XBL 8010-2143

FIG. 21
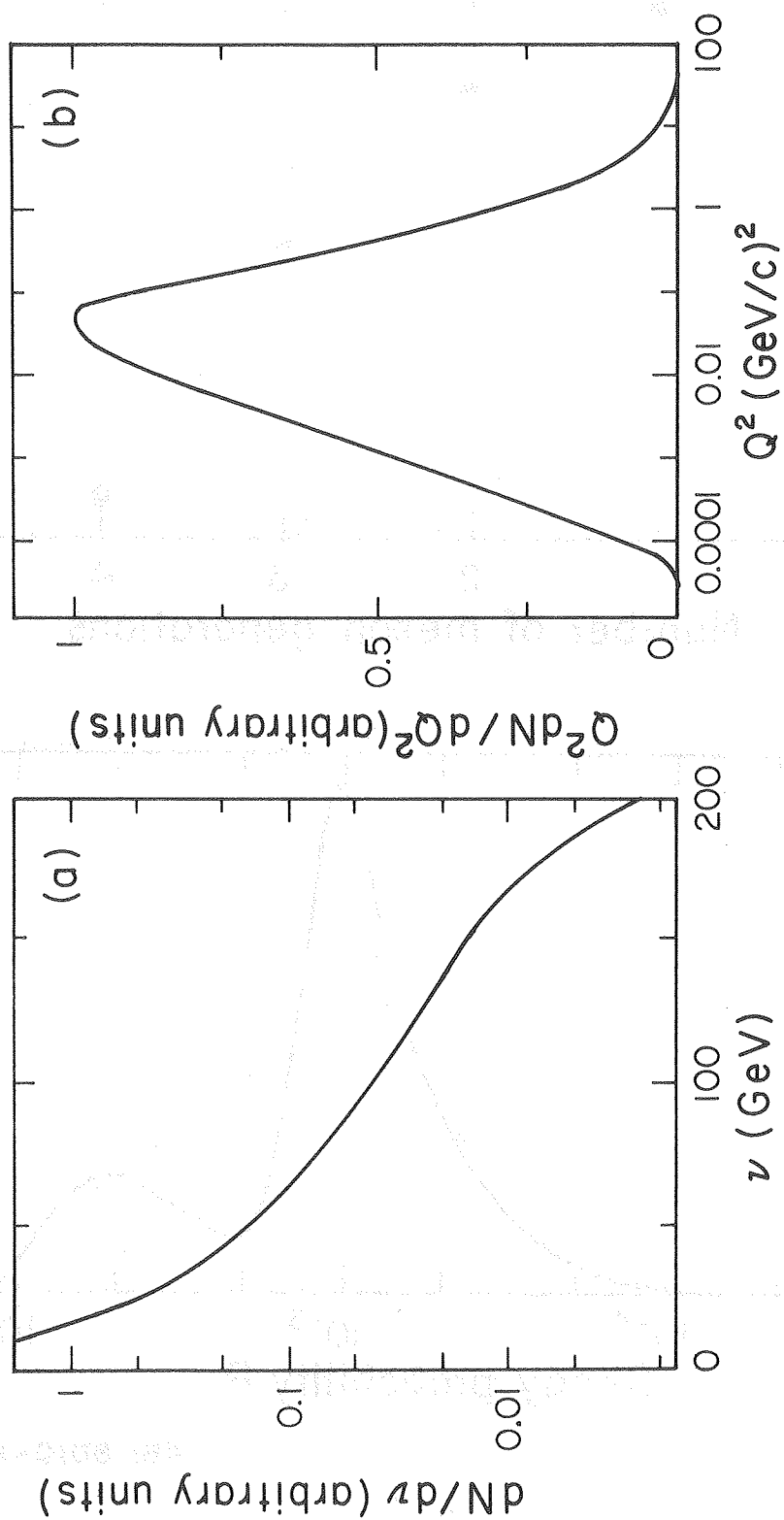
FIG. 22

XBL 8010-2148

XBL8010-2135

FIG. 23

FIG. 24

XBL8010-2142
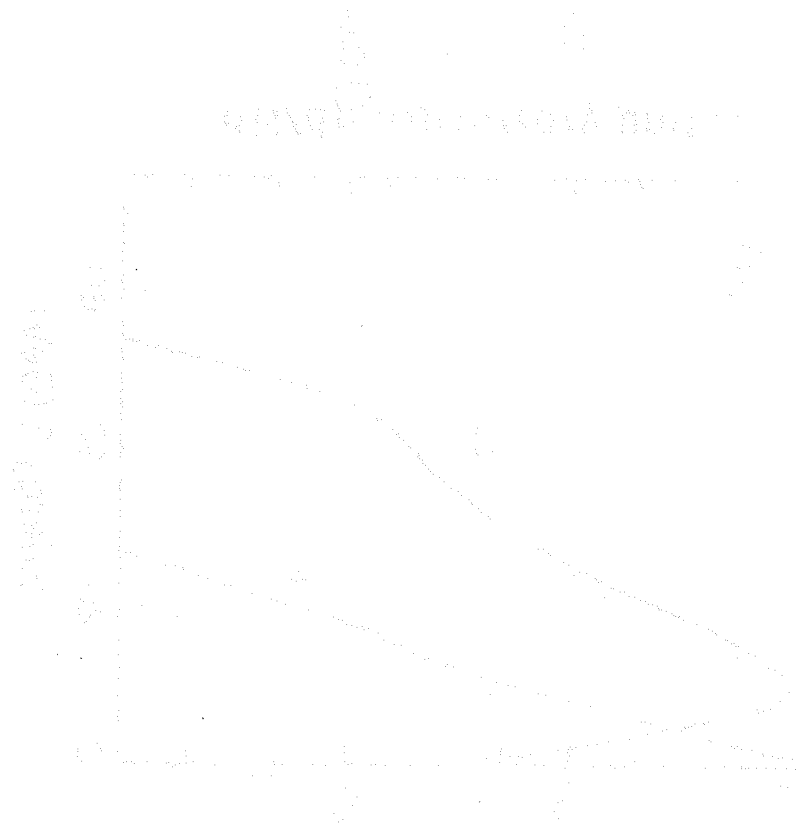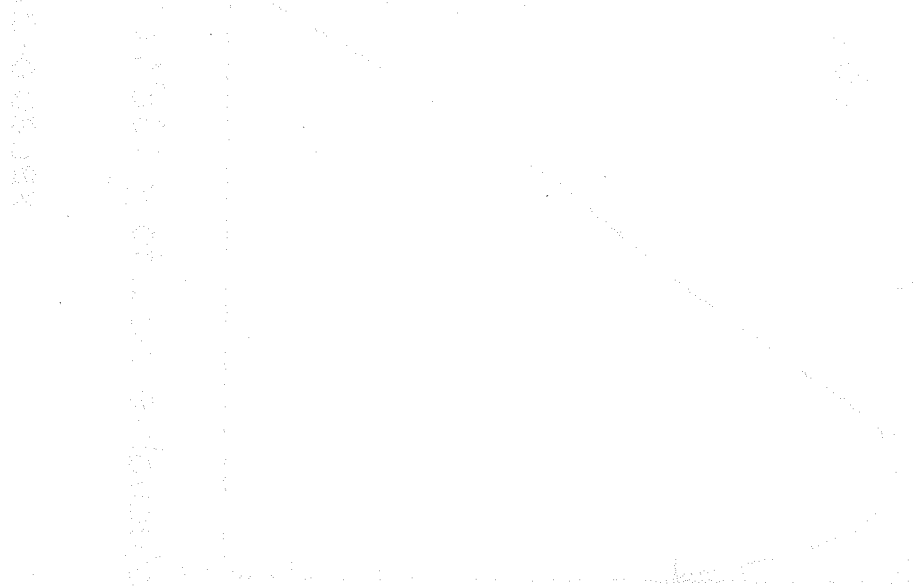
XBL 8010-2146

FIG. 25

illustrates the momentum component perpendicular to the virtual photon

for the muon at the decay point in events satisfying a trigger.

REFERENCES

*Based on G.D. Gollin, Ph.D. Thesis, Princeton University, 1980 (unpublished).

[a] Now at Enrico Fermi Institute, Chicago, IL 60637.

[b] Now at Bell Laboratories, Murray Hill, NJ 07974.

1. B. J. Bjorken and S. L. Glashow, Phys. Lett. 11, 255 (1964).

2. S. L. Glashow, J. Iliopoulos, and L. Maiani, Phys. Rev. D2, 1285 (1970).

3. M. Gell-Mann, Phys. Lett. 8, 214 (1964).

4. J. J. Aubert et al., Phys. Rev. Lett. 33, 1404 (1974); J.-E. Augustin et al., Phys. Rev. Lett. 33, 1406 (1974).

5. G. Goldhaber et al., Phys. Rev. Lett. 37, 255 (1976); I. Peruzzi et al., Phys. Rev. Lett. 37, 569 (1976).

6. G. J. Feldman et al., Phys. Rev. Lett. 38, 1313 (1977); R. Brandelik et al., Phys. Rev. Lett. 33, 1406 (1974).

7. See, for example, J. Kirkby in Proceedings of the 1979 International Symposium on Lepton and Photon Interactions at High Energies, edited by T.B.W. Kirk and H.D.I. Arbarbanel (Fermilab, Batavia, Illinois, 1979), p.107-121.

8. J. P. Leveille, University of Wisconsin Report No. COO-881-120, 1979 (unpublished).

9. See, for example, J. P. Leveille and T. Weiler, Nucl. Phys. B147, 147 (1979), and references cited therin.

10. A.R. Clark et al., Phys. Rev. Lett. 45, 682 (1980).

11. A. R. Clark et al., Phys. Rev. Lett. 45, 1465 (1980).

12. B.A. Gordon et al., Phys. Rev. D20, 2645 (1979).

13. G. Gollin et al., IEEE Trans. Nuc. Sci. NS-26, 59 (1979).

14. V. Barger, W.Y. Keung, and R. J. N. Phillips, Phys. Lett. 91B, 253, (1980).

15. A.R. Clark et al., Phys. Rev. Lett. 43, 187 (1979).

16. W.R. Ditzler et al., Phys. Lett. 57B, 201 (1975).

17. See, for example, A. Silverman, in <u>Proceedings of the International Symposium on Electron and Photon Interactions at High Energies Liverpool, England, September, 1969</u>, edited by D. W. Barben and R. E. Rand (Daresbury, Warrington, Lancashire, England, 1970), Table 2.

18. P. A. Rapidis <u>et al</u>., Phys. Lett. <u>84B</u>, 507 (1979).

19. The decay matrix elements of I. Hinchcliffe and C. H. Llewellyn Smith, Nucl. Phys. <u>B114</u>, 45 (1976) are used to describe D decay.

20. J. Kirkby in <u>Proceedings of the 1979 International Symposium on Lepton and Photon Interactions at High Energies</u>, edited by T.B.W. Kirk and H.D.I. Arbarbanel (Fermilab, Batavia, Illinois, 1979), p.107-121; M. Coles, private communication. Our experiment measures the product of the cross section and the average yield of muons.

21. W.A. Loomis <u>et al</u>., Phys. Rev. <u>D19</u>, 2543 (1979).

22. J. Proudfoot, Ph.D. Thesis, University of Oxford, 1978 (unpublished).

23. P. Bosetti <u>et al</u>., Nucl. Phys. <u>B54</u>, 141 (1973).

24. P. Bosetti <u>et al</u>., Nucl. Phys. <u>B60</u>, 307 (1973).

25. G.A. Akopdjanov <u>et al</u>., Nucl. Phys. <u>B75</u>, 401 (1974).

26. W. Morris <u>et al</u>., Phys. Lett. <u>56B</u>, 395 (1975).

27. E.L. Berger <u>et al</u>., Nucl. Phys. <u>B77</u>, 365 (1974).

28. V.V. Ammosov <u>et al</u>., Nucl. Phys. <u>B58</u>, 77 (1973).

29. S.L. Stone <u>et al</u>., Nucl. Phys. <u>B32</u>, 19 (1971).

30. R. Barloutaud <u>et al</u>., Yad. Fiz. <u>24</u>, 580 (1976) (Sov. J. Nucl. Phys. <u>24</u>, 303 (1976)).

31. A. Bialas in <u>Proceedings of the First Workshop on Ultrarelativistic Nuclear Collisions</u>, Lawrence Berkeley Laboratory Report.No. LBL-8957, edited by C. Webb (Lawrence Berkeley Laboratory, Berkeley, California 1979),p. 63-114.

32. A. Bialas and E. Bialas, Phys. Rev. <u>D21</u>, 675 (1980).

33. S.P. Denisov <u>et al</u>., Phys. Lett. <u>36B</u>, 415 (1971).

34. S.P. Denisov <u>et al</u>., Nucl. Phys. <u>B65</u>, 1 (1973).

35. A.S. Carroll <u>et al</u>., Phys. Rev. Lett. <u>33</u>, 932 (1974).

36. W. Galbraith et al., Phys. Rev. 138, 913 (1965).

37. J.E. Elias et al., Fermilab Report No. FERMILAB-Pub- 79/47-EXP 7185.178, 1979 (unpublished).

38. J.A. Gaidos et al., Nucl. Phys. B32, 10 (1971).

39. See, for example, J.F. Martin et al., Phys. Rev. D20, 5 (1979). This experiment used 20.5 GeV electrons at SLAC.

40. M. Shaevitz, private communication.

41. See, for example, R.D. Field and R.P. Feynman, Phys. Rev. D15, 2590 (1977).

42. D.H. Perkins, Introduction to High Energy Physics, Addison-Wesley, Reading, Massachusetts, 1972, p. 40.

43. V. Barger, W.Y. Keung, and R.J.N. Phillips, Phys. Rev. D20, 630 (1979).

44. A.R. Clark et al., Phys. Rev. Lett. 45, 686 (1980).

45. D. Bauer et al., Phys. Rev. Lett. 43, 1551 (1979).

46. The MSF model is similar to that of F. Bletzacker, H.T. Nieh, and A. Soni, Phys. Rev. Lett. 37, 1316 (1976).

47. C. Chang et al., Phys. Rev. Lett. 39, 519 (1977).

48. F.J. Gilman, Phys. Rev. 167, 1365 (1968). The more familiar form for Γ_T is from L.N. Hand, Phys. Rev. 129, 1834 (1963); Hand's flux is $(1-Q^2/(2M\nu)) / (1+Q^2/\nu^2)^{\frac{1}{2}}$ times Gilman's. Values of $Q^2/(2M\nu)$ range from about .001 to .1 in the data presented here.

49. M.S. Atiya et al., Phys. Rev. Lett. 43, 414 (1979).

50. P. Avery et al., Phys. Rev. Lett. 44, 1309 (1980).

51. D.O. Caldwell et al., Phys. Rev. Lett. 42, 533 (1979).

52. D.O. Caldwell et al., Phys. Rev. Lett. 40, 1222 (1978).

53. F. Bletzacker and H.T. Nieh, SUNY-Stony Brook Report No. ITP-SB-77-44, 1977 (unpublished).

54. S. Okubo, Phys. Lett. 5, 160 (1963); G. Zweig, CERN Report 8419/Th 412, 1964 (unpublished); J. Iizuka, Prog. Theor. Phys. Suppl. 37-38, 21 (1966).

55. D. Sivers, J. Townsend, and G. West, Phys. Rev. D3, 1234 (1976).

56. Y. Watanabe _et al._, Phys. Rev. Lett. 35, 898 (1975); C. Chang _et al._, Phys. Rev. Lett. 35, 901 (1975).

57. T. Weiler, "Photon-Gluon Fusion and Diffractive and Non-diffractive ψ-Leptoproduction," presented at XX International Conference on High Energy Physics, Madison, Wisconsin, July 17-23, 1980.

58. J. J. Aubert _et al._, Phys. Lett. 94B, 101 (1980).

59. S.C. Loken, private communication. The correction is a hand fit to SLAC data comparing electron-neutron and electron-proton scattering.

60. M. Shaevitz, private communication. Prompt muons from hadronic showers contribute less than 10% of the total muon yield.

61. W.A. Loomis, private communication.

62. R.L. Kelly _et al._, Rev. Mod. Phys. 52, No. 2, Part II, S50 (1980).

TABLE 1

Calorimeter and hodoscope subtrigger combinations resulting in a full dimuon trigger. Cluster 1 includes calorimeter counters in modules 1 and 2, cluster 2 includes modules 2 and 3, etc. as described in the text. Hodoscope group 1 includes trigger banks 1, 2, and 3, placed after modules 4, 6, and 8, group 2 includes trigger banks 2, 3, and 4 after modules 6, 8, 10, etc.

Calorimeter cluster with subtrigger	Required hodoscope groups with subtrigger
1 (and any others downstream)	any of 1-6
2 (and any others downstream)	any of 2-6
3 (and any others downstream)	any of 3-6
4 (and any others downstream)	any of 4-6
5 (and 6 if present)	5 or 6
6	6

TABLE 2

Mean values of six reconstructed kinematic quantities for data before background subtraction, for charm Monte Carlo, and for π, K-decay Monte Carlo. All events have E(daughter μ) $\geq$ 15 GeV, ν > 75 GeV, and satisfy the standard analysis cuts described in section III. Statistical errors are shown.

Reconstructed kinematic quantity	Data	Monte Carlo Charm	π, K
$<\nu>$ (GeV)	132.2 ±0.2	136.1 ±0.3	120.4 ±1.0
Geometric mean Q^2 $(GeV/c)^2$	0.547 ±0.004	0.729 ±0.006	0.260 ±0.011
<Daughter μ energy> (GeV)	26.02 ±0.07	26.35 ±0.08	23.58 ±0.21
<Inelasticity>	0.794 ±0.001	0.800 ±0.001	0.793 ±0.003
<Missing energy> (GeV)	15.65 ±0.14	14.59 ±0.18	4.45 ±0.53
$<p(daughter)_\perp$ to $\gamma_V>$ (GeV/c)	0.749 ±0.003	0.676 ±0.003	0.618 ±0.008

TABLE 3

Effects of charmed quark fragmentation on daughter energy and acceptance. To increase sensitivity to the choice of fragmentation function $D(z)$, mean daughter energies are shown for events with $\nu>150$ GeV.

$D(z)$	$<E(\text{daughter } \mu)>$	Relative acceptance
$(1-z)^{0.4}$	28.31 ± 0.15	1.00
$(1-z)^3$	26.94	0.81
$(1-z)^{-1.5}$ ($z < 0.99$)	29.78	1.20
Subtracted data	28.20 ± 0.20	

TABLE 4

The Q^2 dependence of the virtual photoproduction cross section for charm. Results are presented for two values of average ν. Errors are statistical.

Q^2 (GeV^2/c^2)	$\sigma_{eff}(\gamma_V N \to c\bar{c}X)$ (nb)	
	$<\nu>=100$ GeV	$<\nu>=178$ GeV
0.075	467.3 ± 24.7	627.1 ± 53.1
0.133	518.6 ± 29.7	628.7 ± 55.1
0.237	498.3 ± 31.8	687.7 ± 47.6
0.422	556.7 ± 45.4	720.7 ± 41.5
0.750	517.5 ± 31.0	698.5 ± 28.8
1.33	444.3 ± 26.4	588.8 ± 41.0
2.37	371.4 ± 23.4	488.0 ± 19.6
4.22	219.4 ± 18.5	378.7 ± 20.8
7.50	149.0 ± 14.1	274.8 ± 16.8
13.3	86.12 ± 8.63	149.8 ± 12.5
23.7	30.76 ± 5.43	68.50 ± 9.63
42.2	7.94 ± 2.96	19.97 ± 6.04

TABLE 5

The ν dependence of the virtual photoproduction cross section for charm in the range $.32 < Q^2 < 1.8$ $(GeV/c)^2$. The first error shown is statistical, the second systematic.

ν (GeV)	$\sigma_{eff}(\gamma_V N \to c\bar{c}X)$ (nb)
60.4	$378.8 \pm 162.6 \, {}^{+\,289.}_{-\,291.}$
69.8	$393.9 \pm 102.0 \, {}^{+\,189.}_{-\,187.}$
80.6	$408.7 \pm 53.31 \, {}^{+\,112.}_{-\,106.}$
93.1	$424.4 \pm 40.56 \, {}^{+\,65.}_{-\,76.}$
107.	$631.8 \pm 41.53 \, {}^{+\,36.}_{-\,30.}$
124.	$559.0 \pm 27.31 \, {}^{+\,61.}_{-\,14.}$
143.	$606.7 \pm 29.51 \, {}^{+\,97.}_{-\,34.}$
165.	$641.1 \pm 30.67 \, {}^{+\,130.}_{-\,49.}$
191.	$693.1 \pm 44.68 \, {}^{+\,162.}_{-\,60.}$

TABLE 6

The Q^2 dependence of the charm structure function $F_2(c\bar{c})$ for two values of average ν. The first error shown is statistical, the second systematic.

Q^2 (GeV/c)^2	$F_2(c\bar{c})$ $<\nu>=100$ GeV	$<\nu>=178$ GeV
0.075	$(3.002 \pm 0.159 \, {}^{+0.451}_{-0.631}) \times 10^{-4}$	$(3.516 \pm 0.297 \, {}^{+0.291}_{-0.222}) \times 10^{-4}$
0.133	$(6.117 \pm 0.351 \, {}^{+0.513}_{-0.513}) \times 10^{-4}$	$(7.221 \pm 0.633 \, {}^{+0.778}_{-0.888}) \times 10^{-4}$
0.237	$(10.69 \pm 0.683 \, {}^{+0.641}_{-1.20}) \times 10^{-4}$	$(15.48 \pm 1.07 \, {}^{+2.28}_{-1.15}) \times 10^{-4}$
0.422	$(21.60 \pm 1.76 \, {}^{+2.48}_{-3.07}) \times 10^{-4}$	$(30.99 \pm 1.78 \, {}^{+1.21}_{-2.11}) \times 10^{-4}$
0.750	$(36.08 \pm 2.16 \, {}^{+2.86}_{-4.95}) \times 10^{-4}$	$(55.89 \pm 2.30 \, {}^{+2.65}_{-4.55}) \times 10^{-4}$
1.33	$(55.27 \pm 3.28 \, {}^{+3.24}_{-3.50}) \times 10^{-4}$	$(84.93 \pm 5.91 \, {}^{+4.38}_{-7.00}) \times 10^{-4}$
2.37	$(81.86 \pm 5.16 \, {}^{+10.4}_{-3.83}) \times 10^{-4}$	$(123.1 \pm 4.93 \, {}^{+7.48}_{-3.40}) \times 10^{-4}$
4.22	$(85.32 \pm 7.21 \, {}^{+8.26}_{-19.2}) \times 10^{-4}$	$(163.9 \pm 9.01 \, {}^{+7.53}_{-17.3}) \times 10^{-4}$
7.50	$(102.0 \pm 9.62 \, {}^{+6.08}_{-10.5}) \times 10^{-4}$	$(203.0 \pm 12.4 \, {}^{+12.2}_{-8.01}) \times 10^{-4}$
13.3	$(104.0 \pm 10.4 \, {}^{+14.0}_{-7.10}) \times 10^{-4}$	$(190.1 \pm 15.9 \, {}^{+17.0}_{-22.2}) \times 10^{-4}$
23.7	$(65.60 \pm 11.6 \, {}^{+2.76}_{-28.4}) \times 10^{-4}$	$(150.6 \pm 21.2 \, {}^{+5.17}_{-5.20}) \times 10^{-4}$
42.2	$(29.94 \pm 11.2 \, {}^{+1.17}_{-1.71}) \times 10^{-4}$	$(76.78 \pm 23.2 \, {}^{+23.7}_{-11.9}) \times 10^{-4}$

TABLE 7

Calculated $10^4 d\,F_2 / d\ln Q^2$ at fixed Bjorken x vs. ν (top), Q^2 (left margin), and x (diagonals, right margin). For each Q^2-ν combination, two values are shown. The bottom value is fit to the structure function F_2 for muon-nucleon scattering (Ref. 12). The top value is the contribution $F_2(c\bar{c})$ to F_2 from diffractive muoproduction of bound and unbound charmed quarks.

ν(GeV)	27	42	67	106	168	x_B
Q^2 (GeV/c)^2	$10^4 \partial F_2(c\bar{c})/\partial\ln Q^2$ over $10^4 \partial F_2(\mu N)/\partial\ln Q^2$					
0.63	17	30	43	54	58	
	1070	1090	1110	1120	1130	
1.0	23	43	63	77	84	
	980	1010	1040	1050	1060	0.002
1.6	30	59	87	107	116	
	650	680	700	720	730	0.003
2.5	36	73	110	139	146	
	310	340	350	360	360	0.005
4.0	36	80	128	162	163	
	320	390	430	460	480	0.008
6.3	29	75	128	165	154	
	210	330	410	460	490	0.013
10	15	54	104	138	112	
	50	220	340	430	480	0.020
16	4	27	64	90	52	
	-130	50	230	360	440	0.032
25	-2	7	26	40	0	
	-189	-126	50	230	370	0.050
40	0	-1	6	10	-22	
	-31	-171	-122	50	240	0.080
63		0	1	1	-16	
	-23	-154	-119	50		0.130

1. Models for charmed particle production. (a) charmed sea production; (b) vector-meson dominance production; (c) virtual photon-gluon-fusion production.

2. The N1 beam line at Fermilab. North is towards the bottom of the page and west is towards the right. Magnets D1 and Q2 are in enclosure 100, Q3 and D2 in enclosure 101, and D3 in enclosure 102. Q4 is in enclosure 103 and D4 is in enclosure 104.

3. Multiwire proportional chambers and scintillation counters in the muon beam.

4. The Multimuon Spectrometer. The magnet, serving also as target and hadron absorber, reaches 19.7 kGauss within a 1.8x1x16 m^3 fiducial volume. Over the central 1.4x1x16 m^3, the magnetic field is uniform to 3% and mapped to 0.2%. Eighteen pairs of multiwire proportional (PC) and drift chambers (DC), fully sensitive over 1.8x1 m^2, determine muon momenta typically to 8%. The PC's register coordinates at 30^0 and 90^0 to the bend direction by means of 0.2 inch cathode strips. Banks of trigger scintillators (S_1-S_{12}) occupy 8 of 18 magnet modules. Interleaved with the 4-inch thick magnet plates in modules 1-15 are 75 calorimeter scintillators (C) resolving hadron energy E with rms uncertainty $1.5E^{\frac{1}{2}}$ (GeV). Not shown upstream of module 1 are one PC and DC, 63 beam scintillators, 8 beam PC's, and 94 scintillators sensitive to accidental beam and halo muons.

5. One module in the muon spectrometer.

6. Calorimeter subtrigger patterns for dimuon events. (a) cluster

grouping of counters; (b) examples of subtriggers. Pulse heights in at least five of ten scintillators in a cluster must exceed a threshold for that cluster to satisfy a calorimeter subtrigger.

7. Calorimeter subtrigger probability vs. shower energy.

8. Trigger hodoscope subtrigger patterns for dimuon events: (a) typical subtrigger; (b) other possible combinations of hits in the third hodoscope.

9. Multiwire proportional chamber center-finding electronics.

10. A drift chamber cell and preamplifier. The cathode wire spacing is 1/12 inch and the separation between cathode planes is 1/4 inch. The full width of the drift cell is 3/4 inch. In the circuit, each stage is one-third of a 10116 ECL triple line receiver. Not shown in the circuit diagram are "pull-down" resistors connecting both outputs from each stage to -5V.

11. Logical flow in the track-fitting program.

12. Distributions in four kinematic variables for the photon-gluon-fusion model. (a) $c\bar{c}$ pair mass. (b) Momentum transfer-squared: (i) all events generated; (ii) events satisfying the dimuon trigger. (c) Energy lost by the beam muon: (i) all events generated; (ii) events satisfying the dimuon trigger. (d) Daughter muon energy: (i) all events generated; (ii) events satisfying the dimuon trigger.

13. Distributions for π, K-decay Monte Carlo: (a) charged multiplicity in simulated showers for π, K mesons with more than 5 GeV of energy; (b) probability vs. shower energy for a shower to yield a decay muon with more than 9 GeV of energy.

14. Distributions in six reconstructed kinematic variables for

background- subtracted data, charm Monte Carlo, and π, K-decay Monte Carlo. The ordinates represent events per bin with acceptance not unfolded. The inverted histograms show the simulated π, K-decay background, normalized to the beam flux. The upright histograms represent background- subtracted data. Errors are statistical. The curves, normalized to the data after analysis cuts, are the photon-gluon-fusion charm calculation. Horizontal bars indicate typical resolution. Events satisfy standard cuts described in the text with specific exceptions noted below. (a) Daughter muon energy. All events have $\nu \gtrsim 150$ GeV; no daughter energy cut is imposed. The unusual ν cut increases the sensitivity of the predictions of the Monte Carlo simulation to assumptions about charmed quark fragmentation. (b) Daughter muon momentum perpendicular to the virtual photon. Events satisfy the standard cuts. (c) Energy transfer ν . The dashed curve represents an alternative model in which $D\bar{D}$ pairs are produced with a hard fragmentation function and a probability independent of ν. Events satisfy standard cuts except that no ν cut is imposed. (d) Momentum transfer-squared. Events satisfy standard cuts. (e) Missing (neutrino) energy. Events satisfy standard cuts. The arrow indicates the shift in the centroid of the data caused by a $\pm 2.5\%$ change in the calorimeter calibration. (f) Inelasticity. Events satisfy standard cuts.

15. Virtual photon variables for 209 GeV muons. (a) Q^2 times the flux of transversely polarized virtual photons. The flux is in units of c^2 GeV^{-3} and represents the number of photons per unit interval of Q^2 and ν. (b) Virtual photon polarization ε. (c) $R = \sigma_L/\sigma_T$ in the photon-gluon- fusion model. σ_L (σ_T) is the probability for a longitudinally (transversely) polarized virtual photon to produce charm

through the reaction $\gamma_V N \to c\bar{c}X$. (d) εR in the photon-gluon-fusion model.

16. Diffractive charm photoproduction cross sections. Parts (a) and (b) show the extrapolation of the effective cross section to $Q^2=0$ at $\nu=$ (a) 178 and (b) 100 GeV. Errors are statistical. The solid curves are fits to $\sigma(0)(1+Q^2/\Lambda^2)^{-2}$, with $\Lambda=$ (a) 3.3 and (b) 2.9 GeV/c; the arrows labeled "NOM" exhibit $\sigma(0)$. Systematic errors are parametrized by (1) decreasing, (2) increasing by 50% the subtracted π, K-decay background, and by recalculating acceptance with a (3) softer, (4) harder fragmentation as described in the text. The effects on $\sigma(0)$ are indicated by the numbered arrows and the effects on Λ are indicated by the dashed curves, normalized to the same $\sigma(0)$. Horizontal bars show typical rms resolution.

17. The role of charm in the rise of the γN total cross section. Data points representing the effective photon cross section (right scale) are compared with a fit from Ref. 51 to half the photon-deuteron cross section (curve, left scale). Systematic uncertainties dominate the errors.

18. Energy-dependence of the effective cross section for diffractive charm photoproduction. For $0.32<Q^2<1.8(\text{GeV/c})^2$, σ_{eff} varies with Q^2 by $\leq 20\%$. Errors are statistical. The solid curve exhibits the ν-dependence of the photon-gluon-fusion model with the "counting-rule" gluon x_g distribution $3(1-x_g)^5/x_g$, and represents the data with 13% confidence. Other gluon-distribution choices $(1-x_g)^9/x_g$, and "broad glue" $(1-x_g)^5(13.5+1.07/x_g)$ (Ref. 9) are indicated by dashed curves. The dashed curve labeled "BN" is the phenomenological parametrization of Ref. 53, and the dashed horizontal line represents energy-independence. Curves are normalized to the data. The shaded band exhibits the range

of changes in shape allowed by sytematic uncertainties. For visual clarity it is drawn relative to the solid curve. Data below $\nu=75$ GeV are excluded from further analysis.

19. Q^2 dependence of the structure function $F_2(c\bar{c})$ for diffractive charm muoproduction. At each of the two average photon energies, each curve is normalized to the data. Errors are statistical. The solid (short dashed) curves labeled $m_c=1.5$ (1.2) exhibit the photon-gluon-fusion model prediction with a charmed quark mass of 1.5 (1.2) GeV/c^2. Solid curves labeled ψDM correspond to a ψ-dominance propagator, and long-dashed curves labeled BN represent the model of Ref. 53. Shown at the top is a fit adapted from Ref. 12 to the inclusive structure function F_2 for isospin-0 muon-nucleon scattering. The shape variations allowed by systematic errors are represented by the shaded bands.

20. Scale-noninvariance of $F_2(c\bar{c})$. Data points are arranged in pairs, alternately closed and open. The points in each pair are connected by a solid band and labeled by their common average value of Bjorken $x = Q^2/(2M\nu)$. Errors are statistical. The dashed lines are predictions of the photon-gluon-fusion model with $m_c=1.5$ GeV/c^2 except that the model is renormalized and damped at high Q^2 as described in the text. The solid bands represent the slope variations allowed by systematic errors. The dot-dashed lines represent the changes in $F_2(c\bar{c})$ as Q^2 is increased but x is held constant that would be necessary to equal the changes in the CHIO fit to F_2 which occur under the same circumstances. The percentages next to these lines indicate the relative sizes of the changes in $F_2(c\bar{c})$ and F_2, fit by CHIO.

21. Distributions describing meson decay for π, K-decay Monte

Carlo: (a) number of meson generations between virtual photon-nucleon interaction and decay muon; (b) decay probability for π's and K's.

22. Distributions for simulated inelastic muon-nucleon collisions: (a) energy lost by the beam muon; (b) momentum transfer-squared.

23. Kinematic distributions for mesons in simulated showers. (a) Feynman x: (i) primary shower mesons with more than 5 Gev of energy; (ii) all secondary mesons before imposing energy conservation. (b) p_T^2: (i) primary shower mesons with more than 5 GeV of energy; (ii) all secondary mesons before imposing energy conservation.

24. Parent meson and daughter muon distributions for simulated showers: (a) energy of hadrons which decay; (b) muon momentum along z axis.

25. Distributions for π, K-decay Monte Carlo events which satisfy the simulated dimuon trigger: (a) energy of produced muons and neutrinos; (b) momentum perpendicular to the virtual photon for produced muons at the decay point.